ÉCOLE POLYTECHNIQUE FÉDÉRALE DE LAUSANNE

MASTER THESIS

Study of $B^0 \to K^{*0}\gamma$ with conversions and $B^0 \to K^{*0}e^+e^-$ at very low q^2

Author:
Clotilde LEMETTAIS

Supervisor:
Dr. Renato QUAGLIANI
Director:
Prof. Olivier SCHNEIDER

Laboratoire de Physique des Hautes Energies
Institut de physique
Faculté des sciences de base

June 24, 2022

Abstract

Master in Physics

Study of $B^0 \to K^{*0}\gamma$ with conversions and $B^0 \to K^{*0}e^+e^-$ at very low q^2

by Clotilde LEMETTAIS

Lepton Flavour Universality is a property of the Standard Model. In recent years, several anomalies have been observed by LHCb in rare flavour changing neutral current decays of B hadrons characterized by $b \to s\ell\ell$ transition, where ℓ stands for electrons or muons final states. In order to validate analysis and correction to simulation methods used to measure the $\mathcal{R}_X$ ratios, *i.e.* the ratio of branching fraction of $b \to s\mu\mu$ with respect to $b \to see$ processes, the branching fraction $\mathcal{B}(B^0 \to K^{*0}e^+e^-)$ is measured at very low invariant dielectron mass ($q^2 = m^2_{ee}$) range. Fits to data collected by the LHCb experiment between 2011 and 2018 are performed in two regions of q^2: the gamma and very low q^2 bins, corresponding to $q^2 \in [0, 0.00098]$ and $q^2 \in [0.00098, 0.10160]$ GeV^2/c^4, respectively. The same fits to data are also used to check and verify the stability of the observed yields over efficiency ratio under different particle identification and multivariate selection criteria.

The branching fraction in the very low q^2 $\mathcal{B}(B^0 \to K^{*0}e^+e^-, vl)$ is measured to be between (1.53±0.12)$\cdot 10^{-7}$ and (1.57±0.12)$\cdot 10^{-7}$ in four different setups while the value obtained from theoretical prediction is either (1.58±0.10)$\cdot 10^{-7}$ or (1.50±0.08)$\cdot 10^{-7}$ depending on the assumptions made. The measured result is compatible with the prediction, which demonstrates the validity of the analysis and correction to simulation in the full q^2 spectrum of $b \to see$.

Contents

1 Introduction

The Standard Model (SM) is the most accurate theory describing fundamental particles and their interaction. Despite this fact, it fails in predicting the observed asymmetry of matter/anti-matter in the universe as well as provide candidates for the dark matter and integrate gravity as fundamental force. Therefore, it is known that this theory is not the ultimate theory and this motivates the search of New Physics (NP) exploring the high-energy scale of processes. Rare processes of b hadrons, characterised by flavour changing neutral current transition ($b \to s\ell\ell$), are suppressed in the Standard Model and can only happen at loop-level. Such characteristics of the process allow to probe much higher energy scales observing indirect effects of possible NP able to modify the rate of the process and properties of the decay such as the angular distributions of final states. A theoretically clean test of the SM is the lepton flavour universality of electro-weak interactions, property for which the coupling of $W/Z/\gamma$ bosons to the three lepton families is predicted to be universal. Therefore, any deviation from unity in the ratio of branching fractions $\mathcal{B}(b \to s\mu\mu)$ to $\mathcal{B}(b \to see)$ has to be interpreted as a clear sign of New Physics. In this context, hints and a coherent pattern of anomalies of lepton flavour universality violation have been observed in rare b meson decays by the LHCb experiment [1, 2, 3, 4] and the various results from LHCb are briefly sketched in figure 1.1.

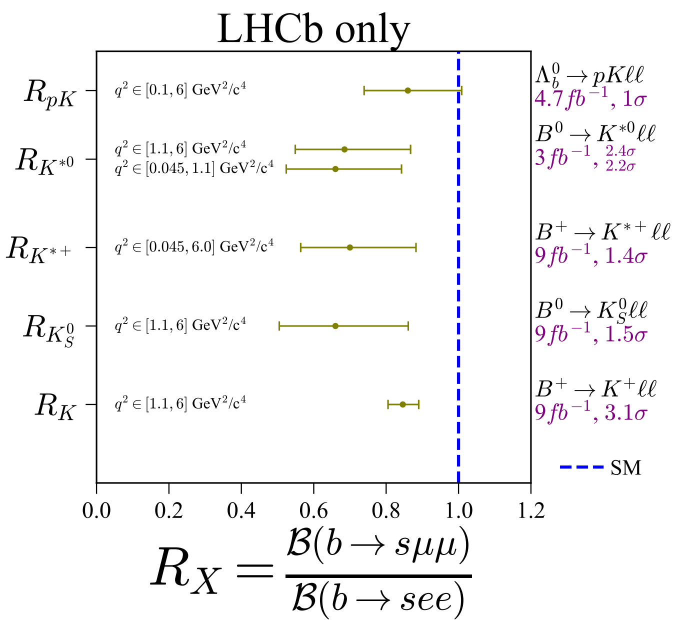

FIGURE 1.1: Deviation from SM in LHCb measurements of $b \to s\ell\ell$ transitions [1, 2, 3, 4]

1.1 Study of the $B^0 \to K^{*0}e^+e^-$ and $B^0 \to K^{*0}\gamma(\to e^+e^-)$ decays

The two decays studied in this thesis are $B^0 \to K^{*0}e^+e^-$ selected in a specific region of the dielectron mass squared m^2_{ee} (= q^2) and $B^0 \to K^{*0}\gamma$ which are respectively called very low and gamma q^2 bins throughout the document. The latter one takes benefit of the interaction in material and conversion of the photon into a pair of electrons to reconstruct the decay. The dominant Feynman diagrams of the $B^0 \to K^{*0}e^+e^-$ decay are presented in figure 1.2. In the case of $B^0 \to K^{*0}\gamma(\to e^+e^-)$, the photon is real and the conversion $\gamma \to e^+e^-$ happens in the detector material. The two decays have a low branching fraction, as their world average which can be found in the PDG [5] are $\mathcal{B}(B^0 \to K^{*0}e^+e^-) = (1.03^{+0.19}_{-0.17}) \cdot 10^{-6}$ and $\mathcal{B}(B^0 \to K^{*0}\gamma) = (4.18 \pm 0.25) \cdot 10^{-5}$, where the branching fraction of $B^0 \to K^{*0}e^+e^-$ is measured over the whole q^2 range removing the resonances.

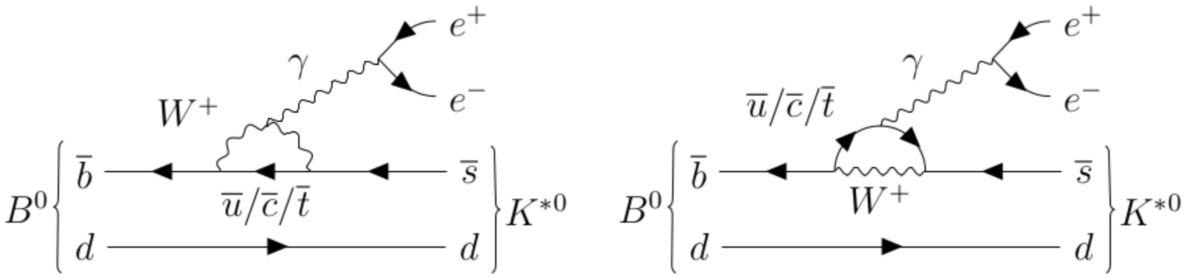

FIGURE 1.2: Dominant Feynman diagrams of the $B^0 \to K^{*0}e^+e^-$ decay [6]

In these two decays, the K^{*0} decays into $(K^+\pi^-)$ and the geometry of the total decay can be parameterised with the angles θ_l, θ_K and ϕ as can be seen on figure 1.3

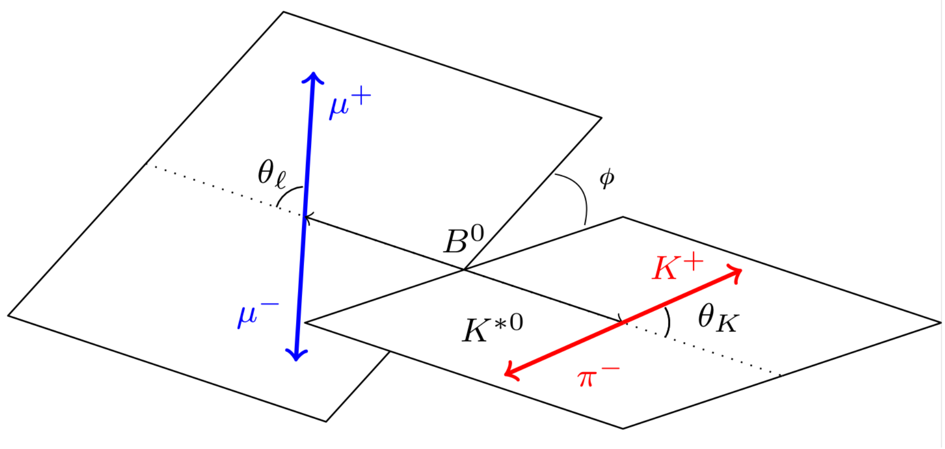

FIGURE 1.3: Geometry and parametrisation of the $B^0 \to K^{*0}e^+e^-$ decay [6]

As the branching fraction of the $B^0 \to K^{*0}e^+e^-$ decay varies with q^2, different bins of analysis are usually defined as can be seen on figure 1.4, which are sensitive to NP in different manner. Sensitivity to NP in such decays is therefore achieved studying the process as a function of q^2.

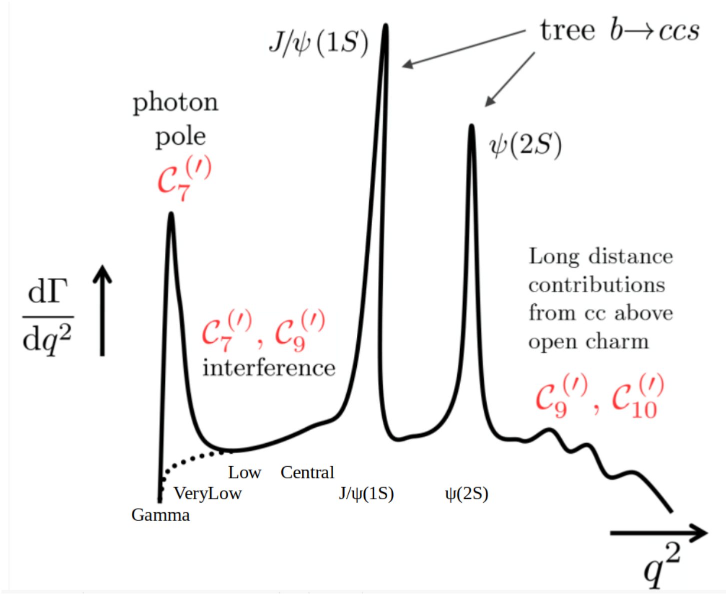

FIGURE 1.4: Variation of the $B^0 \to K^{*0}e^+e^-$ decay rate as a function of q^2 and contribution of the dominant Wilson coefficients in the different bins [7]

Tests of lepton flavour universality at LHCb in the K^+ and K^{*0} final states decays are obtained using as normalisation and calibration channels the corresponding $B^{+,0} \to K^{+,*0}J/\psi\,(1S)(\to \ell\ell)$ [2] decay. The ratio of branching fractions in different q^2 regions (low and central for $\mathcal{R}_{K^*}$, *i.e.* $q^2 \in [0.045, 1.1]$ GeV^2/c^4 and $q^2 \in [1.1, 6.0]$ GeV^2/c^4 [2]; central only for $\mathcal{R}_K$, *i.e.* $q^2 \in [1.1, 6.0]$ GeV^2/c^4 [1]) are expressed as a double ratio (1.1) in order to cancel out most of the efficiency systematics arising from the different reconstruction efficiencies of electrons and muons in LHCb.

$$\mathcal{R}_{K^{(*)}} = \frac{\Gamma(B \to K^{(*)}\mu^+\mu^-)}{\Gamma(B \to K^{(*)}e^+e^-)} \times \frac{\Gamma(B \to K^{(*)}J/\psi(e^+e^-)}{\Gamma(B \to K^{(*)}J/\psi(\mu^+\mu^-)} \tag{1.1}$$

The double ratio approach used by LHCb analyses is validated at the $\psi(2S)$ region as well, which similarly to the J/ψ channel is characterised by tree-level $b \to c\bar{c}s$. Since $J/\psi \to \ell\ell$ and $\psi(2S) \to \ell\ell$ are due to $c\bar{c} \to \ell\ell$, any New Physics effect is totally negligible leading the theory expectation of ratios of decay rates in those modes between μ and e to be unity. Such property is therefore used to validate the LFU analyses.

However, such analysis validation cross-check is performed at much higher q^2 than the one of interest of rare decays, and the assumption that efficiencies and corrections to them are portable from J/ψ to lower q^2 is assumed.

In this context, the $B^0 \to K^{*0}e^+e^-$ decay can be studied in the very low q^2 (*vl*) region, which is a region in q^2 where the branching ratio of $b \to see$ is enhanced by the proximity of the dielectron mass m_{ee} to the photon pole. Such enhancement allows to have a clean and statistically significant sample to analyse and perform various checks validating the efficiency calculations and corrections to simulation when electrons are present in the final states. This check is complementary to what is done in the J/ψ and $\psi(2S)$ region. The $B^0 \to K^{*0}e^+e^-$ decay is chosen for this analysis as the spin 1 nature of K^{*0} allows the existence of the photon pole. Indeed, according to the angular momentum conservation, the spin 0 K^+ in the $B^+ \to K^+e^+e^-$ decay prevents the photon pole (and its shape is shown by the dotted line on figure 1.4).

The measurement of the $\mathcal{B}(B^0 \to K^{*0}e^+e^-, vl)$ branching fraction at very low q^2 divided by the $\mathcal{B}(B^0 \to K^{*0}\gamma)$ branching fraction is theoretically predicted with a precision at the percent level even in presence of NP. Indeed, since all the bins are not subject to the same Wilson coefficients (which are expressing the strength of the operators describing the point-like vertices in effective field theory, see section 2), one can take advantage of it for the analyses. The gamma and the very low bins are dominated by $\mathcal{C}_7^{(\prime)}$ contributions and the decay width in that region is almost unaffected by $\mathcal{C}_9^{(\prime)}$ and $\mathcal{C}_{10}^{(\prime)}$. Thus, the ratio of the branching fractions of $B^0 \to K^{*0}e^+e^-$ and $B^0 \to K^{*0}\gamma$ is expected to be precisely predicted even in presence of NP as almost a full cancellation of potential NP effects affecting only $\mathcal{C}_7^{(\prime)}$ is expected. Moreover, residual interference effects from $\mathcal{C}_9^{(\prime)}$ and $\mathcal{C}_{10}^{(\prime)}$ which would change the predictions in very low q^2 are also expected to be very small.

The goal of this work is to compare the experimental value obtained with LHCb data with such prediction providing an extremely solid check of the calibration of efficiencies of electron modes in a region of q^2 which is smaller than the most sensitive to NP one.

1.2 Choice of the q^2 range

In order to take advantage of the proximity to the photon pole, the very low q^2 range has to be selected as low as possible. It is thus chosen to be $q^2 \in [0.0001, 0.1]$ GeV^2/c^4 corresponding to $m_{ee} \in [10, 320]$ MeV/c^2. The gamma bin is defined as $q^2 \in [0, 0.0001]$ GeV^2/c^4.

Lower boundary: The very low q^2 range could be chosen to start at the threshold value of $m_{ee} = 2m_e \approx 1$ MeV/c^2. However, the angle between the two electrons gets smaller as their invariant mass is getting lower, which leads to a worse definition of the plane containing the dielectron pair, and thus, a worse definition of the angle ϕ between the plane containing the two leptons and the plane containing the two hadrons. According to the analysis [6], the error on the measurement of the angle ϕ reaches more than 1 rad below $m_{ee} = 10$ MeV/c^2 while it is below 500 mrad above this m_{ee} limit. Following the choice made in [6], the lower m_{ee} limit is set to 10 MeV/c^2, corresponding to a q^2 limit of 0.0001 GeV^2/c^4.

Upper boundary: The upper boundary is chosen such that the disentanglement between the contributions of $\mathcal{C}_7^{(\prime)}$ and $\mathcal{C}_{9,10}$ is kept and to consider a statistically independent q^2 range to the one measured within the $\mathcal{R}_X$ measurement. Indeed, for the angular analysis [6], the upper limit was chosen to be $m_{ee}^{max} = 500$MeV/c^2, but since $\mathcal{R}_{K*}$ will be measured in a region starting at q^2 = 0.1 GeV^2/c^4, the upper limit for the very low q^2 is chosen to be 0.1 GeV^2/c^4. Furthermore, since the present study aims at measuring the ratio of the branching fractions of $B^0 \to K^{*0}e^+e^-$ and $B^0 \to K^{*0}\gamma$, the predictions of this ratio are studied in the case of different contributions from $\mathcal{C}_9$ and

$\mathcal{C}_{10}$. The extreme cases where the deviation from the Standard Model in the $b \to see$ transition is $\Delta\mathcal{C}_{9,10} = \pm 1$ are shown on figure 1.5. The predictions were computed using the `Flavio` package on the q^2 range [0.0001, q^2_{max}].

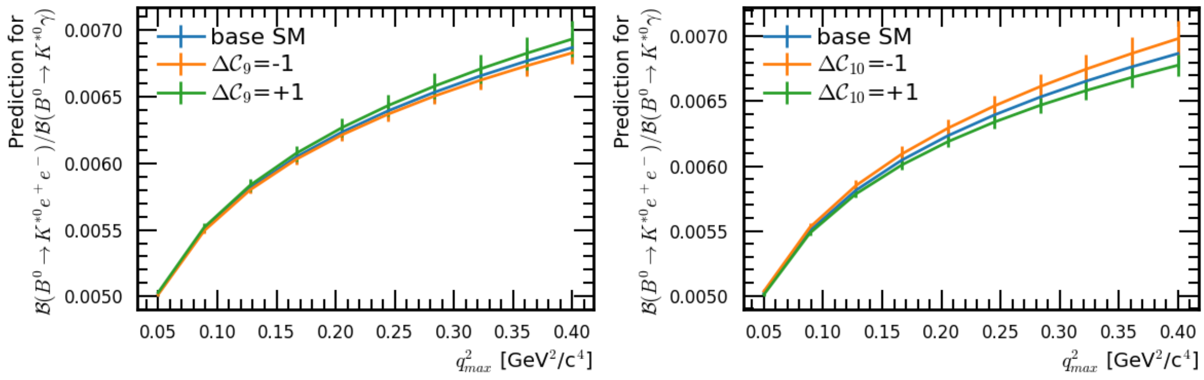

FIGURE 1.5: Predictions for the $\frac{\mathcal{B}(B^0 \to K^{*0}e^+e^-)}{\mathcal{B}(B^0 \to K^{*0}\gamma)}$ ratio for different upper limit of the q^2 range

As one can see, if the upper limit is set to $q^2 = 0.1$ GeV/c^2, even a quite important departure from the SM in $\mathcal{C}_9$ or $\mathcal{C}_{10}$ should not affect the studied ratio.

Effective q^2 range: When requiring events to be in a given reconstructed q^2 region of interest, the effectively selected q^2 which is relevant in theory prediction can suffer from resolution and migration effects. The reconstructed q^2 resolution can be significantly improved by using the reconstructed dielectron mass with the constraint that the four body states $m(K^+\pi^-e^+e^-)$ mass is equal to the B^0 mass and using the *DecayTreeFitter* tool [8] with such constraint to fit the B^0 kinematics [6]. However, q^2 migration effects still need to be taken into account even after that. To do so, the effective q^2 range is measured in simulation, by studying the effect of the selection in the reconstructed q^2 while looking at the true q^2. The effective q^2 boundaries are therefore determined convoluting the efficiency of the true q^2 with the `Flavio` prediction for $d\mathcal{B}(B^0 \to K^{*0}e^+e^-)/dq^2$, *i.e.* such that in the rising and decreasing regions of the efficiency curve, the same number of events is obtained in a uniform acceptance model and in the MC. This measurement gives a resulting effective q^2 of $[0.00098, 0.10160]$ GeV^2/c^4, corresponding to $m_{ee} \in [31.30, 318.75]$ MeV/c^2 and can be seen on figure 1.6.

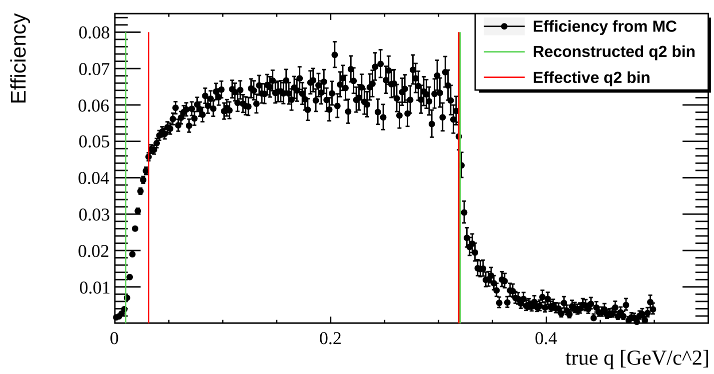

FIGURE 1.6: Effective q^2 range for the very low bin

1.3 RX framework

Efficiencies for LFU measurements are usually evaluated on simulated events after having applied data-driven corrections to them. The motivation behind doing such procedure is that few key properties such as the B hadron kinematics, particle identification performances, track reconstruction and trigger reconstruction are not correctly simulated. Therefore, efficiencies from those selections and reconstruction steps have to be corrected for to assess an accurate efficiency estimation. This thesis has been performed within the so called `RX-framework`, developed for the measurements of $\mathcal{R}_X$ ratios involving $b \to s\ell\ell$ transitions in LHCb. This framework has been designed to provide the first simultaneous analysis of $B^+ \to K^+\ell\ell$ and $B^0 \to K^{*0}\ell\ell$ decay at LHCb. For this coming measurement, both the low and central q^2 regions will be analysed, where the low region is reevaluated to start at 0.1 $\mathrm{GeV}^2/\mathrm{c}^4$ instead of 0.045 $\mathrm{GeV}^2/\mathrm{c}^4$ as in the previous measurements.

The framework has been expanded to perform the present work incorporating part of the developments being done for the angular analysis of $B^0 \to K^{*0}\ell\ell$ at very low q^2 [9]. Indeed, for the case of the K^{*0} analysis, the framework was already implemented for the studies in the low, central, J/ψ and $\psi(2S)$ q^2 regions. The work done in this thesis allowed the inclusion of the gamma and very low q^2 within the framework. Starting from the selection existing for the low q^2 region as a baseline, the framework has been expanded for the very low q^2 and for the gamma q^2 in order to handle mass fits, corrections to simulation and efficiency calculations.

1.4 Analysis strategy

The main goal of this thesis is to measure $\mathcal{B}(B^0 \to K^{*0}e^+e^-)$ in the very low q^2 and compare it with the theory expectations taking benefit of the precisely predicted ratio of branching fraction of the decay of interest with respect to $\mathcal{B}(B^0 \to K^{*0}\gamma)$, which has been experimentally measured in Belle [10]. To do so, the $B^0 \to K^{*0}e^+e^-$ decay is studied in the very low q^2 region using all the available LHCb data collected from 2011 to 2018.

For the measurement of $\mathcal{B}(B^0 \to K^{*0}e^+e^-)$, mass fits are performed on the B^0 mass obtained after having constrained the vertices of the decay in the very low q^2 region in order to extract the number of signal events. A validation of the yields obtained is made by performing a template fit to the θ_K angle (defined in figure 1.3) while fixing the yields according to the ones obtained in the invariant mass fits. The corresponding efficiencies are also computed and corrected, to take into account the mis-modelling of relevant quantities following the correction method used for the $\mathcal{R}_X$ analyses.

In order to cancel a part of the systematic uncertainties, the branching fraction of interest is normalised to the J/ψ resonant mode (see figure 1.4) which has a well known branching fraction and provides a clean and high statistics data sample to fit. The mass fit for $B^0 \to K^{*0}e^+e^-$ and $B^0 \to K^{*0}J/\psi(\to e^+e^-)$ is performed simultaneously. Moreover, in order to have better handles on backgrounds (such as $B_s \to K^{*0}J/\psi$) in the J/ψ resonant mode, the muon mode $B^0 \to K^{*0}J/\psi(\to \mu^+\mu^-)$ is also included in the simultaneous fit.

The $B^0 \to K^{*0}e^+e^-$ branching fraction is therefore measured following the expression (1.2):

$$\mathcal{B}(B^0 \to K^{*0}e^+e^-) = \frac{\mathcal{N}(B^0 \to K^{*0}e^+e^-)}{\mathcal{N}(B^0 \to K^{*0}J/\psi)} \cdot \frac{\epsilon_{B^0 \to K^{*0}J/\psi}}{\epsilon_{B^0 \to K^{*0}e^+e^-}} \cdot \frac{\mathcal{B}(B^0 \to K^{*0}J/\psi)}{1 - F_s} \cdot \mathcal{B}(J/\psi \to e^+e^-) \tag{1.2}$$

where $\mathcal{N}$ are the yields obtained from the mass fits and ϵ are the corresponding corrected efficiencies.

The measured values of $\mathcal{B}(B^0 \to K^{*0}J/\psi) = (1.27 \pm 0.05) \cdot 10^{-3}$ and $\mathcal{B}(J/\psi \to e^+e^-) = (5.971 \pm 0.032) \cdot 10^{-2}$ are used and taken from the PDG [5], while $F_s = 0.084 \pm 0.01$ is the fraction of the S-wave in the resonant channel measured in [11]. The F_s parameter has to be included since the measured yields in $K^{*0}J/\psi$ comprise both the resonant K^{*0} (P-wave) and the non-resonant $(K^+\pi^-)$ (S-wave) modes, while the branching ratio value from the PDG for $\mathcal{B}(B^0 \to K^{*0}J/\psi)$ only accounts for the P-wave.

A second check that can be performed is to determine if at a relative level, the efficiency corrections are controlled in the gamma and very low q^2 bins. To do so, also the gamma bin is fitted and yields are extracted. A study of the variation of yields and efficiencies under different particle identification selections and multivariate classifier requirement criteria is also performed. A good indication of the stability of the $\mathcal{R}_X$ analysis procedure and correction to simulation is provided by studying whether the ratio of the two (yields and efficiencies) is stable under different requirements. This check is made in both the very low and the gamma q^2 bins as one can take advantage of the higher statistics of the gamma bin.

2 Theory

2.1 The Standard Model and beyond

The Standard Model (SM) is the theory describing the particles and their interactions in the universe [12]. In addition to give a description of three of the four fundamental forces, it classifies the particles as can be seen on figure 2.1.

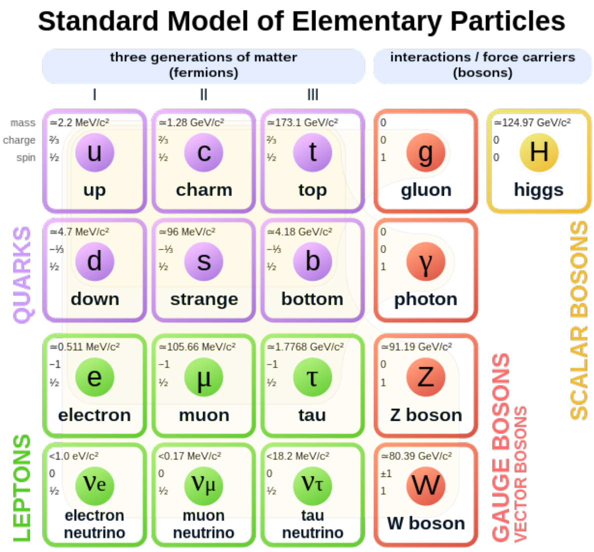

FIGURE 2.1: Standard Model classification of particles and interactions [13]

In the SM, the electroweak interaction has the same coupling for the three generations of leptons. This property, called Lepton Flavour Universality (LFU), has been verified in many experiments. However, some hints of a violation of this property has been highlighted by the LHCb experiment in B meson decays [1, 14]. In particular, the evidence of violation of the LFU has been measured in the $B^+ \to K^+\ell^+\ell^-$ ($\ell = e, \mu$) decay with a significance of 3.1σ [1].

This violation can arise in processes forbidden at tree-level, such as flavour changing neutral currents, thus letting possible New Physics (NP) to appear. This is the case in the $b \to s\ell\ell$ transitions where the SM predicts a loop process involving a W and a Z or γ bosons and a $u/c/t$ quark, but where there could be a contribution of NP involving an hypothetical leptoquark or a new neutral boson which could have a different coupling with the different lepton flavours [1]. These two possibilities are shown on figure 2.2.

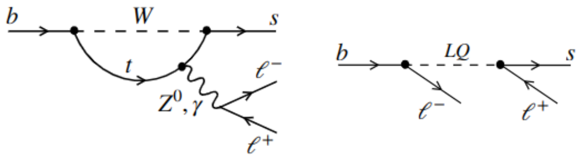

FIGURE 2.2: (Left) SM contribution for $b \to sll$ transition, (Right) Possible new physics contribution through a leptoquark interaction [14]

In order to corroborate LHCb results and provide the most sensitive experimental input from LHCb data in this context, both the K^{*0} and K^+ are analysed simultaneously to update the current K^{*0} measurement (which used only 2011 and 2012 data from LHCb) and validate at the same time the evidence of LFU violation measured in $\mathcal{R}_K$. One of the main method to study Lepton Flavour Universality (LFU) is to measure the so-called $\mathcal{R}_X$ ratios (2.1) which are expected to be unity in the SM:

$$\mathcal{R}_X = \frac{\mathcal{B}(B_{u,d} \to X_s \mu^+ \mu^-)}{\mathcal{B}(B_{u,d} \to X_s e^+ e^-)} \tag{2.1}$$

For the processes $B^+ \to K^+ \ell^+ \ell^-$ and $B^0 \to K^{*0} \ell^+ \ell^-$ involving $b \to s\ell\ell$ transitions, the SM predicts the corresponding $\mathcal{R}_K$ and $\mathcal{R}_{K^*}$ ratios (2.2) (2.3) [7] to be equal to 1 over almost the whole q^2 range. Since all uncertainties due to hadronic terms cancel out, on gets a very clean theory expectation with 1% uncertainty due to QED correction factors. A departure from unity in these ratios is thus a clear sign of NP happening in the $b \to s\ell\ell$ transitions.

$$\mathcal{R}_K = \frac{\int_{q^2_{min}}^{q^2_{max}} \frac{d\Gamma(B^+ \to K^+ \mu^+ \mu^-)}{dq^2} dq^2}{\int_{q^2_{min}}^{q^2_{max}} \frac{d\Gamma(B^+ \to K^+ e^+ e^-)}{dq^2} dq^2} \tag{2.2}$$

$$\mathcal{R}_{K^*} = \frac{\int_{q^2_{min}}^{q^2_{max}} \frac{d\Gamma(B^0 \to K^{*0} \mu^+ \mu^-)}{dq^2} dq^2}{\int_{q^2_{min}}^{q^2_{max}} \frac{d\Gamma(B^0 \to K^{*0} e^+ e^-)}{dq^2} dq^2} \tag{2.3}$$

2.2 Effective field theory and Wilson coefficients

The interactions happening in such loop processes can be described by an effective field theory (EFT) [15] where the interaction loop is reduced to a point-like interaction. In this theory, the Hamiltonian of $b \to s\ell\ell$ or $b \to s\gamma$ transition is provided by the expression (2.4) [16].

$$\mathcal{H}_{eff} = -\frac{4G_F}{\sqrt{2}} V_{tb} V_{ts}^* \sum_i (\mathcal{C}_i \mathcal{O}_i + \mathcal{C}'_i \mathcal{O}'_i) \tag{2.4}$$

where G_F is the Fermi constant, V_{tb} and V_{ts}^* the dominant elements of the CKM matrix entering the loop-level process, $\mathcal{C}_i^{(\prime)}$ are the so-called Wilson coefficients encoding the strength of the associated $\mathcal{O}_i^{(\prime)}$ local operator describing the point-like interactions vertices.

In the very low q^2 the operator describing the process is $\mathcal{O}_7^{(\prime)}$ related to the $b \to s\gamma^{(*)}$ transition while $\mathcal{O}_9^{(\prime)}/\mathcal{O}_{10}^{(\prime)}$ are related to the $b \to s\ell\ell$ transition mediated by a W/Z, together with their corresponding Wilson coefficients for a total of six operators. These operators are given by expression (2.5) [16].

$$
\begin{array}{ll}
\mathcal{O}_7 \propto m_b(\bar{s}\sigma_{\mu\nu}P_R b)F^{\mu\nu} & \mathcal{O}_7' \propto m_b(\bar{s}\sigma_{\mu\nu}P_L b)F^{\mu\nu} \\
\mathcal{O}_9 \propto (\bar{s}\gamma_\mu P_L b)(\bar{\ell}\gamma^\mu \ell) & \mathcal{O}_9' \propto (\bar{s}\gamma_\mu P_R b)(\bar{\ell}\gamma^\mu \ell) \\
\mathcal{O}_{10} \propto (\bar{s}\gamma_\mu P_L b)(\bar{\ell}\gamma^\mu \gamma_5 \ell) & \mathcal{O}_{10}' \propto (\bar{s}\gamma_\mu P_R b)(\bar{\ell}\gamma^\mu \gamma_5 \ell)
\end{array}
\tag{2.5}
$$

where m_b is the mass of the b quark, $\sigma_{\mu\nu} = \frac{i}{2}[\gamma_\mu, \gamma_\nu]$, $F^{\mu\nu}$ is the electromagnetic tensor and $P_{R/L} \propto (1 \pm \gamma_5)$ the right and left chirality projectors.

In the SM, the Wilson coefficients $\mathcal{O}_9'$ and $\mathcal{O}_{10}'$ are equal to zero, and the ratio $\frac{\mathcal{O}_7'}{\mathcal{O}_7} \approx \frac{m_s}{m_b} \approx 0.02$, which leads to a heavy suppression of the $b \to s\gamma$ with a right-handed photon [16].

3 Technical aspects

3.1 LHCb detector

The data used in this thesis have been collected by the LHCb experiment at the LHC between 2011 and 2018 for a total integrated luminosity of 9 fb^{-1}. LHCb is one of the four detectors located on the Large Hadron Collider (LHC) at CERN and aims at detecting and study the decays of b and c hadrons produced in pp collisions at a center of mass energy of $\sqrt{s} = 14$ TeV.[1] The LHCb detector has been primarily designed to perform precise measurements on CP violation and the study of rare b hadron decays and it is designed as a single-arm forward spectrometer covering the pseudo-rapidity range $2 < \eta < 5$. As can be seen on figure 3.1, LHCb is composed of a tracking system, two Cherenkov detectors (RICH1 and RICH2), an electromagnetic calorimeter (ECAL), a hadronic calorimeter (HCAL) and a muon system (M1 - M5). The tracking system consists of a vertex locator (VELO) and tracking stations located on both sides of the 4 Tm LHCb dipole magnet (TT, T1, T2, T3). This thesis presents a summarised description of the detector components, which are described in detail in ref. [17].

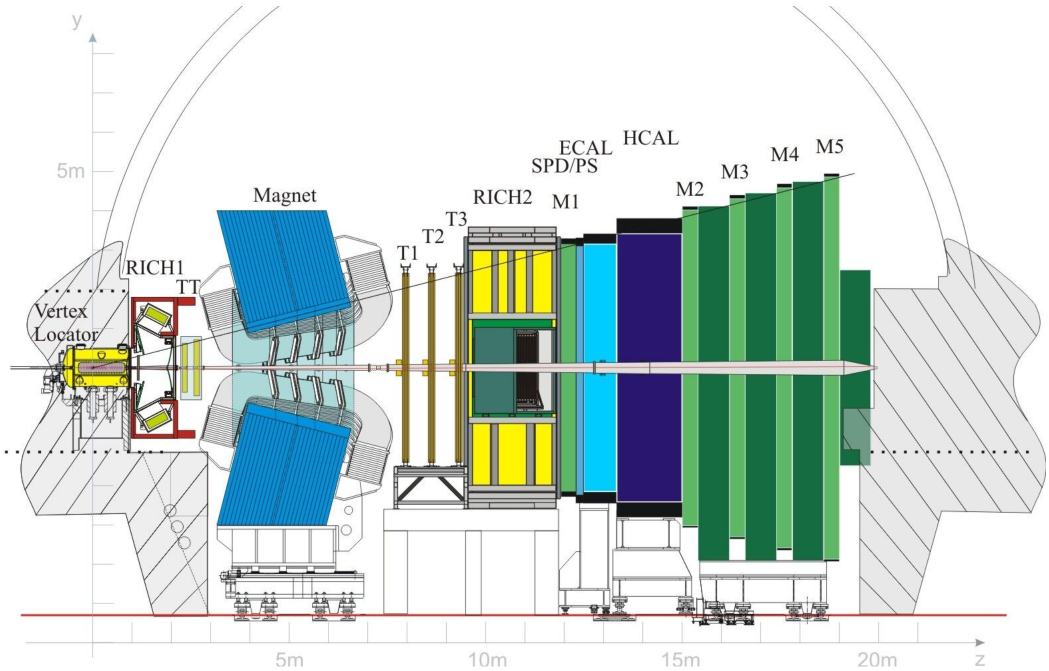

FIGURE 3.1: LHCb detector [17]

[1] In 2011(2012) $\sqrt{s} = 7(8)$ TeV, while for 2015, 2016, 2017 and 2018 $\sqrt{s} = 13$ TeV.

Vertex Locator (VELO): The VELO is surrounding the pp interaction point and its closest detection active material sensor to the beam pipe is placed at a distance of 8 mm from it. The detector aims at selecting and identify the primary and secondary vertices of b hadron decays as well as measure the decay length of b hadrons. It is composed of 42 silicon detectors allowing to detect the position of the vertices corresponding to the b hadron decays with a precision on the position measurement up to 4 μm [18].

Magnet : By bending the trajectory of the charged particles in its magnetic field, the magnet of the LHCb detector allows a precise measurement of the charged particle momentum. The dipole magnet is made of two conical saddle shape coils placed face to face along the beam axis and provides an integrated magnetic field of 4 Tm.

Ring Imaging Cherenkov detectors (RICH1, RICH2): The two RICH detectors are placed upstream and downstream of the dipole magnet and they are responsible for low/ high momentum particle identification in LHCb, respectively. Hybrid Photon Detectors (HPD) detect the light ring emitted by the charged particles travelling faster than light in the gas contained in the detectors, thus allowing to measure their speed. The RICH1 detector, placed before the magnet, contains silica aerogel (which has been removed after 2012 data taking [19]) and C_4F_{10} gas radiator whose properties allow to achieve discrimination power in the low-momentum region ($p \sim 1 - 60$ GeV/c). The RICH2, placed after the magnet, contains a CF_4 gas radiator and it extends particle identification power in the higher-momentum regions ($p \sim 15 - 100$ GeV/c).

Tracking system (TT, T1, T2, T3): As the RICH detectors, the tracking system is placed on either sides of the magnet. It records the trajectory of charged particles, allowing to determine their momenta. It is composed of two trackers with different technologies. The first one is a silicon tracker, composed of the Tracker Turicensis (TT), located upstream of the magnet, and the inner tracker (IT) of the T1 to T3 stations, located downstream of the magnet. The second tracker is the outer tracker (OT) of the T1–T3 stations and uses straw tubes drift chambers.

Calorimeter system (SPD, PS, ECAL, HCAL) : The calorimeter system's goal is to identify electrons, photons and hadrons, and to measure their energy and position by stopping the particles as they travel through the detector material. In particular, it is essential for the reconstruction of neutral particles such as photons and neutral pions. The first layer of this calorimeter system is the Scintillating Pad Detector (SPD), which aims at differentiating charged and neutral particles. It is directly followed by a Pre-Showering detector (PS), aiming at separating electro-magnetic and hadronic showers. Then, the Electromagnetic Calorimeter (ECAL), made of lead plates interspaced with scintillating tiles, measures the energy and position of the lighter particles such as electrons and photons with an energy resolution $\sigma_E/E = (8 \to 10)\%/\sqrt{E} \oplus 0.9\%$ (E in GeV) [20] while the Hadronic Calorimeter (HCAL), made of iron plates interspaced with scintillating tiles provides this information for hadrons with an energy resolution $\sigma_E/E = (69 \pm 5)\%/\sqrt{E} \oplus (98 \pm 2)\%$ (E in GeV) [20]. The different parts of the calorimeter system and the detection logic is shown on figure 3.2.

The four subdetectors are designed to handle the difference of hit density along the distance from the beam pipe. The SPD/PS and ECAL are composed of three sections

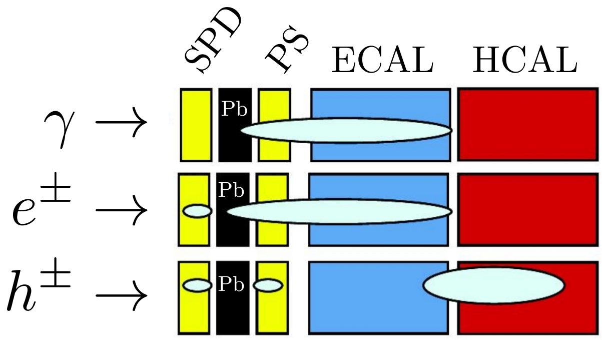

FIGURE 3.2: LHCb calorimeter system and $\gamma/e/$hadrons identification [21]

with different granularities, from high granularity closer to the beam axis to lower granularity in the outer part. The HCAL follows the same design with only two sections.

Muon system (M1, M2, M3, M4, M5) : Muons are the most penetrating particles among charged particles detectable in LHCb as stable particles. For this reason, the muon system is located at the very end of the detector. It is composed of five stations made of Multi Wired Proportional chambers. They are filled with a mixture of CO_2, Ar and CF_4. The gas gets ionised by the muons travelling through the detector. The M1 station is located in front of the SPD/PS and the four other stations are located after the calorimeter system and are separated by iron layers. As the calorimeter system, the granularity of the stations changes along the distance to the beam axis in order to maintain a constant occupancy over the detector.

3.2 Events reconstruction and trigger logic

Reconstruction: In order to reconstruct the $B^0 \to K^{*0}e^+e^-$ events, one looks for a K^{*0} candidate, composed of two tracks identified as K^+ and π^-, and two tracks identified as electron and positron. All the tracks and vertices are required to fulfil and pass several quality requirements as described in section 4.

Concerning the electron tracks, the bremsstrahlung photons emitted by the electrons upstream the dipole magnet when traversing the detector material in the VELO and the RICH1 are recovered and reconstructed in order to recover the missing energy and improve the momentum measurement. The bremsstrahlung process in LHCb is sketched on figure 3.3.

Since photons are neutral, their trajectory is not bent by the magnet. The photons emitted before the magnet are thus recovered and reconstructed in the ECAL (E1). However, photons emitted after the magnet will follow the same trajectory as the electron from which they come from. This will therefore result in a single cluster (E2) in the calorimeter and the energy of these photons will be reconstructed together with the electron [17]. Nonetheless, this recovery routine has only around 50% efficiency.

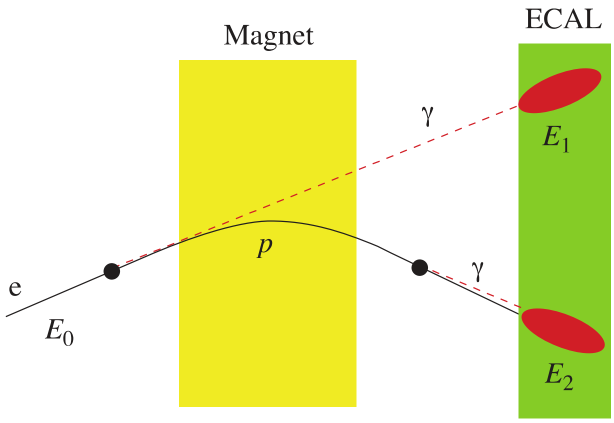

FIGURE 3.3: Bremsstrahlung process and reconstruction at LHCb [17]

The candidates reconstructed as $K^{*0}e^+e^-$ are therefore categorised into three bremsstrahlung categories depending on how many brem photons were recovered:

- 0G: no brem photons have been recovered in the dielectron pair
- 1G: only one brem photon has been recovered
- 2G: more than one brem photon has been recovered

Trigger logic: Events are required to pass two types of trigger: L0, which is a hardware-based trigger relying on detector information available at the read-out level; and HLT, which is a software-based trigger relying on reconstructed tracks and vertices.

The analysis is performed on two different L0 trigger categories : L0I and L0L. L0I is the primary trigger, which is fired when any particle in the event which is not a final state is firing the `L0Muon` or `L0Hadron` or `L0Electron` hardware trigger (*i.e.* having a cluster in the muon system, the HCAL or the ECAL with a positive decision) as outlined in section 4. L0L is the secondary trigger and is fired when the electron final states in the reconstructed $K^{*0}e^+e^-$ have the ECAL clusters associated to a positive decision of the `L0Electron` trigger.

3.3 Samples

The dataset used for this thesis consists in the full available data to date collected by the LHCb experiment during the LHC Run 1 (2011 and 2012) and Run 2 (2015, 2016, 2017, 2018), corresponding to a total integrated luminosity of 9 fb^{-1}. The center of mass energy at which the data has been collected is 7 TeV in 2011, 8 TeV in 2012 and 13 TeV from 2015 to 2018. For this study, the data is divided into three sets corresponding to the LHC Run 1 (R1 : 2011-2012), Run 2 part 1 (R2p1 : 2015-2016) and Run 2 part 2 (R2p2 : 2017-2018). Each run period subset is also divided into the two trigger categories L0I and L0L. Among the samples, the data corresponding to the two magnet polarity data taking conditions (up and down) is merged. Indeed, in order to cancel detector asymmetry effects, data is taken each year with both up and down polarities in approximately 50%-50% fractions.

Monte-Carlo simulated samples are used for the modelling of the components of data and for efficiency estimation. They are divided in samples of run period and trigger following the same logic as for data. For the simulation of signal, a sample `Bd2KstEE` is used for the very low q^2 region, and a sample `Bd2kstGEE` is used for the gamma q^2 region. The decay models used to create the MC simulation samples are the ones predicted by the SM. This means that the q^2 and decay angles distributions in simulation are the ones expected by SM predictions. MC simulations are also used in order to model the specific and partially reconstructed backgrounds discussed in section 5.

4 Selection

The first step of this project is to define a selection for the analysis. The RX framework being already implemented for the low q^2 region, one can take the selection applied in this region as a baseline and adapt it for the very low and gamma q^2 bins. Some selection cuts are also chosen in agreement with what has been done in the angular analysis [6] in order to allow comparisons with their results along the study.

The main selection cuts are presented in this section, and a table with the list of all cuts depending on the sample and q^2 bin is shown in appendix A.

4.1 Trigger

As specified before, the analysis is performed on L0I and L0L samples separately. For the L0I sample, the requirement is to have a positive decision on `L0Hadron` or `L0Electron` or `L0Muon` but triggered by a particle which is not in the candidate final states. The event is triggered if a cluster with minimum transverse energy between 2.4 and 3.0 GeV depending on the data period is observed in the HCAL, the ECAL or the muon system by such particle. For the L0L sample, the `L0Electron` should be fired, *i.e.* a cluster with minimum transverse energy between 2.4 and 3.0 GeV depending on the data period should be observed in the ECAL, by an electron from the signal final state candidates.

Then the events should trigger the High Level Triggers (HLT1, HLT2) with different requirements depending on the run period (see appendix A).

4.2 Preselection and particle identification

After the trigger requirements are passed, the reconstructed candidates are selected according to their track and vertex quality as well as according to their kinematics. The kaon and pion tracks should be of good quality and shouldn't originate from a primary vertex. The two particles are required to have a transverse momentum larger than 250 MeV/c and are identified thanks to the RICH detector. The reconstructed K^{*0} candidate should have a mass within 100 MeV/c^2 around the K^{*0} mass. The dielectron candidate is required to have a good quality vertex and to have a transverse momentum larger than 500 MeV/c. Moreover, one requires the vertex formed by the electron, positron, kaon and pion tracks to be of a good quality and to be displaced from any primary vertex. Finally, the opening angles between any two particles is required to be bigger than 0.5 mrad to avoid clone tracks in the decay. An exception is made for the angle between the two electrons in the gamma q^2 since in this region the dielectron system is expected to share the same VELO segment and have a zero opening angle. Indeed, for the gamma q^2 selection the opening angle cut between the two electrons is not applied, while the selection is kept in the very low q^2 bin. A global event cut is also applied, based on the number of hits detected by the SPD detector.

Finally, the particle identification (PID) selection is made using a neural network based response called ProbNN and the PID variables. The ProbNN variables consist in a probability of a track to be of a given species, determined by combining all subdetectors and tracking information. The PID variables are obtained as a sum of differences between the log likelihood of being of a given species and of being a pion, where the log likelihoods come from the RICH and calorimeter systems. In this analysis, two different electron identification selections are studied.

4.3 Background rejection and truth matching

In order to reduce background, a selection is applied based on possible misidentifications and kinematics. An additional cut is applied in the very low q^2 bin requiring the significance σ_{VELO} (4.1) of the distance of the dielectron vertex from the VELO material to be below 0.3.

$$\sigma_{VELO} = \sqrt{\left(\frac{\delta_x}{\sigma_x}\right)^2 + \left(\frac{\delta_y}{\sigma_y}\right)^2 + \left(\frac{\delta_z}{\sigma_z}\right)^2} \tag{4.1}$$

where δ are the real distances between the closest VELO point and the dielectron vertices, and σ are the uncertainties of the vertices positions [6].

In addition to this, the HOP mass [22] of the B^0 candidate is required to be larger than 4800 MeV/c^2. The HOP mass is used to take into account the missing energy due to bremsstrahlung emission and reject partially reconstructed and combinatorial background. Indeed, one can define $\alpha_{HOP} = p_T(K^{*0})/p_T(e^+e^-)$ (where p_T is the transverse momentum with respect to the B direction) and $p_{corr}(e^+e^-) = \alpha_{HOP} \cdot p(e^+e^-)$ and use the p_{corr} to compute the corrected invariant mass $m_{HOP}(K^+\pi^-e^+e^-)$ [6]. If α_{HOP} differs from unity, some energy is missing in the final state. In case of the signal $B^0 \to K^{*0}e^+e^-$, the missing energy is mainly due to bremsstrahlung photons emitted in the same direction as the electron pair. However, in the case of partially reconstructed or combinatorial background, there is no reason for the missing particles to be emitted in the same direction as the electron pair.

Another powerful variable in rejecting background is the MVA resulting from a MultiVariate Analysis. Within the $\mathcal{R}_X$ analysis two multivariate classifiers are available, one that aims to fight the combinatorial (MVA) and another one aiming at fighting the partially reconstructed backgrounds (PRMVA). The same requirement of the low q^2 analysis is kept in very low and gamma q^2, being that MVA > 0.5 and PRMVA > 0.5. The case for which no requirement is asked on the PRMVA is also studied to simplify comparisons with [6] where only combinatorial MVA was used.

For the Monte-Carlo simulations, truthmatching requirements are also applied and background categories are selected depending on the signal or background nature of the sample.

5 Participating backgrounds

Several backgrounds can pollute and mimic the signal looked for in $B^0 \to K^{*0}e^+e^-$ reconstructed candidates. Indeed, the rare-nature of such decay (*i.e.* its very small branching fraction) allows several other decays to enter and mimic the same final states. The backgrounds considered in this study are discussed here following what has been done in [6].

5.1 Semi-leptonic background

The most important background for $B^0 \to K^{*0}e^+e^-$ is the semi-leptonic $B^0 \to D^-(\to K^{*0}(\to K^+\pi^-)e^-\overline{\nu_e})e^+\nu_e$, which has the same final state as the signal (due to the non reconstruction of the neutrinos) and has a branching ratio four times larger than the signal one. In the analysis [6], the contribution of semi-leptonic background is reduced from $\sim 200\%$ to $\sim 6\%$ by a cut on $|\cos(\theta_L)| < 0.8$. In this study, in order to be consistent with the RX framework, this cut is replaced by $m(K^+\pi^-e^-) > 1880$, which is similar to $\cos(\theta_L) < 0.8$ and have the same rejection power of a cut on $|\cos(\theta_L)|$ for semileptonic backgrounds. This cut is thus asymmetric in this work compared to [6]. However, given the combinatorial-like shape nature of the semi-leptonic backgrounds and the high rejection power of multi-variate classifier selections, the expected shape of this background is the same as the combinatorial one which is modelled according to what is described later in the document. Indeed, the combinatorial background and semileptonic one are very difficult to disentangle, therefore they are fitted together under the combinatorial background label.

5.2 $B^0 \to K^{*0}\gamma(\to e^+e^-)$ leakage

The leakage of the $B^0 \to K^{*0}\gamma(\to e^+e^-)$ decay in the very low q^2 bin is estimated by the analysis [6] to reach 25% of the signal channel when no specific cut is applied. However, as the majority of the photon conversion happens in the material of the VELO detector, applying a cut on the distance between the dielectron vertex position and the VELO material should remove a large part of this contamination. In the analysis, the optimal cut is measured to be $\sigma_{VELO} \equiv$ `JPsi_VMI_D` > 0.3, which is applied to the data samples in the very low q^2 region. With this veto, they estimated the contribution of the $B^0 \to K^{*0}\gamma(\to e^+e^-)$ to be about 2%. Adapting this number to the very low q^2 range of this study, it corresponds to a $\sim$ 2.5% contamination of the signal channel. This background is not modelled and included in the mass fit for this study and in order to finalise the measurement in the very low q^2 region, either a systematic or inclusion of such component will be required.

5.3 $B^0 \to K^{*0}\eta$ and $B^0 \to K^{*0}\pi^0$ backgrounds

Another source of backgrounds is the $B^0 \to K^{*0}\eta$ and $B^0 \to K^{*0}\pi^0$ decays. In both cases, the η/π^0 decays into $e^+e^-\gamma$ and either the photon is not recovered but has a small enough energy so that $m(K^+\pi^-e^+e^-)$ still peaks at the B^0 mass, or it is recovered but wrongly associated to a bremsstrahlung photon. Even though these decay have a lower branching fraction than the signal one, their contribution needs to be evaluated, as their phase space is mostly located in the q^2 region studied. In the analysis [6], the contribution of the $B^0 \to K^{*0}\pi^0$ decay is estimated to be between 1 and 4 % of the signal channel depending on the run period and trigger category, and the contribution of the $B^0 \to K^{*0}\eta$ is estimated to be between 6 and 12%. Since the very low q^2 range is narrower in this study as well as the selection being slightly different than in [6], these numbers and constraints have been recomputed.

For the $B^0 \to K^{*0}\eta$ decay, the MC simulation for the $\eta \to e^+e^-\gamma$ decay is generated without any physics model except for the momentum conservation and two samples are generated to boost statistics in the q^2 region of interests (see step-like behaviour in 5.1). The resulting dielectron mass distribution is thus very different from the expected one. To correct this, two MC samples of `Bd2KstEtaEEG` are added together and reweighted. The first one is the one generated with a simple phase space model and the second one is generated imposing $m(e^+e^-) < 60$ MeV/c^2. After reweighting, the sample matches the theoretical shape as can be seen on figure 5.1.

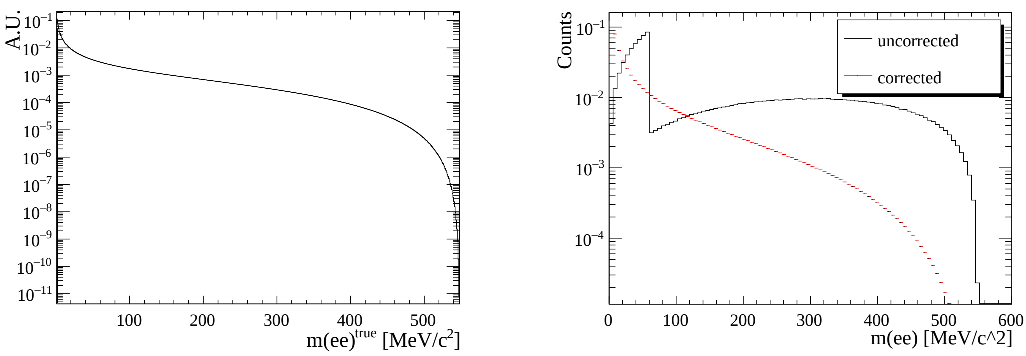

(a) Theoretical shape (taken from [6])

(b) MC samples before and after reweighting (all years and polarities)

FIGURE 5.1: Correction of the $B^0 \to K^{*0}\eta$ MC sample to match theory

The case where the η/π^0 decays into two photons can be a source of background for the $B^0 \to K^{*0}\gamma(\to e^+e^-)$ signal in the gamma q^2 bin. In this case, one of the two photons is missed, or more likely, recovered as a bremsstrahlung photon.

For both the very low and the gamma q^2 bins, the corresponding $B^0 \to K^{*0}\eta(\to e^+e^-\gamma)/B^0 \to K^{*0}\eta(\to \gamma\gamma)$ and $B^0 \to K^{*0}\pi^0(\to e^+e^-\gamma)/B^0 \to K^{*0}\pi^0(\to \gamma\gamma)$ decays are modelled and added to the total data fits and their contribution is constrained according to the efficiency ratios estimation and branching ratios.

5.4 Other specific backgrounds and misidentifications

Other decay channels can contribute to the total data. Most of them are due to a misidentification of one or more particles. From the analysis [6], one can consider the following ones.

$B_s^0 \to \phi e^+ e^-$: In this decay, the ϕ decays into K^+K^- and one of the kaons can be misidentified as a pion. The ϕ is thus reconstructed as a K^{*0} with a low $m(K^+\pi^-)$ mass. These events are rejected by applying a veto cut $m(K^+(\pi^- \to K^-)) > 1040$ MeV/c^2.

$B^+ \to K^+ e^+ e^-$: If a random pion observed in the event is wrongly taken as coming from the signal decay or if the kaon is misidentified as a pion and a random kaon is wrongly associated to the signal, this decay may pollute the signal. However, the dielectron pair is not coming from a virtual photon in this case, so the decay do not have a photon pole and this background shouldn't be present at very low q^2. The analysis [6] estimated the participation of this background to less than 0.03%. It is thus neglected for the very low q^2 study.

$\Lambda_b^0 \to pK^- e^+ e^-$: Events from this decay can pass the selection if the proton is misidentified as a pion or if there is a double misidentification of the proton as a kaon and the kaon as a pion. Although some elements of this decay are not well known, the analysis [6] estimated the participation of the background to be between 0.45 and 0.8 % depending on the run period. These numbers being below the percent level, this background is neglected too.

Semi-leptonic cascades : A contamination from semi-leptonic cascades such as $B^0 \to D^-(\to K^{*0}(\to K^+\pi^-)\pi^-)e^+\nu_e$, $B^0 \to \overline{D}^0(\to K^+\pi^-)\pi^- e^+\nu_e$ or $B^0 \to D^{*-}(\to D^0(\to K^+\pi^-)\pi^-)e^+\nu_e$ can pollute the signal if a pion is misidentified as an electron. Since no peaking behaviour is observed by the analysis [6] around the D^-/D^0 masses when looking at $m(K^+(e^- \to \pi^-)$ and $m(K^+\pi^-(e^- \to \pi^-)$, these backgrounds are neglected.

$B^0 \to K^{*0}\pi^+\pi^-$: If the two pions of this decay are misidentified as electron/positron, a contamination from $B^0 \to K^{*0}\pi^+\pi^-$ can appear. By studying the $m(e^+e^- \to \pi^+\pi^-)$ spectrum, the analysis [6] estimated the contamination of this decay to be below the percent level in the very low q^2 region, and this background is thus neglected for the present study.

5.5 Partially reconstructed and combinatorial backgrounds

The last remaining backgrounds are the partially reconstructed and the combinatorial backgrounds, which are briefly summarised in the following. As discussed in section 4, several cuts are implemented in order to reduce their contribution. In particular, a veto cut on the HOP mass is applied to reduce the partially reconstructed background contamination, and a MultiVariate Analysis (MVA) classifier is used to reduce the combinatorial background contamination. Also, another dedicated partially reconstructed MVA is used specifically aiming to suppress partially reconstructed background. What remains after those selections however is modelled and added to the mass fit.

Partially reconstructed background: The partially reconstructed background is coming mostly from $B^+ \to K_1(1270)(\to K^+\pi^-X)e^+e^-$ and $B^+ \to K_1(1270)(\to K^+\pi^-X)\gamma(\to e^+e^-)$ where the X is not reconstructed, it is modelled using an MC sample of $B^+ \to K_1(1270)(\to K^+\pi^-X)e^+e^-$ events. The relative abundance to signal of partially reconstructed is fitted so that it is shared between gamma and very low q^2.

Combinatorial background: For the combinatorial background a sample of real data where same sign electrons are reconstructed together with a K^{*0} is used. Same sign data corresponds to reconstructed $K^{*0}e^+e^+$ and $K^{*0}e^-e^-$ candidates and is used to model the shaping of combinatoric induced by the HOP and MVA requirements. Such data are generally found to be a good proxy for the combinatorial modelling and in particular in the understanding of sculpting effects of combinatoric due to the selections applied.

6 Mass fits

In order to perform the data fit for each trigger and run period, one has to first fit the different expected components. The fits of signals and partially reconstructed backgrounds are performed on simulated samples for both very low and gamma q^2.

All the fits are performed and presented here on the 4200–6200 MeV/c^2 mass range but depending on the various cases tested, the final fits on data can be performed in a narrower mass range.

6.1 Signal fits

The very low $B^0 \to K^{*0}e^+e^-$ and the gamma $B^0 \to K^{*0}\gamma(\to e^+e^-)$ signals are respectively fitted using `Bd2KstEE` and `Bd2KstGEE` MC samples. The signal shapes are modelled by double-sided crystal ball PDFs (6.1).

$$f_{dscb}(x,\mu,\sigma,\alpha_L,\alpha_R,n_L,n_R) = N \times \begin{cases} A_L(B_L - \frac{x-\mu}{\sigma})^{-n_L} & \text{for } \frac{x-\mu}{\sigma} \leq -|\alpha_L| \\ A_R(B_R - \frac{x-\mu}{\sigma})^{-n_R} & \text{for } \frac{x-\mu}{\sigma} \geq |\alpha_R| \\ \exp(-\frac{(x-\mu)^2}{2\sigma^2}) & \text{for } -|\alpha_L| < \frac{x-\mu}{\sigma} < |\alpha_R| \end{cases} \tag{6.1}$$

where N is a normalisation factor and

$$A_L = \left(\frac{n_L}{|\alpha_L|}\right)^{n_L} \exp\left(-\frac{\alpha_L^2}{2}\right), B_L = \frac{n_L}{|\alpha_L|} - |\alpha_L|$$

$$A_R = \left(-\frac{n_R}{|\alpha_R|}\right)^{n_R} \exp\left(-\frac{\alpha_R^2}{2}\right), B_R = -\frac{n_R}{|\alpha_R|} + |\alpha_R|$$

Due to low statistics in the bremsstrahlung (brem) category corresponding to two or more photons emitted, this category is merged with the category corresponding to one brem photon emitted.

The categories 0G (zero brem photon emitted) and 1G (one or more brem photons emitted) are fitted separately and then added together in the total data fit with their respective fractions, extracted from the simulation. The consideration of a systematic effect could be required on this distribution between the 0G and 1G categories, but it should be a small effect as verified in many other analyses in LHCb. The fits are performed for a total of 6 categories: L0I and L0L and the three different run periods R1, R2p1 and R2p2.

The results for R2p2 are shown on figure 6.1 for the very low q^2 and on figure 6.2 for the gamma q^2. The bremsstrahlung fractions, taken directly from their distribution in simulation are presented in table 6.1 for R2p2. The results for other run periods are shown in appendix B.

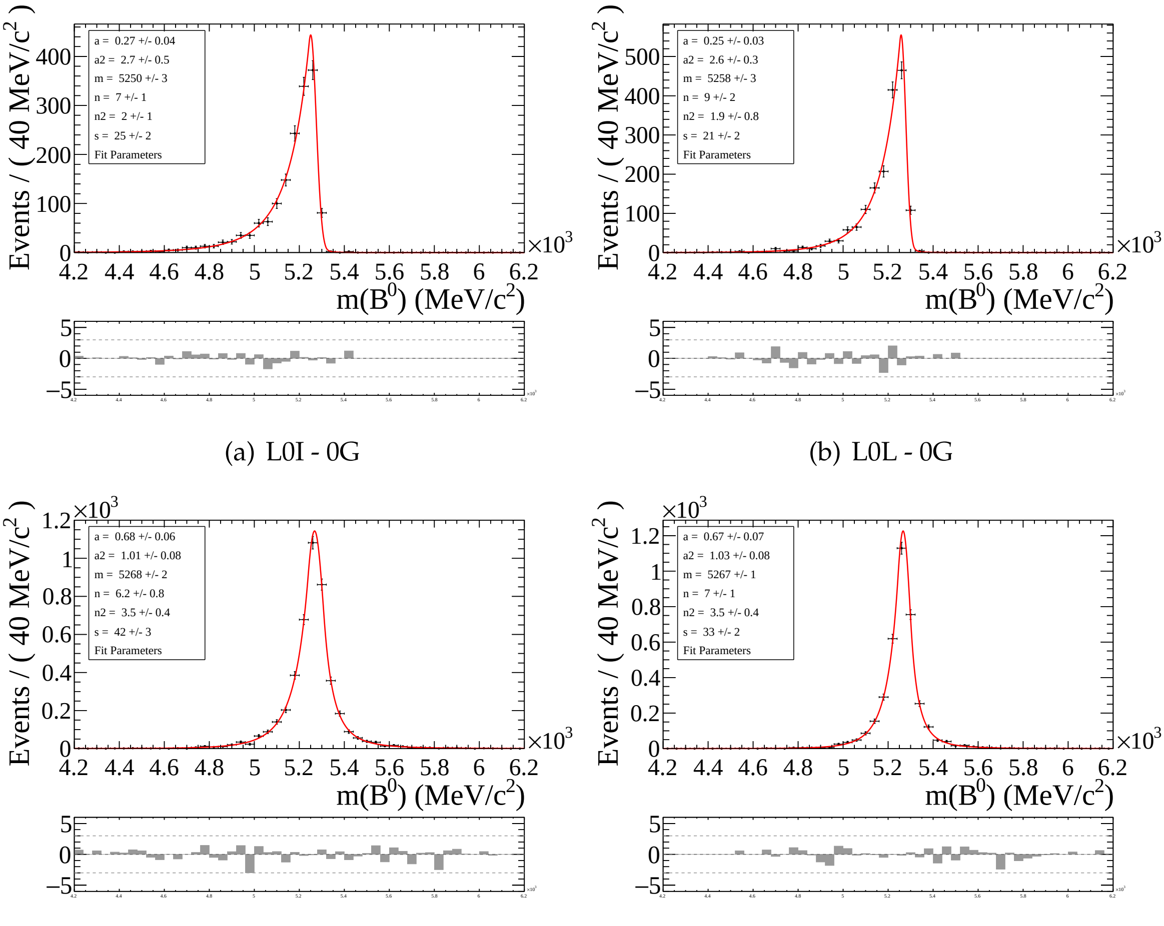

(a) L0I - 0G

(b) L0L - 0G

(c) L0I - 1G

(d) L0L - 1G

FIGURE 6.1: Signal MC fit of $B^0 \to K^{*0}e^+e^-$ candidates in the very low q^2 for R2p2

	0G	1G
L0I, very low	0.271	0.729
L0L, very low	0.334	0.666
L0I, gamma	0.278	0.722
L0L, gamma	0.340	0.660

TABLE 6.1: MC fraction of events with 0 brem photon emitted (0G) and 1 or more brem photon emitted (1G) for R2p2

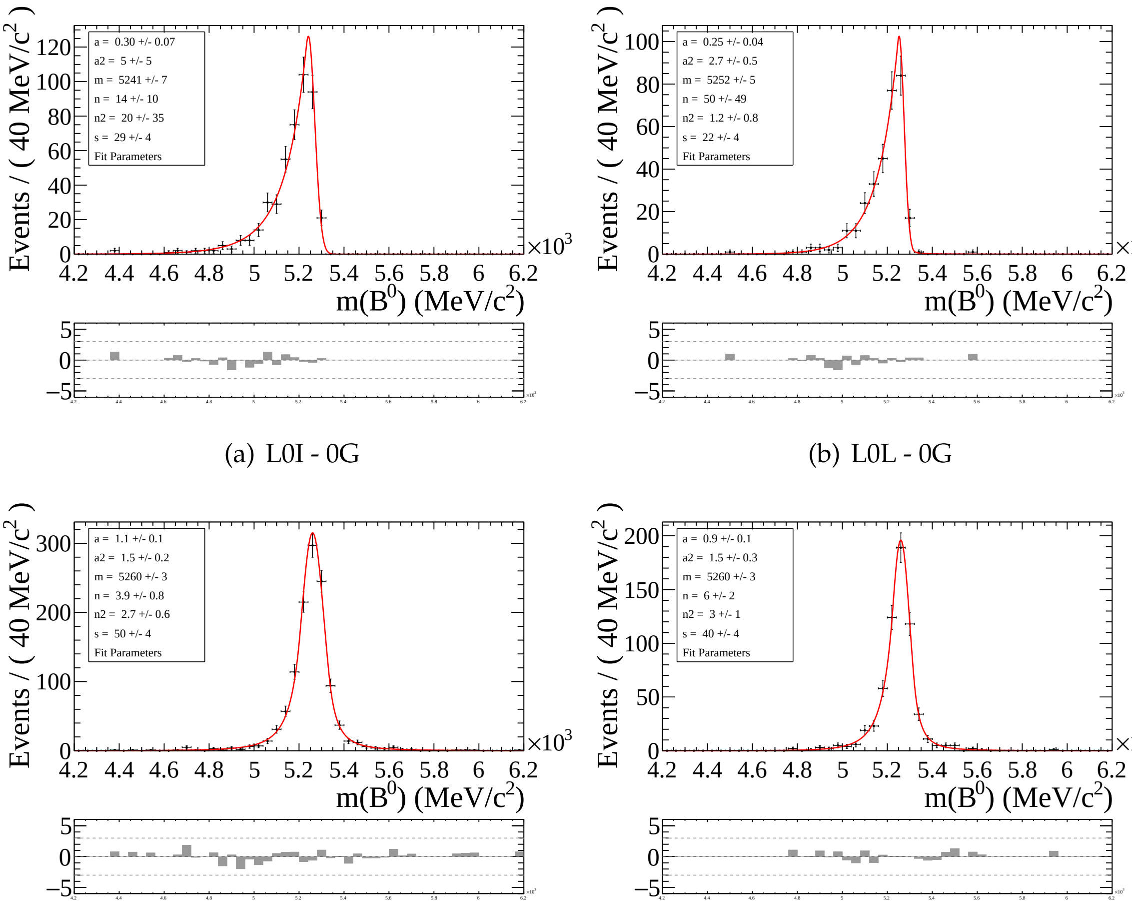

(a) L0I - 0G (b) L0L - 0G

(c) L0I - 1G (d) L0L - 1G

FIGURE 6.2: Signal MC fit of $B^0 \to K^{*0}\gamma(\to e^+e^-)$ candidates in the gamma q^2 for R2p2

6.2 Specific backgrounds

The specific backgrounds that cannot be neglected and thus taken into account in the mass fit are the $B^0 \to K^{*0}\eta$ and $B^0 \to K^{*0}\pi^0$ decays. The case where the η / π^0 decays into $e^+e^-\gamma$ is modelled for the fit in the very low q^2 bin. For the fit in the gamma q^2, one can consider the contribution of the $B^0 \to K^{*0}\eta$ and $B^0 \to K^{*0}\pi^0$ decays, but with the η / π^0 decaying into two photons, where one of them converts into a dielectron pair.

For the very low q^2 bin, the reweighted `Bd2KstEtaEEG` and the `Bd2KstPi0EEG` MC samples are used and the shapes are fitted with double-sided crystal ball PDFs (6.1). For the gamma q^2 bin, the MC samples `Bd2KstEtaGGEE` and `Bd2KstPi0GGEE` are used and the shapes are fitted with a RooKeysPdf. This function is a kernel density estimation [23] which uses an adaptative algorithm to model empirically the distribution of an arbitrary dataset with a superposition of Gaussian kernels (one for each data point). In the very low region, the samples are fitted separately for the L0I and L0L trigger categories while the two categories are fitted together in the gamma region due to the limited statistic in the corresponding samples. For the same reason, all run periods are fitted together for the two q^2 regions.

The results for $B^0 \to K^{*0}\eta$ are shown in figures 6.3 and 6.4 for respectively the very low and the gamma q^2 bins, and the results for $B^0 \to K^{*0}\pi^0$ are shown in figures 6.5 and 6.6.

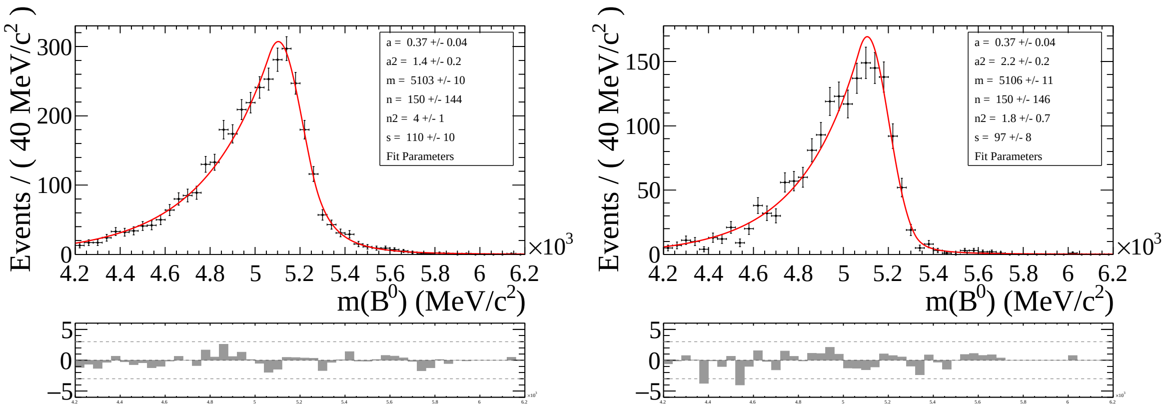

(a) L0I (b) L0L

FIGURE 6.3: MC fit of $B^0 \to K^{*0}\eta(\to e^+e^-\gamma)$ candidates in the very low q^2 for all run periods merged

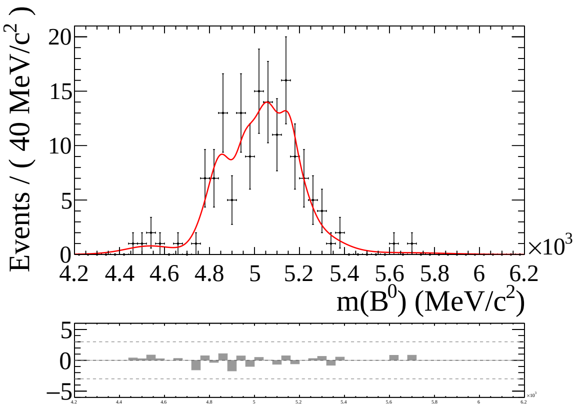

(a) L0I+L0I

FIGURE 6.4: MC fit of $B^0 \to K^{*0}\eta(\to \gamma(\to e^+e^-)\gamma)$ candidates in the gamma q^2 for 2012+2016 run periods and triggers merged

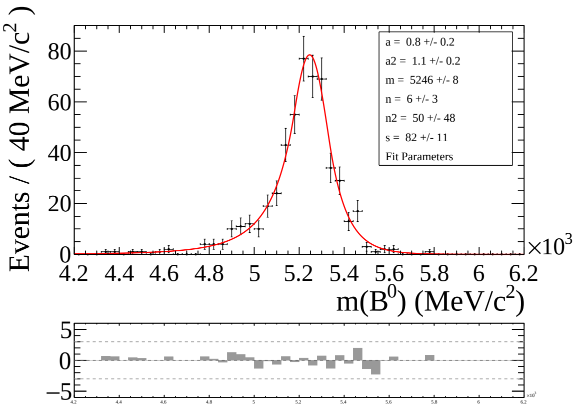

(a) L0I

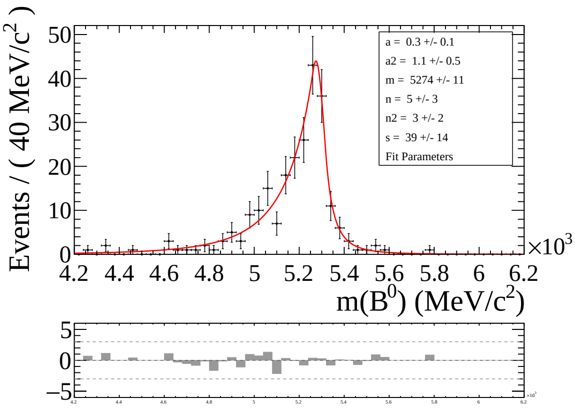

(b) L0L

FIGURE 6.5: MC fit of $B^0 \to K^{*0}\pi^0(\to e^+e^-\gamma)$ candidates in the very low q^2 for all run periods merged

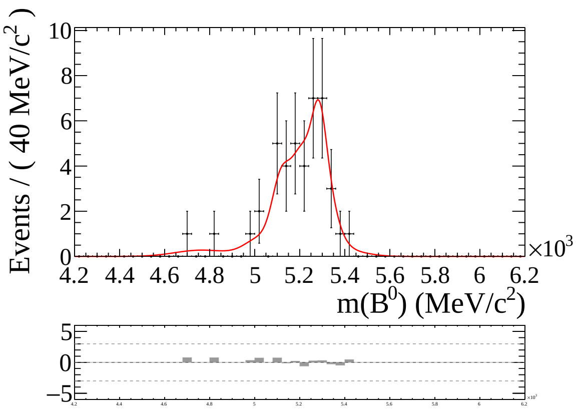

(a) L0I+L0L

FIGURE 6.6: MC fit of $B^0 \to K^{*0}\pi^0(\to \gamma(\to e^+e^-)\gamma)$ candidates in the gamma q^2 for 2012+2016 run periods and triggers merged

6.3 Partially reconstructed background

For the partially reconstructed background modelling, the decay $B^+ \to K_1 e^+e^-$ is used as a proxy and the `Bu2K1EE` MC sample is fitted in both very low and gamma q^2 regions using a double-sided crystal ball PDF. As for the specific backgrounds, the L0I and L0L trigger categories are fitted separately but the R1, R2p1 and R2p2 run periods are fitted together.

The results are respectively shown on figures 6.7 and 6.8 for the very low and gamma q^2 bins.

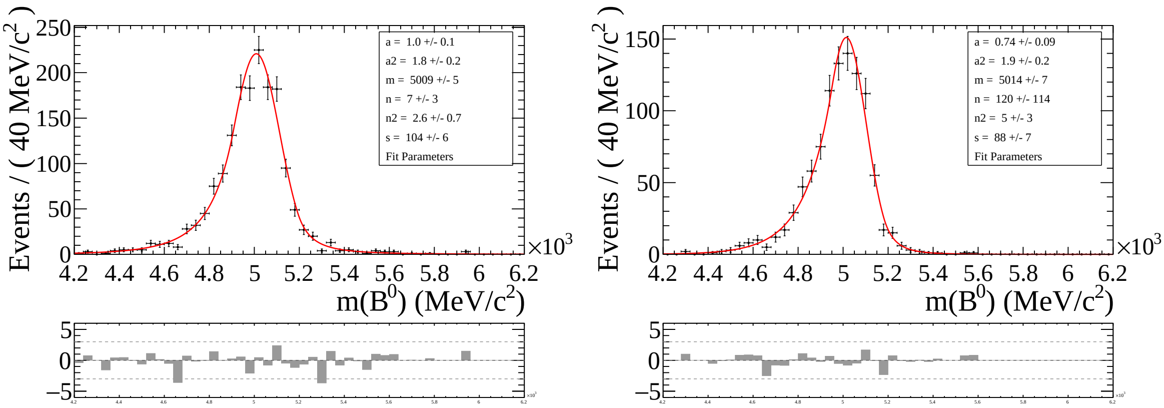

(a) L0I (b) L0L

FIGURE 6.7: MC fit $B^+ \to K_1 e^+ e^-$ candidates for partially reconstructed background in the very low q^2 for all run periods merged

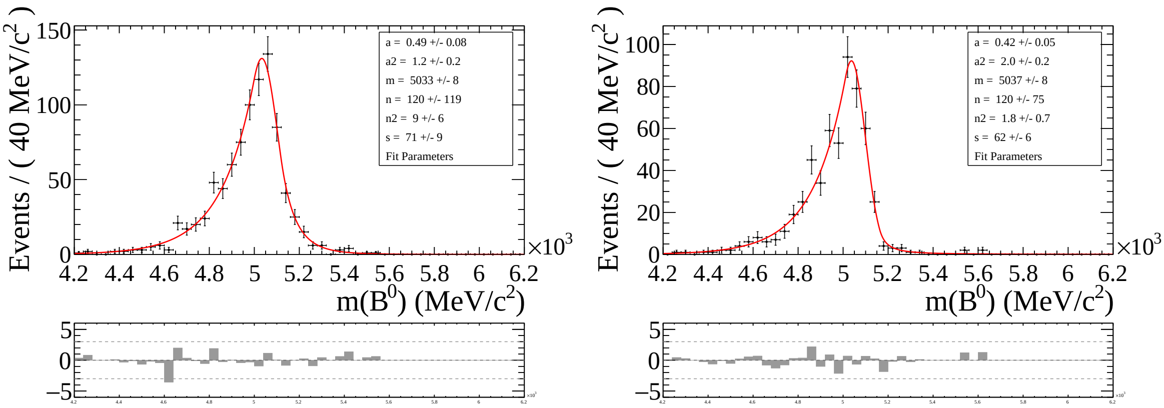

(a) L0I (b) L0L

FIGURE 6.8: MC fit $B^+ \to K_1 e^+ e^-$ candidates for partially reconstructed background in the gamma q^2 for all run periods merged

6.4 Combinatorial background

The last component that needs to be taken into account into the total data fit is the combinatorial background. The PRMVA cut removing a part of background in the left tail, the combinatorial background is modelled with an ExpTurnOn PDF (6.2) directly in the total data fit.

The parameters of the PDF which are in charge of the shaping of a pure combinatorial shape (m_0, s_E) are expected to match the parameters found by fitting the `LPTSS` sample, corresponding to data with same sign dielectron final states.

$$f_{ExpTurnOn}(x, m_0, s_E, b) = \frac{e^{bx}}{1 + e^{-s_E(x-m_0)}} \tag{6.2}$$

The distributions obtained in same sign data after the full selection for the gamma and very low q^2 regions are shown on figure 6.9 for all run periods merged. The values obtained fitting them to parameterise the sculpting effect (m_0, s_E) with an ExpTurnOn shape are displayed in table 6.2. The b parameter of the ExpTurnOn is left free in the total data fit.

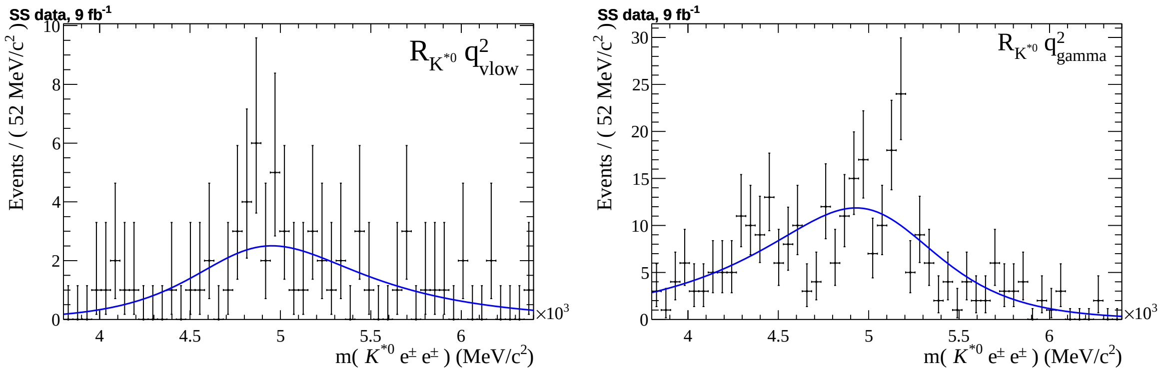

(a) very low q^2 (b) gamma q^2

FIGURE 6.9: Fits of the same sign lepton data used as a proxy for the combinatorial background shapes for all run periods merged

	m_0	s_E
very low q^2	4830±225	0.0049±0.0011
gamma q^2	5069±118	0.0048±0.0004

TABLE 6.2: Combinatorial background ExpTurnOn parameters extracted from same sign data fit

7 Angular fits

In order to have a validation of the yields of the different components found with the mass fits, an angular fit of $\cos\theta_K$ is performed. As described in section 1, θ_K is the angle between the B^0 and the K^+ directions in the K^{*0} rest frame. As for the mass fits, the different components are fitted for each run period and trigger categories using MC simulation samples in very low and gamma q^2 regions. The same samples as the ones for the mass fits are used for the angular fits.

7.1 Signal shapes

The signal $B^0 \to K^{*0}e^+e^-$ for the very low q^2 bin and $B^0 \to K^{*0}\gamma(\to e^+e^-)$ for the gamma q^2 bin are modelled by order 4 polynomials. The shapes being the same for the 0G and 1G bremsstrahlung categories, the two are fitted together for each trigger category and for each run period separately. Moreover, the PDFs are required to be positively defined on the fitting range [-1,1].

The results for R2p2 are shown on figure 7.1 for the very low q^2 bin and on figure 7.2 for the gamma q^2 bin. The results for other run periods are shown in appendix C.

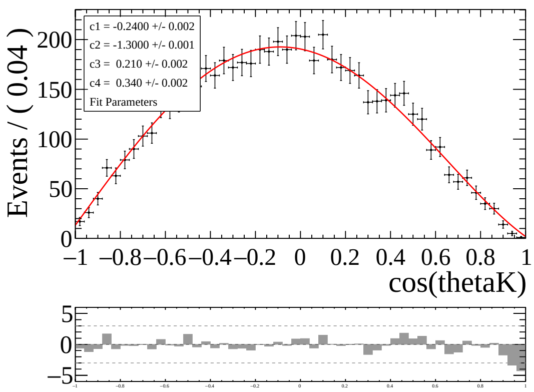

(a) L0I

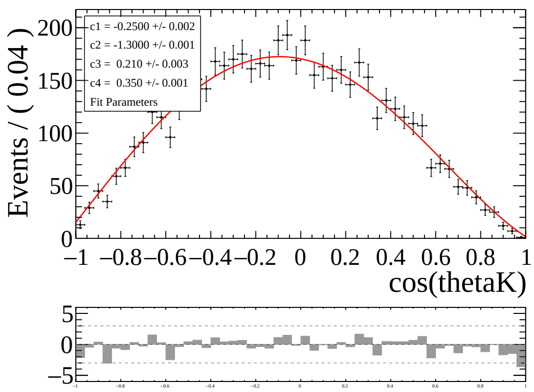

(b) L0L

FIGURE 7.1: Signal MC fit of $B^0 \to K^{*0}e^+e^-$ candidates in the very low q^2 for R2p2

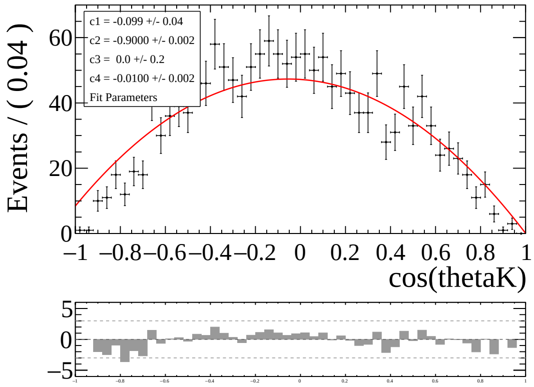

(a) L0I

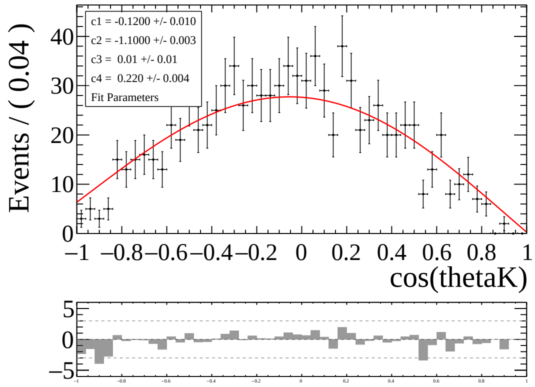

(b) L0L

FIGURE 7.2: Signal MC fit of $B^0 \to K^{*0}\gamma(\to e^+e^-)$ candidates in the gamma q^2 for R2p2

7.2 Specific backgrounds

The $B^0 \to K^{*0}\eta$ and $B^0 \to K^{*0}\pi^0$ backgrounds are fitted using the respective MC samples corresponding to $B^0 \to K^{*0}\eta(\to e^+e^-\gamma)$ for the very low q^2 and $B^0 \to K^{*0}\eta(\to \gamma(\to e^+e^-)\gamma)$ for the gamma q^2. For the very low q^2 case, the shapes are fitted with order 5 Chebychev polynomials defined in equation (7.1), and constrained to be positive in the whole fit range. The backgrounds are fitted for L0I and L0L categories separately but for all run periods merged. For the gamma q^2 case, due to very low statistics in the sample, the shapes are fitted with RooKeysPdf for all triggers and run periods merged.

$$T(x) = T_0(x) + c_1T_1(x) + ... + c_5T_5(x)$$
$$T_0(x) = 1 \quad ; \quad T_1(x) = x \quad ; \quad T_{n+1}(x) = 2xT_n(x) - T_{n-1}(x) \tag{7.1}$$

The fits for $B^0 \to K^{*0}\eta$ are shown in figures 7.3 and 7.4 for respectively the very low and the gamma q^2 bins, and the results for $B^0 \to K^{*0}\pi^0$ are shown in figures 7.5 and 7.6.

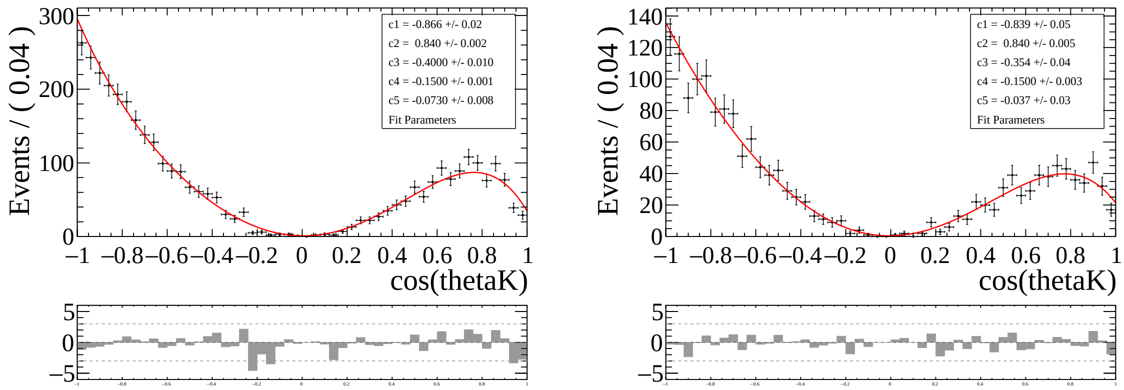

(a) L0I

(b) L0L

FIGURE 7.3: MC fit of $B^0 \to K^{*0}\eta(\to e^+e^-\gamma)$ candidates in the very low q^2 for all run periods merged

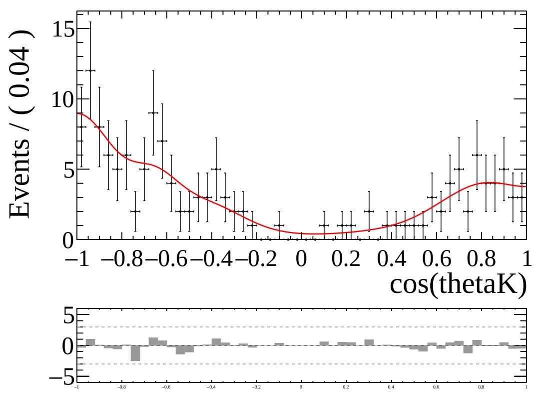

(a) L0I+L0I

FIGURE 7.4: MC fit of $B^0 \to K^{*0}\eta(\to \gamma(\to e^+e^-)\gamma)$ candidates in the gamma q^2 for 2012+2016 run periods and triggers merged

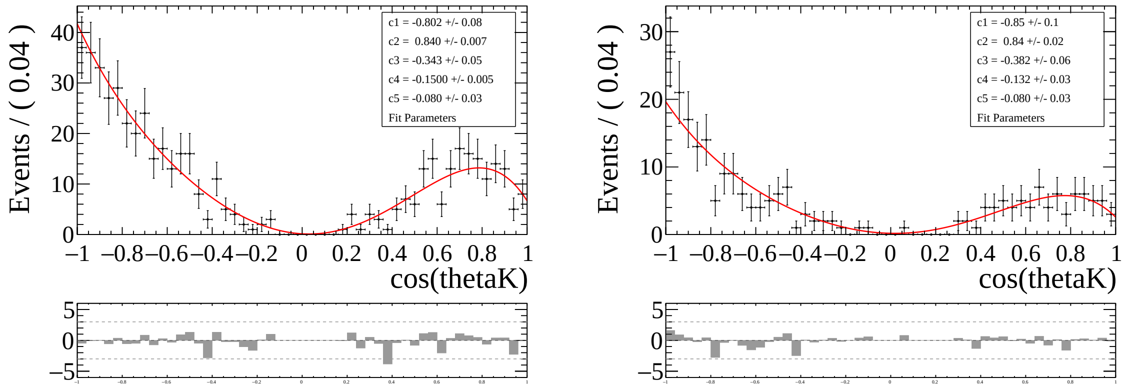

(a) L0I (b) L0L

FIGURE 7.5: MC fit of $B^0 \to K^{*0}\pi^0(\to e^+e^-\gamma)$ candidates in the very low q^2 for all run periods merged

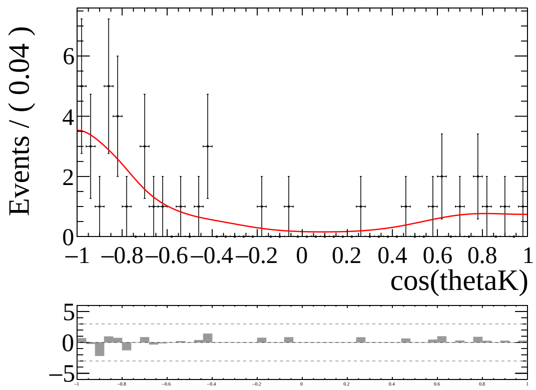

(a) L0I+L0L

FIGURE 7.6: MC fit of $B^0 \to K^{*0}\pi^0(\to \gamma(\to e^+e^-)\gamma)$ candidates in the gamma q^2 for 2012+2016 run periods and triggers merged

7.3 Partially reconstructed background

The $B^+ \to K_1 e^+e^-$ decay, which is used as a proxy for the partially reconstructed background, is fitted using a RooKeysPdf for both the very low and the gamma q^2. As for the mass fits, the L0I and L0L samples are fitted separately but the three run periods are merged together.

The results can be seen on figures 7.7 and 7.8 for the very low and gamma q^2 bins respectively.

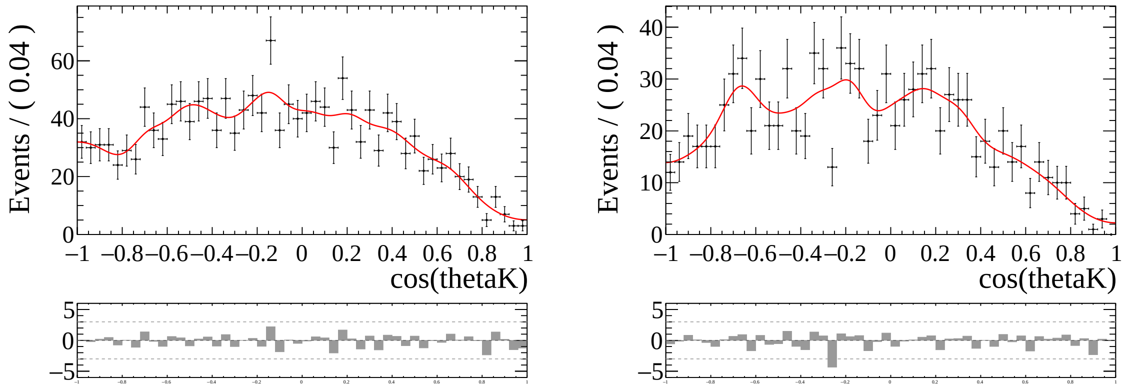

(a) L0I (b) L0L

FIGURE 7.7: MC fit $B^+ \to K_1 e^+ e^-$ candidates for partially reconstructed background in the very low q^2 for all run periods merged

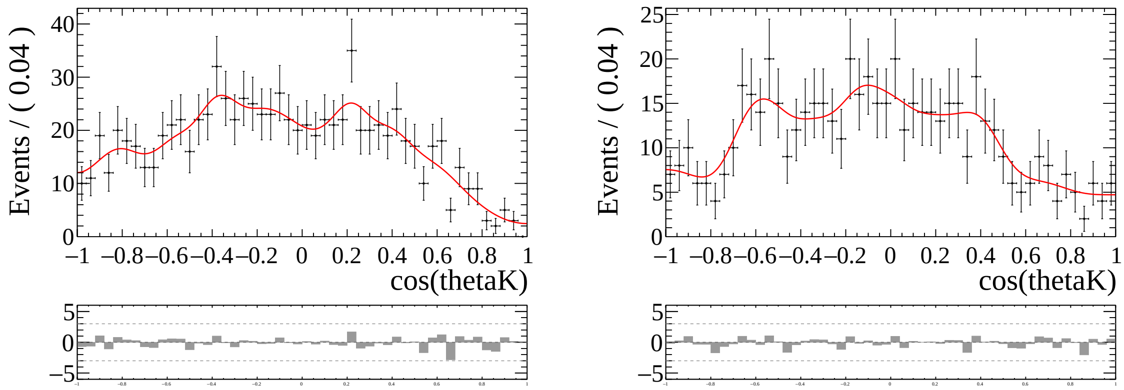

(a) L0I (b) L0L

FIGURE 7.8: MC fit $B^+ \to K_1 e^+ e^-$ candidates for partially reconstructed background in the gamma q^2 for all run periods merged

7.4 Combinatorial background

Contrary to the mass fits, the combinatorial background is fitted individually and the PDF is included in the total angular fit instead of being directly fitted with the total data. The same sign data sample with the two leptons required to have the same sign is thus fitted with a RooKeysPdf for each trigger category but with all run periods merged as for the other backgrounds.

The results are shown on figure 7.9 for the very low q^2 bin and on figure 7.10 for the gamma q^2 bin.

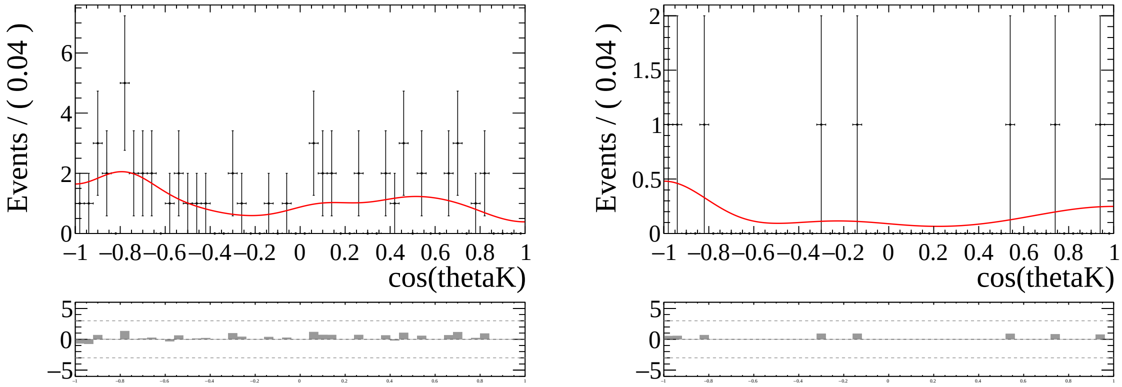

(a) L0I (b) L0L

FIGURE 7.9: Fit of the same sign lepton data used as a proxy for the combinatorial background in the very low q^2 for all run periods merged

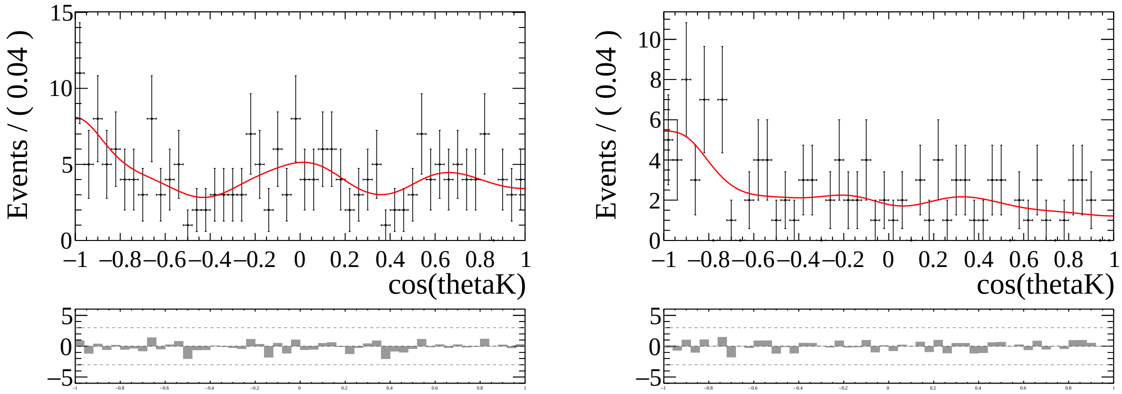

(a) L0I (b) L0L

FIGURE 7.10: Fit of the same sign lepton data used as a proxy for the combinatorial background in the gamma q^2 for all run periods merged

8 Efficiency and corrections to simulation

The efficiency of a selection is defined as the number of events passing the selection divided by the total number of generated events. The efficiency computation relies thus directly on the MC simulations, and so does the modelling of the fits components. One must therefore make sure that they reproduce well the data. For the MC samples of LHCb this is however not the case, leading to the necessity of correcting them. The corrections performed are the ones developed in the RX framework [7] and are specified in this section as they are handled in the efficiency calculations.

First, one has to take into account the LHCb acceptance. In the case of the $K^{*0}e^+e^-$ decay, the dependency of it as a function of the q^2 is studied and the ϵ_{geo} is evaluated in the effective q^2 region of interest. To do so, a sample with a 4π angular distribution is produced and cuts corresponding to the LHCb angular acceptance are applied by hand to evaluate the corresponding efficiency. The geometrical efficiency on the signal MC sample is therefore measured as the number of events [in the very low q^2 bin and in the LHCb acceptance] divided by the number of events [in the very low q^2 bin]. The total efficiency is the product of the geometrical efficiency and the efficiency of selection.

The efficiency of the selection is then corrected accounting for the different mis-reproduced quantities in the MC samples. The corrections, consisting of applying weights, are performed on the particle identification, the number of reconstructed tracks in the events parameterising the detector occupancy, the B kinematics, the triggers, and the tracking reconstruction. They are applied one on top of each other in the order listed above and are described in the following.

8.1 Particle identification

The measurement of the PID efficiency is performed in a data-driven way for the kaons and pions and with a ratio of data over simulation for the electrons. In the first case, the calibration samples are provided by the `PIDCalib` package. The weights resulting from the PID maps act as efficiencies and are used in replacement of the PID selection cut for the estimation of the total efficiency of selection. In the case of electron final states, a weight ratio map is used parameterising $\frac{\epsilon_{PID}(data)}{\epsilon_{PID}(MC)}$ which allows to use the weight given the simulated sample being selected in PID for the determination of efficiencies with PID corrections in.

The efficiency maps are computed as a function of the kinematics of the final states: particle momentum p (transverse momentum p_T for electrons), the pseudo-rapidity η and the multiplicity `nTracks`. Two types of maps are computed: ID maps, consisting in measuring the rate of correctly identified particles; and mis-ID maps, consisting in measuring the rate of misidentification of a given particle to another given particle. The calibration samples for the kaons and pions are samples of $D^0 \to K^-\pi^+$ events coming from a $D^{*+} \to D^0\pi^+$ and the calibration samples for electrons is a sample of $B^+ \to K^+J/\psi(\to e^+e^-)$ events. The total PID correction to simulation is therefore obtained multiplying the single track final state weight obtained convoluting the efficiency (or efficiency ratio) maps in the simulated samples.

8.2 Electron track reconstruction

The efficiency correction of the electron tracks reconstruction [24] is performed as an efficiency ratio of data over simulation. Both data and MC efficiency maps are measured as the rate of electron tracks reconstructed as traversing the whole detector (long tracks) given that they are reconstructed in the VELO. They are computed as a function of the particles transverse momentum p_T, the pseudo-rapidity η, and ϕ which is a track angular information. The final weight applied to the corresponding efficiency is the product of the weights of each of the two electron tracks.

8.3 B kinematics, multiplicity and reconstruction

For these corrections to simulation, the muonic final state channel $B \to KJ/\psi(\to \mu^+\mu^-)$ is used and the corrections to apply to simulation are estimated training a multivariate classifier which parameterises the data over simulation discrepancy in the p_T, p, η of the reconstructed B candidates and n_{Tracks}. Such corrections are then ported to the electron mode final states. The reason behind such approach is that the better resolution in the measured kinematics of the B candidates obtained using muons in the final states in data allow to access, when comparing them to the simulation, an excellent proxy parameterising the data/simulation mis-modelling of the B hadron kinematic.

This mis-modelling effect, obtained in simulation, is induced by the poorly known Parton distribution functions which are responsible of $b\bar{b}$ production in pp collision in the LHCb acceptance. In order to access in an unbiased way the data/simulation discrepancies for generator level quantities, the muon final states simulated samples is previously corrected for the PID, L0 and HLT triggers effect which can cause additional data/MC discrepancies in the B kinematics.

The differences in track multiplicity in the event between MC and data are mainly coming from: the wrong simulation of low momentum particles; back-splash from particle showers (which ends up being still reconstructed in the trackers); secondary interactions such as photon conversions (which ultimately depend on the simulation of the detector material budget and the interaction of particles with material); and the simulation of soft QCD processes in pp collision.

For what concern the B kinematics differences between data and simulation, such discrepancy is originating from both the way $b\bar{b}$ are generated in simulation and the mis-modelling of reconstruction effects.

For the multiplicity and the generation corrections to simulation, the data/MC differences in `nTracks` and on the B meson momentum p, transverse momentum p_T and pseudo-rapidity η observed in muon mode are used.

For reconstruction related effects, the relevant data/simulation discrepancies depends on the final states of the reconstructed candidates. For this reason, such corrections are obtained comparing data and simulation in the $K^{*0}J/\psi(\to ee)$ decays after having applied also the trigger, PID, kinematics and multiplicity, and HLT corrections to the calibration samples $K^{+,*0}J/\psi(\to ee)$ as described in the next section.

8.4 Trigger

The efficiencies of selecting candidates based on the trigger decisions either at hardware (L0) and software reconstruction (HLT) level should also be correctly determined. Corrections are therefore applied for effects due to mis-modelling of detector, trigger thresholds values used in real data compared to simulation as well as ageing effects which are particularly relevant for the ECAL system. For both the L0 and the HLT requirements, the efficiency on data ϵ_{data} and on the simulation ϵ_{MC} are computed using the TISTOS method and the weights are obtained as the data/MC ratio of efficiencies. Per-particle information quantities are used to correct the trigger efficiency of the L0L category and B hadron kinematic information for the L0I category. The TISTOS method consists in computing the efficiencies for data and simulation as follows:

$$\epsilon = \frac{N_{TIS\&TOS}}{N_{TIS}} \tag{8.1}$$

where TIS and TOS correspond respectively to "Trigger Independent of signal" and "Trigger On Signal" and are defined differently for the different triggers considered.

L0 trigger: Data is analysed in the two trigger categories L0I and L0L exclusive. The efficiencies for these two triggers must thus be accurate. The TIS and TOS categories are described as follows:

- L0I category:
  - TIS tag: Events triggered on L0 by non-signal particle: `B_L0Muon_TIS` or `B_L0HadronTIS` or `B_L0ElectronTIS`
  - TOS tag: Events triggered on L0 level by either a signal lepton or hadron: `E1_L0Electron_TOS` or `E2_L0Electron_TOS` or `B_L0Hadron_TOS`
- L0L exclusive category:
  - TIS tag: Events triggered on L0 by non-signal hadron or muon: `B_L0Hadron_TIS` or `B_L0Muon_TIS`

- *TOS* tag: Events triggered on L0 by a signal hadron: `B_L0Hadron_TOS`

For each trigger category L0I, L0L and for each sample data, MC, a per-event weight parameterising the data/simulation efficiency correction factor is evaluated following equation (8.1) and the corresponding per-event weight is computed as:

$$w_{trig} = \frac{\epsilon^{data}_{trig}}{\epsilon^{MC}_{trig}} \tag{8.2}$$

where $trig = L0I, L0L$.

In the case of the $L0L$ trigger, the category contains the combination of the two electrons, one should thus combine the weights for the two electrons, as can be seen in equation (8.3).

$$w_{L0L} = \frac{1 - (1 - \epsilon^{data}_{L0L}(\texttt{E1}) \cdot \texttt{E1TOS}) \cdot (1 - \epsilon^{data}_{L0L}(\texttt{E2}) \cdot \texttt{E2TOS})}{1 - (1 - \epsilon^{MC}_{L0L}(\texttt{E1}) \cdot \texttt{E1TOS}) \cdot (1 - \epsilon^{MC}_{L0L}(\texttt{E2}) \cdot \texttt{E2TOS})} \tag{8.3}$$

where the property $P(A||B) = P(A) + P(B) - P(A\&B)$ is used and `EiTOS` is 1 if the electron `Ei` is above threshold and 0 otherwise.

For an exclusive category, the exclusive weight is defined as:

$$w_{trig,exclu} = w_{trig} \cdot \frac{1 - \epsilon^{data}_{trig'}}{1 - \epsilon^{MC}_{trig'}} = \frac{\epsilon^{data}_{trig}}{\epsilon^{MC}_{trig}} \cdot \frac{1 - \epsilon^{data}_{trig'}}{1 - \epsilon^{MC}_{trig'}} \tag{8.4}$$

where $trig = L0I, L0L$ and $trig' = L0L, L0I$; $trig \neq trig'$.

HLT trigger: The High Level Trigger efficiency should also account for the differences between data and simulation. For this trigger category, the *TIS* and *TOS* tags are defined as follows:

- *TIS* tag: logical `OR` condition of HLT1 and HLT2 trigger lines fired independently of the signal
- *TOS* tag: logical `AND` condition of HLT1 and HLT2 trigger lines defined in table A.2.

The efficiencies for data and MC are then computed using equation (8.1) and the weight is defined as the ratio of the efficiency on data and the efficiency on simulation.

9 Results

9.1 Total mass fit

The total mass fits are performed adapting the fitter used for the $\mathcal{R}_X$ analysis. The mass fit is obtained fitting simultaneously the $K^{*0}J/\psi(\rightarrow ee), K^{*0}J/\psi(\rightarrow \mu\mu), K^{*0}e^+e^-, vl$ and $K^*\gamma$ final states candidates.

The shapes of the different components in very low and gamma q^2 obtained from simulation are fixed, except for the exponential slope parameter (b) for the combinatorial background. The signal line shape width, parameterised with s_{scale}, encoding the fact that $\sigma_{data} = s_{scale} \cdot \sigma_{MC}$) and the mean mass value, parameterised by m_{shift} encoding $m_{data} = m_{MC} + m_{shift}$ are also free to float but their values are shared between the very low q^2 and the J/ψ mode. For the gamma q^2, those parameters are fully free to float independently of J/ψ mode since the origin of residual mass shape mis-modelling in simulation for converted photons are not of the same nature as in very low and J/ψ channels.

All signal and combinatorial yields are free to float while the $K^{*0}\eta$ and $K^*\pi^0$ background yields are Gaussian constrained according to their expected values obtained via efficiencies and branching ratios consideration in the very-low q^2 (9.1) and gamma q^2 (9.2). The partially reconstructed background in gamma and very-low q^2 ratio to signal yield is shared between gamma and very-low, an additional reason for which the fit is performed in a simultaneous manner.

$$\begin{aligned}
\mathcal{N}(B^0 \rightarrow K^{*0}\eta(\rightarrow e^+e^-\gamma)) = {} & \mathcal{N}(B^0 \rightarrow K^{*0}J/\psi(\rightarrow e^+e^-)) \\
& \cdot \frac{\epsilon_{B^0\rightarrow K^{*0}\eta(\rightarrow e^+e^-\gamma)}}{\epsilon_{B^0\rightarrow K^{*0}J/\psi(\rightarrow e^+e^-)}} \\
& \cdot \frac{\mathcal{B}(B^0 \rightarrow K^{*0}\eta(\rightarrow e^+e^-\gamma))}{\mathcal{B}(B^0 \rightarrow K^{*0}J/\psi(\rightarrow e^+e^-))}
\end{aligned} \tag{9.1}$$

$$\begin{aligned}
\mathcal{N}(B^0 \rightarrow K^{*0}\pi^0(\rightarrow e^+e^-\gamma)) = {} & \mathcal{N}(B^0 \rightarrow K^{*0}J/\psi(\rightarrow e^+e^-)) \\
& \cdot \frac{\epsilon_{B^0\rightarrow K^{*0}\pi^0(\rightarrow e^+e^-\gamma)}}{\epsilon_{B^0\rightarrow K^{*0}J/\psi(\rightarrow e^+e^-)}} \\
& \cdot \frac{\mathcal{B}(B^0 \rightarrow K^{*0}\pi^0(\rightarrow e^+e^-\gamma))}{\mathcal{B}(B^0 \rightarrow K^{*0}J/\psi(\rightarrow e^+e^-))}
\end{aligned}$$

$$\mathcal{N}(B^0 \to K^{*0}\eta(\to \gamma\gamma)) = \mathcal{N}(B^0 \to K^{*0}\gamma) \cdot \frac{\epsilon_{B^0\to K^{*0}\eta(\to\gamma\gamma)}}{\epsilon_{B^0\to K^{*0}\gamma}} \cdot \frac{\mathcal{B}(B^0 \to K^{*0}\eta(\to \gamma\gamma))}{\mathcal{B}(B^0 \to K^{*0}\gamma)}$$

$$\mathcal{N}(B^0 \to K^{*0}\pi^0(\to \gamma\gamma)) = \mathcal{N}(B^0 \to K^{*0}\gamma) \cdot \frac{\epsilon_{B^0\to K^{*0}\pi^0(\to\gamma\gamma)}}{\epsilon_{B^0\to K^{*0}\gamma}} \cdot \frac{\mathcal{B}(B^0 \to K^{*0}\pi^0(\to \gamma\gamma))}{\mathcal{B}(B^0 \to K^{*0}\gamma)} \tag{9.2}$$

where the branching fraction used are summarized in table 9.1.

	Branching fraction from PDG [5]
$\mathcal{B}(B^0 \to K^{*0}\eta)$	$(1.59\pm0.10)\cdot10^{-5}$
$\mathcal{B}(\eta \to e^+e^-\gamma)$	$(6.9\pm0.4)\cdot10^{-3}$
$\mathcal{B}(B^0 \to K^{*0}\pi^0)$	$(3.3\pm0.6)\cdot10^{-6}$
$\mathcal{B}(\pi^0 \to e^+e^-\gamma)$	$(1.174\pm0.035)\cdot10^{-2}$
$\mathcal{B}(B^0 \to K^{*0}J/\psi)$	$(1.27\pm0.05)\cdot10^{-3}$
$\mathcal{B}(J/\psi \to e^+e^-)$	$(5.971\pm0.032)\cdot10^{-2}$
$\mathcal{B}(B^0 \to K^{*0}\gamma)$	$(4.18\pm0.25)\cdot10^{-5}$

TABLE 9.1: Branching fractions used in the background constraints calculations

Simultaneously to the very low and gamma region fit with electron final states, also the $K^{*0}J/\psi$ mode is fitted in order to constraint the mass shape parameters of very low q^2 and provide yields used to constraint the expected backgrounds in very low and gamma q^2. This simultaneous fit is performed for each run period and trigger category independently.

The results combining all run periods and triggers are presented here for the very low (figure 9.1) and gamma (figure 9.2) q^2 bins. The results for the individual run periods and trigger categories can be found in appendix B together with the fits for the J/ψ mode. The yields of the signal components are presented in table 9.2 and the contributions of the different backgrounds are displayed in table 9.3.

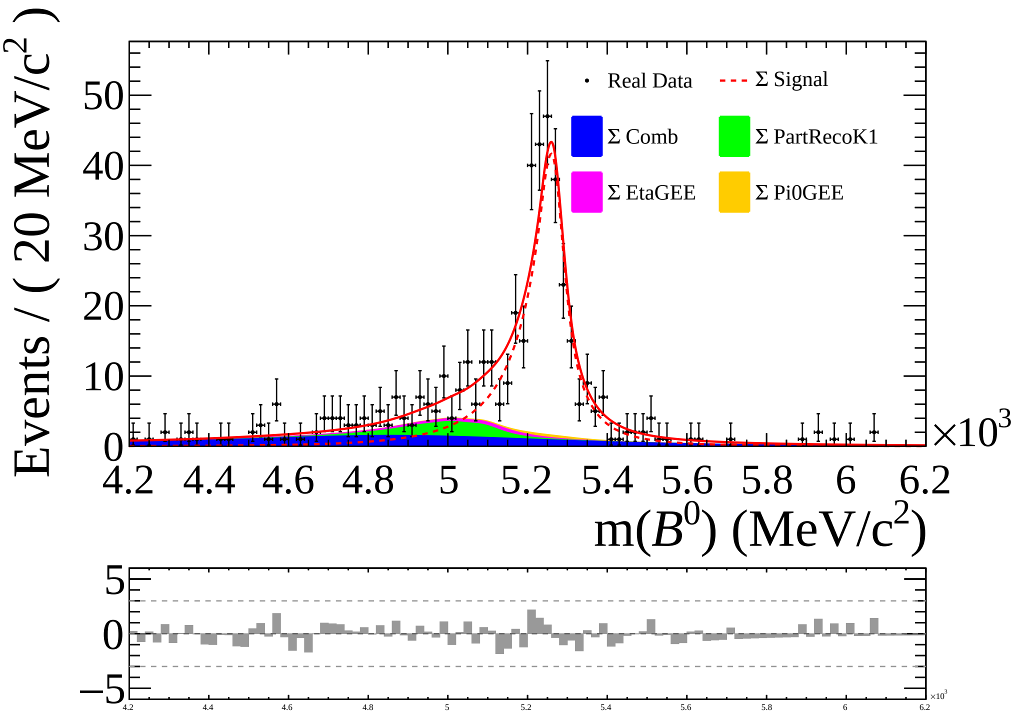

FIGURE 9.1: Total data fit of $B^0 \to K^{*0}e^+e^-$ candidates in the very low q^2 for all run periods and trigger categories merged

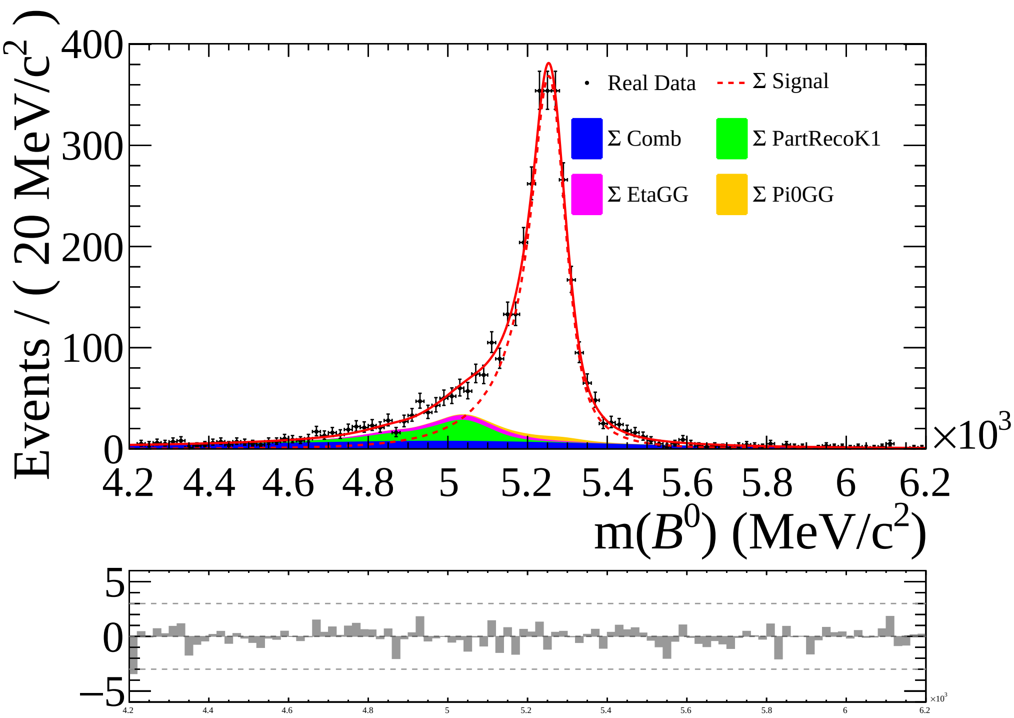

FIGURE 9.2: Total data fit of $B^0 \to K^{*0}\gamma(\to e^+e^-)$ candidates in the gamma q^2 for all run periods and trigger categories merged

Sample	Signal yield, very low q^2	Signal yield, gamma q^2
R1 - L0I	34±7	404±25
R1 - L0L	35±6	459±19
R2p1 - L0I	45±8	392±28
R2p1 - L0L	50±7	376±23
R2p2 - L0I	75±10	751±35
R2p2 - L0L	86±10	664±31

TABLE 9.2: Signal yields for each run period and trigger category in the total data mass fit

Sample	$f_{B^0 \to K^{*0}\eta}$	$f_{B^0 \to K^{*0}\pi^0}$	$f_{PartReco}$	$\mathcal{N}_{Comb}$
R1 - L0I, vlow	$(6.0\pm0.9)\cdot10^{-5}$	$(2.8\pm0.7)\cdot10^{-5}$	$(0.8\pm0.4)\cdot10^{-1}$	5±5
R1 - L0L, vlow	$(2.7\pm0.5)\cdot10^{-5}$	$(1.3\pm0.4)\cdot10^{-5}$	$1.5\pm0.5)\cdot10^{-1}$	0±1
R2p1 - L0I, vlow	$(7.3\pm0.8)\cdot10^{-5}$	$(3.5\pm0.8)\cdot10^{-5}$	$(0.8\pm0.5)\cdot10^{-1}$	21±7
R2p1 - L0L, vlow	$(3.1\pm0.4)\cdot10^{-5}$	$(1.3\pm0.3)\cdot10^{-5}$	$(0.6\pm0.4)\cdot10^{-1}$	3±2
R2p2 - L0I, vlow	$(6.7\pm0.8)\cdot10^{-5}$	$(3.2\pm0.7)\cdot10^{-5}$	$(1.3\pm0.4)\cdot10^{-1}$	41±10
R2p2 - L0L, vlow	$(3.2\pm0.4)\cdot10^{-5}$	$(1.1\pm0.3)\cdot10^{-5}$	$(0.8\pm0.3)\cdot10^{-1}$	16±6
R1 - L0I, gamma	$(3.0\pm0.9)\cdot10^{-2}$	$(1.5\pm0.1)\cdot10^{-2}$	$(0.8\pm0.4)\cdot10^{-1}$	57±17
R1 - L0L, gamma	$(2.8\pm1.4)\cdot10^{-2}$	$(1.5\pm0.1)\cdot10^{-2}$	$(1.5\pm0.5)\cdot10^{-1}$	24±11
R2p1 - L0I, gamma	$(4.9\pm129)\cdot10^{-2}$	$(2.6\pm0.1)\cdot10^{-2}$	$(0.8\pm0.5)\cdot10^{-1}$	96±21
R2p1 - L0L, gamma	$(1.9\pm0.8)\cdot10^{-2}$	$(1.0\pm0.1)\cdot10^{-2}$	$(0.6\pm0.4)\cdot10^{-1}$	19±12
R2p2 - L0I, gamma	$(4.9\pm1.2)\cdot10^{-2}$	$(2.6\pm0.1)\cdot10^{-2}$	$(1.3\pm0.4)\cdot10^{-1}$	188±25
R2p2 - L0L, gamma	$(1.9\pm0.8)\cdot10^{-2}$	$(1.0\pm0.1)\cdot10^{-2}$	$(0.8\pm0.3)\cdot10^{-1}$	83±17

TABLE 9.3: Contributions of the different backgrounds in the total data mass fit for each run period and trigger category. The fractions f_{bkg} are expressed as fractions of signal; $\mathcal{N}_{Comb}$ is the number of combinatorial events

9.2 Total angular modelling

For the total angular modelling, the shapes are fixed to the ones determined independently for each component, and for each run period and trigger category, the yields of the different components are fixed to the ones measured with the mass fits.

The resulting plots are shown on figures 9.3 and 9.4 respectively for the very low and the gamma q^2 bins. The final total shapes match well the data, indicating that the results found in the mass fit are trustworthy and that the components used are well describing the data. The plots for each run period and trigger separately are shown in appendix C.

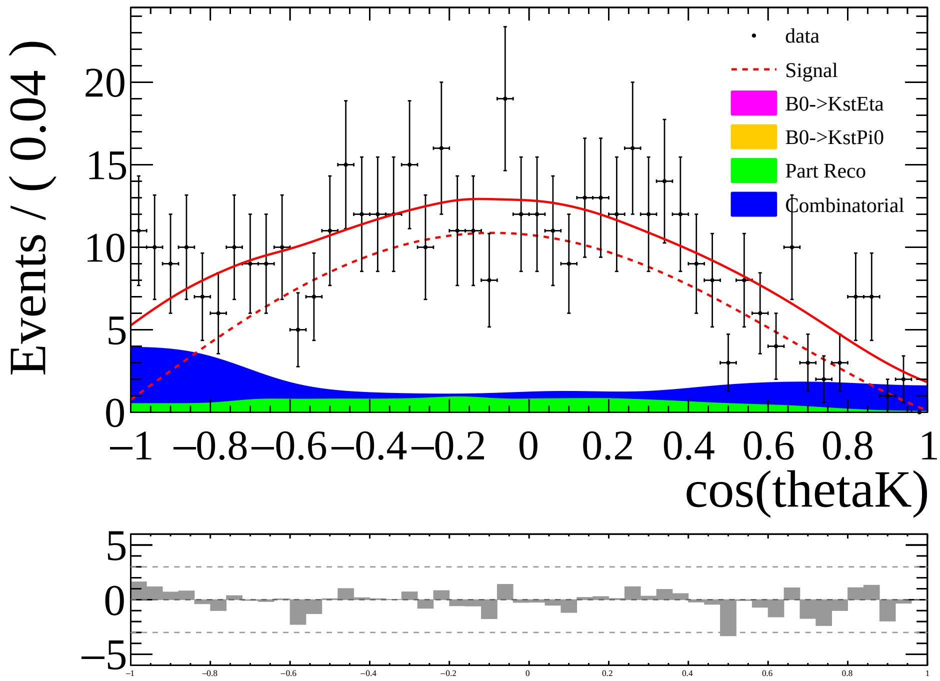

FIGURE 9.3: Total data model of $B^0 \to K^{*0}e^+e^-$ candidates in the very low q^2 for all run periods and trigger categories merged

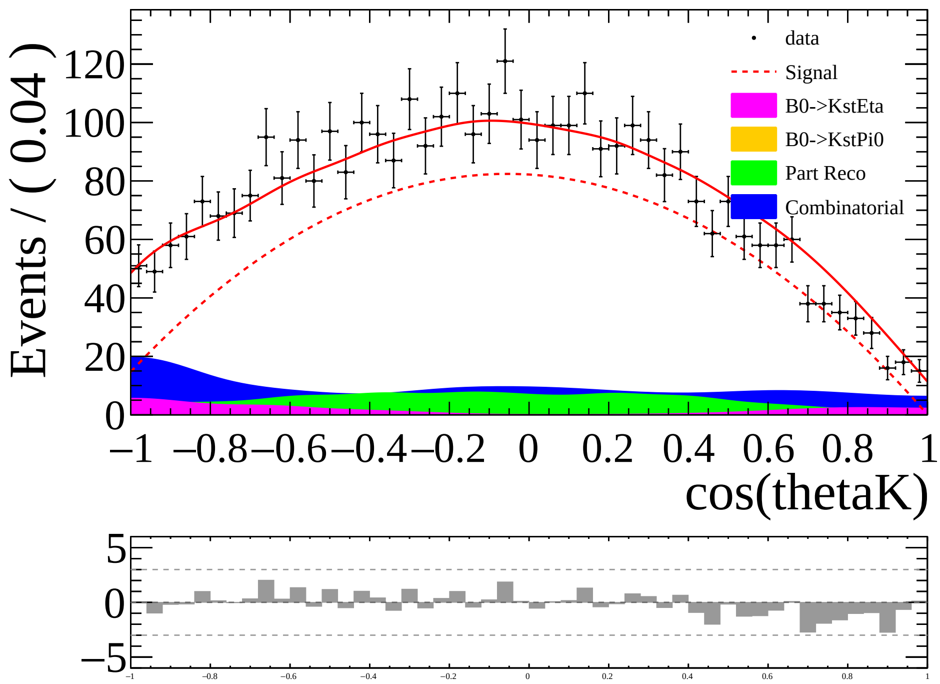

FIGURE 9.4: Total data model of $B^0 \to K^{*0}\gamma(\to e^+e^-)$ candidates in the gamma q^2 for all run periods and trigger categories merged

9.3 Cross-check of efficiency corrections

A way to verify that the efficiency corrections strategy applied is valid is to take advantage of the high statistics obtained in γ and very low q^2 to measure the variation of yields and efficiency under different selections. In this thesis the PID selection and the multivariate classifier requirement is varied and the variation of yields and efficiencies are compared. The results of such comparison are used as an indicator of the goodness of the correction to simulation and efficiency estimation procedure.

Therefore, the fits to the invariant mass of the B candidates are also performed applying a tighter PID cut than the nominal one, as specified in table 9.4. The check is also performed removing from the selection the PRMVA cut, responsible for the reduction of the partially reconstructed background in the nominal selection scenario. This case is labelled with "noPRMVA" in the following. The mass fits for the tight and noPRMVA setups are shown in appendix B.

	Nominal	Tight
electron PID cut	`Min(E1_ProbNNe,E2_ProbNNe) > 0.2 && Min(E1_PIDe, E2_PIDe) > 2`	`Min(E1_ProbNNe,E2_ProbNNe) > 0.4 && Min(E1_PIDe, E2_PIDe) > 3`

TABLE 9.4: PID cut setups for the study of the yields and efficiency variations

The resulting yields and efficiency are presented in table 9.5 for the fits with the PRMVA applied, and in table 9.6 for the fits without the PRMVA cut.

Category	$\mathcal{N}$(nominal)	$\mathcal{N}$(tight)	$\frac{\mathcal{N}_{tight}}{\mathcal{N}_{nominal}}$	$\frac{\epsilon_{tight}}{\epsilon_{nominal}}$
R1 - L0I, gamma	404±25	391±25	$96.6^{+1.0}_{-0.8}$ %	$97.2^{+0.5}_{-0.4}$ %
R1 - L0L, gamma	259±19	244±19	$94.2^{+1.6}_{-1.3}$ %	$97.6^{+1.1}_{-1.0}$ %
R2p1 - L0I, gamma	392±28	314±27	$80.2^{+2.1}_{-1.9}$ %	$85.0^{+1.7}_{-1.3}$ %
R2p1 - L0L, gamma	376±23	323±21	$86.0^{+1.9}_{-1.7}$ %	$83.7^{+1.8}_{-1.4}$ %
R2p2 - L0I, gamma	751±35	612±31	$81.5^{+1.5}_{-1.4}$ %	$82.8^{+1.3}_{-1.0}$ %
R2p2 - L0L, gamma	664±31	538±27	$81.1^{+1.6}_{-1.5}$ %	$82.6^{+1.8}_{-1.4}$ %
R1 - L0I, vlow	34±7	30±6	$88.2^{+6.6}_{-4.4}$ %	$93.6^{+0.6}_{-0.4}$ %
R1 - L0L, vlow	35±6	29±5	$84.8^{+7.0}_{-5.1}$ %	$95.4^{+0.5}_{-0.4}$ %
R2p1 - L0I, vlow	45±8	43±8	$96.0^{+4.0}_{-2.1}$ %	$87.8^{+0.6}_{-0.6}$ %
R2p1 - L0L, vlow	50±7	44±7	$87.9^{+5.3}_{-3.9}$ %	$87.2^{+0.6}_{-0.6}$ %
R2p2 - L0I, vlow	75±10	64±9	$85.5^{+4.5}_{-3.6}$ %	$86.8^{+0.5}_{-0.5}$ %
R2p2 - L0L, vlow	86±10	71±9	$82.1^{+4.5}_{-3.7}$ %	$85.7^{+0.6}_{-0.5}$ %

TABLE 9.5: Yields and efficiency variations under PID cut

Category	$\mathcal{N}$(nominal)	$\mathcal{N}$(tight)	$\frac{\mathcal{N}_{tight}}{\mathcal{N}_{nominal}}$	$\frac{\epsilon_{tight}}{\epsilon_{nominal}}$
R1 - L0I, gamma	445±29	430±27	$96.6^{+1.0}_{-0.8}$ %	$97.1^{+0.4}_{-0.4}$ %
R1 - L0L, gamma	298±21	282±20	$94.4^{+1.5}_{-1.2}$ %	$97.9^{+1.0}_{-1.0}$ %
R2p1 - L0I, gamma	449±31	363±27	$80.8^{+1.9}_{-1.8}$ %	$85.0^{+1.5}_{-1.3}$ %
R2p1 - L0L, gamma	433±26	361±22	$83.4^{+1.9}_{-1.7}$ %	$83.3^{+1.5}_{-1.6}$ %
R2p2 - L0I, gamma	830±40	677±33	$81.2^{+1.4}_{-1.3}$ %	$82.7^{+1.1}_{-1.0}$ %
R2p2 - L0L, gamma	736±33	594±29	$80.8^{+1.5}_{-1.4}$ %	$82.4^{+1.6}_{-1.4}$ %
R1 - L0I, vlow	33±7	35±6	$105.5^{+2.7}_{-5.1}$ %	$93.5^{+0.5}_{-0.4}$ %
R1 - L0L, vlow	36±6	31±5	$85.5^{+6.7}_{-4.9}$ %	$95.2^{+0.5}_{-0.5}$ %
R2p1 - L0I, vlow	50±9	48±8	$95.5^{+3.9}_{-2.1}$ %	$87.7^{+0.6}_{-0.5}$ %
R2p1 - L0L, vlow	54±7	46±7	$85.2^{+5.4}_{-4.2}$ %	$87.0^{+0.6}_{-0.6}$ %
R2p2 - L0I, vlow	80±11	69±10	$86.1^{+4.3}_{-3.4}$ %	$86.7^{+0.5}_{-0.5}$ %
R2p2 - L0L, vlow	93±11	79±10	$84.5^{+4.1}_{-3.4}$ %	$85.8^{+0.6}_{-0.5}$ %

TABLE 9.6: Yields and efficiency variations under PID cut for the no-PRMVA samples

For both with and without PRMVA cases, the yields and efficiency variations are compatible regarding the errors. This relative verification is thus a good indication that the corrections to simulation applied here are controlled in the very low and gamma q^2 regions.

9.4 Measurement of $\mathcal{B}(B^0 \to K^{*0}e^+e^-)$ in very low q^2 and comparison to theory

Using the measured yields and the estimated efficiencies in the very low q^2 and in the J/ψ mode, one can measure the branching fraction of the $B^0 \to K^{*0}e^+e^-$ decay in the very low q^2 bin according to expression (1.2). The branching fractions are firstly computed for each year and trigger independently and are presented in table 9.7. The single category result is then combined using the `blue-combine` package in order to account for the correlation or not of the different uncertainties. For example, the external measurement value of $\mathcal{B}(B^0 \to K^{*0}J/\psi)$ is taken fully correlated among the various categories for the final averaging, while simulated events statistic uncertainties affecting the efficiency evaluation are taken fully uncorrelated.

Considering the theoretical side, the `Flavio` prediction for the ratio $\frac{\mathcal{B}(B^0\to K^{*0}e^+e^-,vl)}{\mathcal{B}(B^0\to K^{*0}\gamma)}$ considering the effective q^2 range determined in 1.6 is found to be (3.778±0.025)$\cdot 10^{-3}$. To perform this measurement, the $d\mathcal{B}/dq^2(B^0 \to K^{*0}e^+e^-)$ prediction from `Flavio` which can be seen on figure 9.5 is integrated over the effective q^2 range [0.00098, 0.10160] GeV^4/c^2. By measuring directly the ratio $\mathcal{B}(B^0 \to K^{*0}e^+e^-, vl)/\mathcal{B}(B^0 \to$

$K^{*0}\gamma$), one can benefit from the fully correlated aspect of the branching fractions and the cancellation of uncertainties in the ratio.

$\mathcal{B}(B^0 \to K^{*0}e^+e^-, vl)$	R1	R2p1	R2p2
L0I	(1.45±0.30)·10^{-7}	(1.56±0.29)·10^{-7}	(1.31±0.19)·10^{-7}
L0L	(1.85±0.31)·10^{-7}	(1.87±0.28)·10^{-7}	(1.70±0.21)·10^{-7}
All runs and triggers		(1.57±0.12)·10^{-7}	

TABLE 9.7: Measured value of the $\mathcal{B}(B^0 \to K^{*0}e^+e^-, vl)$

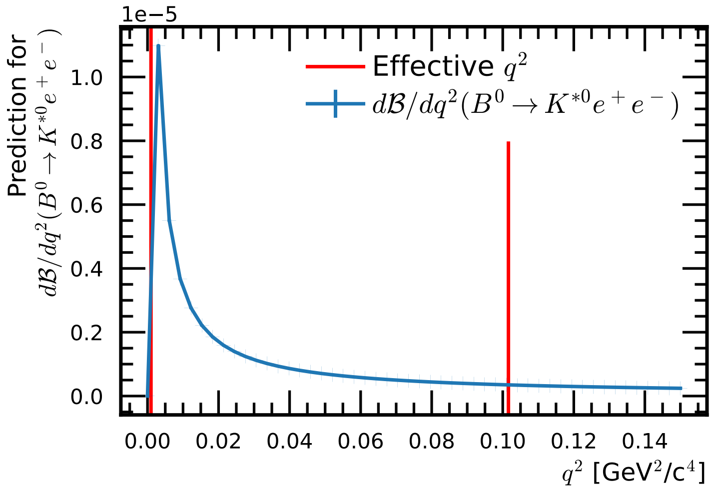

FIGURE 9.5: `Flavio` prediction for $d\mathcal{B}/dq^2(B^0 \to K^{*0}e^+e^-)$

By multiplying this ratio value by the world average value from PDG $\mathcal{B}(B^0 \to K^{*0}\gamma) = (4.18 \pm 0.25) \cdot 10^{-5}$, one can get the expected $\mathcal{B}(B^0 \to K^{*0}e^+e^-, vl)$, which is equal to (1.58±0.10)·10^{-7}. If one uses the slightly more precise value from Belle $\mathcal{B}(B^0 \to K^{*0}\gamma) = (3.96 \pm 0.07 \pm 0.14) \cdot 10^{-5}$ [10], the expected $\mathcal{B}(B^0 \to K^{*0}e^+e^-, vl)$ is (1.50±0.08)·10^{-7}. The measured and the expected values are thus totally compatible regarding the uncertainties, which means that the efficiency correction method is valid in the very low q^2. Using the other setups where the PRMVA cut is removed and/or with the tight PID cut from table 9.4, one finds branching fractions which are also totally compatible with the theory expectation. The experimental results for the different setups compared to the predicted value of the branching fraction are summarised in table 9.8 and figure 9.6.

	$\mathcal{B}(B^0 \to K^{*0}e^+e^-, vl)$
Nominal setup	$(1.57 \pm 0.12) \cdot 10^{-7}$
Nominal, noPRMVA setup	$(1.54 \pm 0.12) \cdot 10^{-7}$
Tight setup	$(1.53 \pm 0.12) \cdot 10^{-7}$
Tight, noPRMVA setup	$(1.54 \pm 0.12) \cdot 10^{-7}$
Predicted value (PDG)	$(1.58 \pm 0.10) \cdot 10^{-7}$
Predicted value (Belle)	$(1.50 \pm 0.08) \cdot 10^{-7}$

TABLE 9.8: Measured and predicted values for $\mathcal{B}(B^0 \to K^{*0}e^+e^-, vl)$. The label "PDG/Belle" denotes which value of $\mathcal{B}(B^0 \to K^{*0}\gamma)$ is used for the prediction.

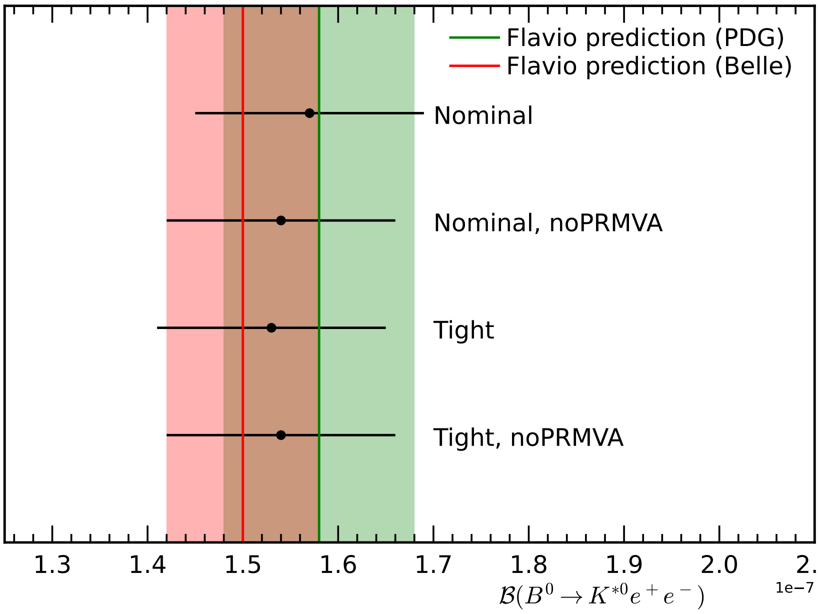

FIGURE 9.6: Measured and predicted values for $\mathcal{B}(B^0 \to K^{*0}e^+e^-, vl)$. The label "PDG/Belle" denotes which value of $\mathcal{B}(B^0 \to K^{*0}\gamma)$ is used for the prediction.

9.5 Prospects

The precision of this result and the procedure of validating efficiencies corrections in electron samples at very low q^2 will be significantly improved by amelioration in both the statistical yields from LHCb with Run 3 data taking and the reduction of the errors in the $\mathcal{B}(B^0 \to K^{*0}\gamma)$ from Belle II.

Indeed, the LHC Run 3 will provide much more statistics with an expected integrated luminosity of 50 fb^{-1} by the end of Run 3. Moreover, the $B^0 \to K^{*0}\gamma$ branching fraction value measured by the Belle II experiment is currently $\mathcal{B}(B^0 \to K^{*0}[K^+\pi^-]\gamma) = (4.5 \pm 0.3 \pm 0.2) \cdot 10^{-5}$, where the first uncertainty is statistical and the second is systematic [25], and it is expected to significantly improve in precision in the coming years with the ramping up data-taking at Belle II. The work performed in this thesis is expected to be a milestone check to be performed in any future LFU analysis in LHCb validating the efficiency correction and providing a stringent validation of the analysis method in the future.

For such reason, the same approach and strategy can be applied in other decay modes analysed at LHCb, such as $B_s^0 \to \phi e^+e^-$ providing an equally valid cross-check in the $\mathcal{R}_\phi$ measurements and any LFU measurements using B_s^0 hadrons.

In the measurement performed in this study, the systematic uncertainty on efficiency is neglected as the uncertainty is widely dominated by statistical uncertainties. However, with the statistics improvement from LHC Run 3, these systematics will become more important to control and must be included in the measurements. To do so, a first step, which would allow to directly account for the systematics budget and their correlations, is to allow the fitter to directly fit for the branching ratio value, reparameterising the yields as a function of efficiencies and a single branching ratio value. Then the systematics affecting the efficiency estimation as well as the fit systematics and their correlations can be directly embedded in the fitter by applying multi-variate Gaussian constraints on the efficiency ratio factors entering the yields parameterisation. Doing so, the branching ratio parameter of interest will be one of the free parameters in the fitter and the errors arising from the efficiencies and the Gaussian constraints from the systematics will propagate directly on the fitted value and its error determination.

Finally, the fits performed in the gamma q^2 bin can be used to measure the $B^0 \to K^{*0}\gamma$ branching fraction at LHCb. However, no calibration sample exists for now to calibrate photon conversion in LHCb, therefore the result is not expected to be excellent, but it is still found to be not too far from the world average ($(3.61\pm0.17)\cdot10^{-5}$ vs $(4.18\pm0.25)\cdot10^{-5}$ in PDG) without accounting for any dedicated correction in the conversion. It is also important to note that the absolute efficiencies estimation in this bin suffer from different issues such as consistency in simulation versions compared to J/ψ mode as well as lack in statistics and several assumptions of portability of 2016 efficiencies for 2017/2018. To be noted however that for relative efficiency variation, and particularly the PID test, those effects are expected to be irrelevant.

An analysis dedicated to this decay in LHCb using conversion would be a nice follow-up. To perform such analysis (measure the $\mathcal{B}(B^0 \to K^{*0}\gamma$ with converted photons) would require the development of a calibration sample for electrons originating from photon conversions. If this would be feasible in LHCb, the result could become competitive and open up a variety of measurements in LHCb using converted photons which are not possible nowadays, being all affected by the lack of a calibration sample to correct material interaction and conversion in material at LHCb. For this, a sample of ($c\bar{c} \to \chi_{ci} \to J/\psi\ \gamma$), with $ci = c1, c2$, could be used as it is well-defined and provides high statistics. The idea would be to use the mass difference between χ_{ci} and J/ψ to have a sharp and narrow mass peak, where the $J/\psi \to \mu^+\mu^-$ is used. The reconstruction through a $J/\psi \to \mu\mu$ channel in fact, benefits of an excellent mass resolution and very high reconstruction efficiency as well as the possibility to be directly available in the very first stages of the trigger selection chain. This ultimately would motivate the need of developing a dedicated trigger reconstruction/selection of $J/\psi\gamma(\to ee)$ calibration line for converted electron calibration.

10 Conclusion

This master project aimed at validating the analysis methods used to measure the $\mathcal{R}_X$ ratios, which is a measurement performed in LHCb to test the lepton flavour universality in the SM in rare b hadron decays.

This is made by measuring the branching fraction of the $B^0 \to K^{*0}e^+e^-$ decay in the very low q^2 bin. Such validation allows to verify two key ingredients of the $\mathcal{R}_X$ analysis: the corrections to simulation for electrons and the associated efficiency calculation, as well as the validity of the analysis and corrections to simulation across the full q^2 region.

In parallel to the very low q^2, the $B^0 \to K^{*0}\gamma(\to e^+e^-)$ is studied to provide constraints for the very low q^2 mass fit and to perform complementary studies able to validate the selection and the correction to simulation under different final states selection requirements.

After the definition of a cut-based selection, for both the $B^0 \to K^{*0}e^+e^-$ and $B^0 \to K^{*0}\gamma(\to e^+e^-)$ decays, the reconstructed B^0 invariant mass is fitted in the very low and gamma q^2 bins. The fits are performed simultaneously in three data taking periods Run 1 (2011-2012), Run 2 part 1 (2015-2016) and Run 2 part 2 (2017-2018), and in each of them in the two trigger categories (L0I and L0L). The fits are performed under different setups to study both the impact of the partially reconstructed MVA (PRMVA) selection and the stability of the ratio of yields and efficiency under different electron PID cut. For each bin, the participating backgrounds are identified and fitted using Monte-Carlo simulation samples. A Monte-Carlo sample of the decay of interest is also fitted as the signal component. Once the shapes are defined, they are implemented in the RX framework in which the total data fits are performed, simultaneously with the normalisation channel $B^0 \to K^{*0}J/\psi(\to e^+e^-)$.

Besides that, angular fits of the θ_K angle are performed for the same signal and backgrounds components in the two bins. For the total data modelling, the yields determined in the mass fits are assigned to the components and it is found that they are compatible with the angular data and that they don't suffer from any large mismodelling.

In order to account for mis-simulated effects, corrections are applied on the efficiencies following the strategy developed in the $\mathcal{R}_X$ analysis. A check on the variation of the efficiencies compared to yield variation is performed using both the very low and the gamma q^2 bins applying different PID selections to the electrons. It is found that the ratio of yield and efficiency is stable, which is a good hint that the correction to simulation method is valid at such low q^2 and that the results are invariant under different PID requirements.

Then, the correction to simulation is applied in order to measure the branching fraction $\mathcal{B}(B^0 \rightarrow K^{*0}e^+e^-)$ in the very low q^2 and comparing it to the predicted value from theory scaled by the externally provided $\mathcal{B}(B^0 \rightarrow K^{*0}\gamma)$. In fact, using the ratio of the branching fraction in the very low q^2 to the $\mathcal{B}(B^0 \rightarrow K^{*0}\gamma)$ allows to cancel a large part of the theoretical uncertainties. Therefore, an expectation from theory for $\mathcal{B}_{pred}(B^0 \rightarrow K^{*0}e^+e^-, vl)$ can be computed and is found to be $(1.58 \pm 0.10) \cdot 10^{-7}$ when using the world average value of $\mathcal{B}(B^0 \rightarrow K^{*0}\gamma)$ from PDG, and $(1.50 \pm 0.08) \cdot 10^{-7}$ when using the Belle measurement of $\mathcal{B}(B^0 \rightarrow K^{*0}\gamma)$.

With the nominal selection setup (PRMVA applied, loose PID cut), the measured $\mathcal{B}_{meas}(B^0 \rightarrow K^{*0}e^+e^-, vl)$ is found to be $(1.57 \pm 0.12) \cdot 10^{-7}$, while for the setup where the PRMVA is not applied and/or with a tighter electron PID selection, the measured value $\mathcal{B}_{meas}(B^0 \rightarrow K^{*0}e^+e^-, vl)$ is found to be between $(1.53 \pm 0.12) \cdot 10^{-7}$ and$(1.54 \pm 0.12) \cdot 10^{-7}$ depending on the case.

In all cases, the measured and predicted values are totally compatible, indicating that the analysis method and in particular the efficiency corrections are valid in the very low q^2. One can thus assume its validity over the whole q^2 range up to the $J/\psi\ (1S)$ and $\psi\ (2S)$ resonant modes.

A Full selection

The full selection applied to data is presented in tables A.1, A.2 and A.3. For the PID cut, the one presented here is the nominal one, the tighter cut studied is specified in section 9. For the MVA cut, this is the most restrictive cut studied. For the case without constraint on the partially reconstructed MVA the part `cat_wMVA_PR_lowcen > 0.50` is simply removed.

For the MC samples, an additional selection with truthmatching is applied. It consists in requiring the events to be in certain background categories defines as follows:

- `BKGCAT == 0` : signal
- `BKGCAT == 10` : signal but with all intermediate states not fully reconstructed
- `BKGCAT == 20` : fully reconstructed physics background
- `BKGCAT == 30` : misidentifications
- `BKGCAT == 40` : partially reconstructed physics background
- `BKGCAT == 50` : signal with radiative losses
- `BKGCAT == 60` : ghosts

The cuts applied for signal and background MC samples for all run periods are thus:

- Signal : `((((B0_BKGCAT == 0 || B0_BKGCAT == 10)||(B0_BKGCAT == 50))|| (B0_BKGCAT == 60))&& ((((E1_TRUEID==0) + (E2_TRUEID==0) + (K_TRUEID==0) + (Pi_TRUEID==0) <=1 ))))&& (SignalLikeness>=3)`
- Backgrounds : `((((((B0_BKGCAT == 20)|| (B0_BKGCAT == 30))|| (B0_BKGCAT == 40))|| (B0_BKGCAT == 50))|| (B0_BKGCAT == 60))|| (B0_BKGCAT == 0 || B0_BKGCAT == 10))&& ((((E1_TRUEID==0) + (E2_TRUEID==0) + (K_TRUEID==0) + (Pi_TRUEID==0) <=1 )))`

<table>
<tr><th>Category</th><th>Run period</th><th>Cut</th></tr>
<tr><td>BKG</td><td>All*</td><td><code>(((((TMath::Max(B0_M012,B0_M013_Subst3_pi2K)
< 5100)&& (!(B0_M23_Subst3_pi2K < 1040 &&
Pi_MC15TuneV1_ProbNNpi < 0.8)))&&
(!((TMath::Abs(B0_TRACK_M_Subst_Kl2lK_DTF_JPs
- 5279.580000) < 60 &&
E1_MC15TuneV1_ProbNNe < 0.8) ||
(TMath::Abs(B0_TRACK_M_Subst_lpi2pil_DTF_JPs
- 5279.580000) < 60 &&
E2_MC15TuneV1_ProbNNe < 0.8))))&&
(!((TMath::Abs(B0_TRACK_M_Subst_Kl2lK_DTF_Psi
- 5279.580000) < 60 &&
E1_MC15TuneV1_ProbNNe < 0.8) ||
(TMath::Abs(B0_TRACK_M_Subst_lpi2pil_DTF_Psi
- 5279.580000) < 60 &&
E2_MC15TuneV1_ProbNNe < 0.8))))&&
((!(TMath::Abs(TMath::Sqrt(TMath::Sq(K_PE+Pi_PE+
TMath::Sqrt(TMath::Sq(139.570180)+
TMath::Sq(E2_TRACK_PX)+ TMath::Sq(E2_TRACK_PY)+
TMath::Sq(E2_TRACK_PZ))) -
TMath::Sq(K_PX+Pi_PX+E2_TRACK_PX) -
TMath::Sq(K_PY+Pi_PY+E2_TRACK_PY) -
TMath::Sq(K_PZ+Pi_PZ+E2_TRACK_PZ)) - 1869.650000)
< 30 && E2_MC15TuneV1_ProbNNe < 0.8))&&
(!(TMath::Abs(B0_TRACK_M12_Subst1_e2pi - 1864.830000)
< 30 && E2_MC15TuneV1_ProbNNe < 0.8))))&&
(JPs_VMI_D > 0.3)</code>**</td></tr>
<tr><td>HOP</td><td>All</td><td><code>B0_HOP_M > 4800</code></td></tr>
<tr><td>MVA</td><td>All</td><td><code>cat_wMVA_lowcen > 0.50 && cat_wMVA_PR_lowcen > 0.50</code></td></tr>
</table>

TABLE A.1: Selection cuts for rejection of background ; * for Run 1, V15TuneV1 is replaced by V12TuneV3 ; ** only in the very low q^2 bin

<table>
<tr><th>Category</th><th>Run period</th><th>Cut</th></tr>
<tr><td>L0</td><td>All</td><td>B0_L0MuonDecision_TIS || B0_L0HadronDecision_TIS || B0_L0ElectronDecision_TIS</td></tr>
<tr><td rowspan="3">LPET</td><td>Run1</td><td>((Year == 11)&& ((E1_L0ElectronDecision_TOS && E1_L0Calo_ECAL_realET > 2500) || (E2_L0ElectronDecision_TOS && E2_L0Calo_ECAL_realET > 2500)))|| ((Year == 12)&& ((E1_L0ElectronDecision_TOS && E1_L0Calo_ECAL_realET > 3000) || (E2_L0ElectronDecision_TOS && E2_L0Calo_ECAL_realET > 3000)))</td></tr>
<tr><td>Run2p1</td><td>((Year == 15)&&((E1_L0ElectronDecision_TOS && E1_L0Calo_ECAL_realET > 3000) || (E2_L0ElectronDecision_TOS && E2_L0Calo_ECAL_realET > 3000)))||((Year == 16)&& ((E1_L0ElectronDecision_TOS && E1_L0Calo_ECAL_realET > 2700) || (E2_L0ElectronDecision_TOS && E2_L0Calo_ECAL_realET > 2700)))</td></tr>
<tr><td>Run2p2</td><td>((Year == 17)&& ((E1_L0ElectronDecision_TOS && E1_L0Calo_ECAL_realET > 2700) || (E2_L0ElectronDecision_TOS && E2_L0Calo_ECAL_realET > 2700)))|| ((Year == 18)&& ((E1_L0ElectronDecision_TOS && E1_L0Calo_ECAL_realET > 2400) || (E2_L0ElectronDecision_TOS && E2_L0Calo_ECAL_realET > 2400)))</td></tr>
<tr><td>HLT1</td><td>All</td><td>B0_Hlt1TrackMVADecision_TOS</td></tr>
<tr><td>HLT2</td><td>Run1 and Run2p2</td><td>(B0_Hlt2Topo2BodyDecision_TOS || B0_Hlt2Topo3BodyDecision_TOS)|| (B0_Hlt2TopoE2BodyDecision_TOS || B0_Hlt2TopoE3BodyDecision_TOS || B0_Hlt2TopoEE2BodyDecision_TOS || B0_Hlt2TopoEE3BodyDecision_TOS)</td></tr>
<tr><td>TRG</td><td>All</td><td>((B0_L0MuonDecision_TIS || B0_L0HadronDecision_TIS || B0_L0ElectronDecision_TIS))&& (B0_Hlt1TrackMVADecision_TOS)</td></tr>
</table>

TABLE A.2: Selection cuts for trigger requirements

<table>
<tr><th>Category</th><th>Run period</th><th>Cut</th></tr>
<tr><td>PS</td><td>All</td><td>((((((((((E1_InAccEcal==1 && E2_InAccEcal==1)&&
(TMath::Min(E1_L0Calo_ECAL_region,
E2_L0Calo_ECAL_region) >= 0))&&
(!((TMath::Abs(E1_L0Calo_ECAL_xProjection) < 363.6 &&
TMath::Abs(E1_L0Calo_ECAL_yProjection) < 282.6)||
(TMath::Abs(E2_L0Calo_ECAL_xProjection) < 363. &&
TMath::Abs(E2_L0Calo_ECAL_yProjection) < 282.6))))&&
(K_hasRich==1 && Pi_hasRich==1 &&
K_InAccMuon==1 && Pi_InAccMuon==1))&&
(E1_hasRich==1 && E2_hasRich==1 &&
E1_hasCalo==1 && E2_hasCalo==1))&&
(K_PT > 250 && Pi_PT > 250 && Pi_P > 2000 &&
K_P > 2000))&& (TMath::Min(E1_PT,E2_PT) > 500 &&
TMath::Min(E1_P,E2_P) > 3000))&& (Kst_PT > 500
&& TMath::Min(K_IPCHI2_OWNPV,Pi_IPCHI2_OWNPV) > 9))&&
(TMath::Min(E1_PT,E2_PT) > 300 &&
TMath::Min(E1_IPCHI2_OWNPV,E2_IPCHI2_OWNPV) > 9 &&
TMath::Min(TMath::Sqrt(TMath::Sq(E1_TRACK_PX)+
TMath::Sq(E1_TRACK_PY)),
TMath::Sqrt(TMath::Sq(E2_TRACK_PX)+
TMath::Sq(E2_TRACK_PY))) > 200 && JPs_PT > 500))&&
(TMath::Max(K_TRACK_CHI2NDOF,Pi_TRACK_CHI2NDOF) < 3 &&
TMath::Max(K_TRACK_GhostProb,Pi_TRACK_GhostProb)
< 0.4))&&
(TMath::Max(E1_TRACK_CHI2NDOF,E2_TRACK_CHI2NDOF) < 3 &&
TMath::Max(E1_TRACK_GhostProb,E2_TRACK_GhostProb)
< 0.4))&& (1 && H1H2_OA > 0.0005 &&
L1H1_OA > 0.0005 && L1H2_OA > 0.0005 &
& L2H1_OA > 0.0005 && L2H2_OA > 0.0005)</td></tr>
<tr><td>PID</td><td>All*</td><td>((((K_PIDK > -5)&&
(K_MC15TuneV1_ProbNNk * (1 - K_MC15TuneV1_ProbNNp)
> 0.05))&& (K_PIDK > 0))&&
(Pi_MC15TuneV1_ProbNNpi * (1 - Pi_MC15TuneV1_ProbNNk)
* (1 - Pi_MC15TuneV1_ProbNNp) > 0.1))&&
(((TMath::Min(E1_PIDe,E2_PIDe) > 0)&&
(TMath::Min(E1_MC15TuneV1_ProbNNe,E2_MC15TuneV1_ProbNNe)
> 0.2))&& (TMath::Min(E1_PIDe, E2_PIDe) > 2))</td></tr>
<tr><td>KSTMASS</td><td>All</td><td>TMath::Abs(Kst_M - 895.810000) < 100</td></tr>
<tr><td rowspan="2">SPD</td><td>Run1</td><td>nSPDHits < 600</td></tr>
<tr><td>Run2</td><td>nSPDHits < 450</td></tr>
</table>

TABLE A.3: Selection cuts for preselection and particle identification; * for Run 1, V15TuneV1 is replaced by V12TuneV3

B Mass fits

B.1 MC signal fits

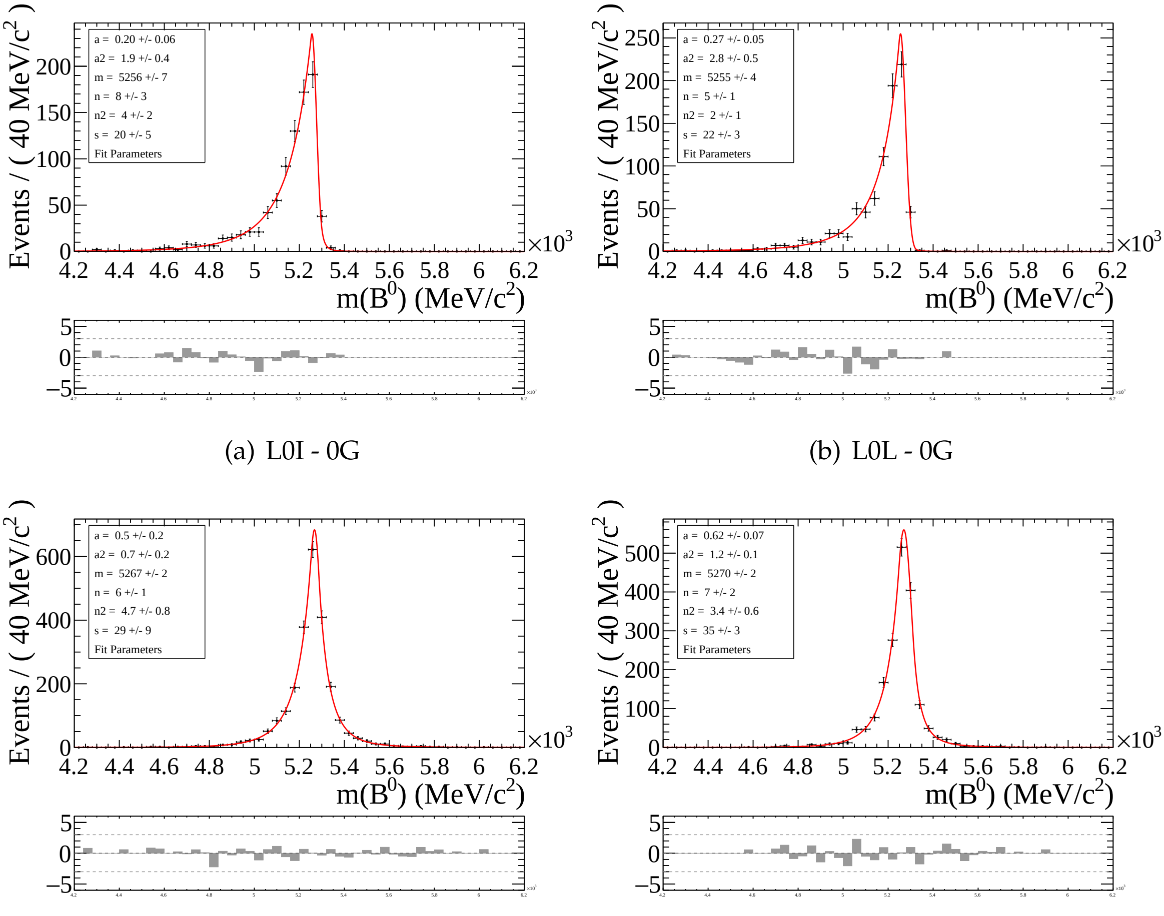

(a) L0I - 0G (b) L0L - 0G

(c) L0I - 1G (d) L0L - 1G

FIGURE B.1: Signal MC fit of $B^0 \to K^{*0}e^+e^-$ candidates in the very low q^2 for R1

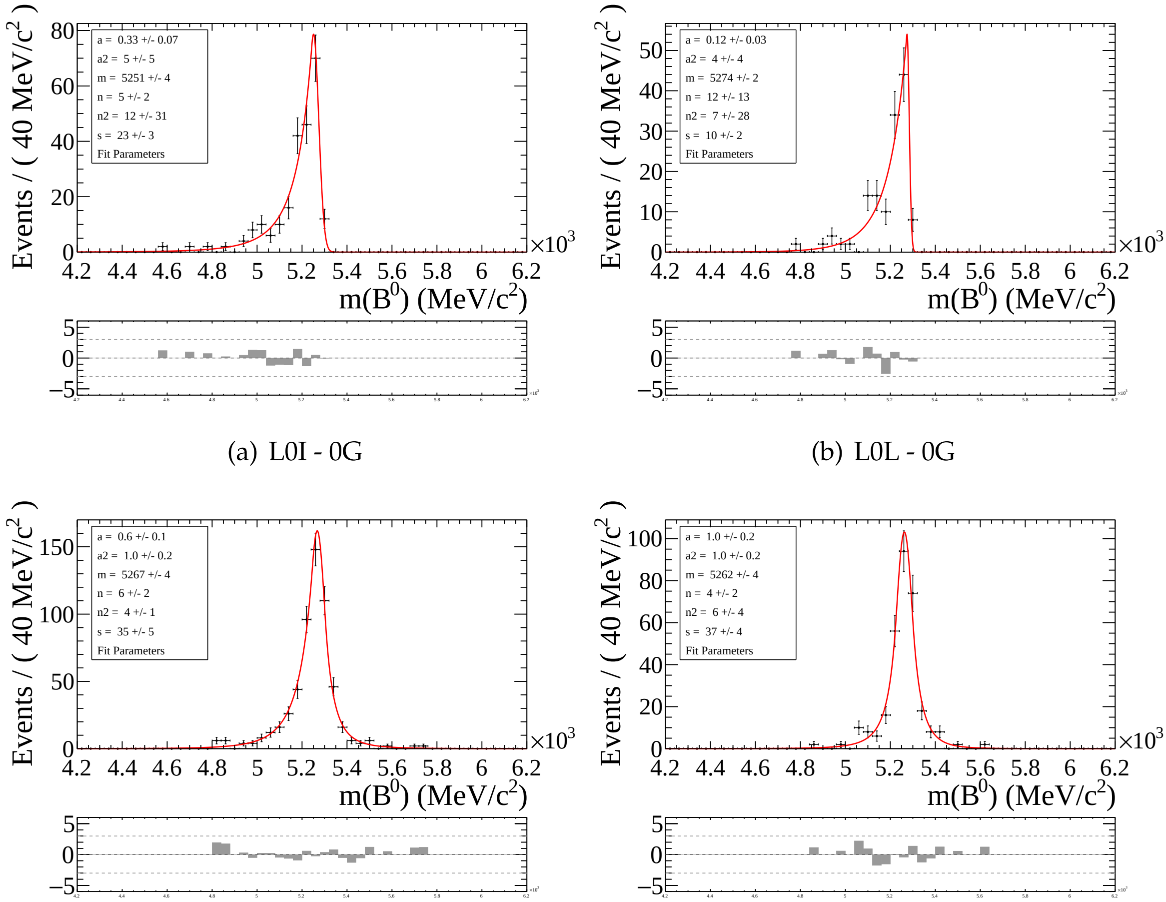

(a) L0I - 0G

(b) L0L - 0G

(c) L0I - 1G

(d) L0L - 1G

FIGURE B.2: Signal MC fit of $B^0 \to K^{*0}\gamma(\to e^+e^-)$ candidates in the gamma q^2 for R1

	0G	1G
Run1 - L0I, very low	0.271	0.729
Run1 - L0L, very low	0.330	0.670
Run2p1 - L0I, very low	0.267	0.733
Run2p1 - L0L, very low	0.337	0.663
Run1 - L0I, gamma	0.283	0.717
Run1 - L0L, gamma	0.327	0.673
Run2p1 - L0I, gamma	0.298	0.702
Run2p1 - L0L, gamma	0.369	0.631

TABLE B.1: MC fraction of events with 0 bremsstrahlung photon emitted (0G) and 1 or more bremsstrahlung photon emitted (1G) for R1 and R2p1

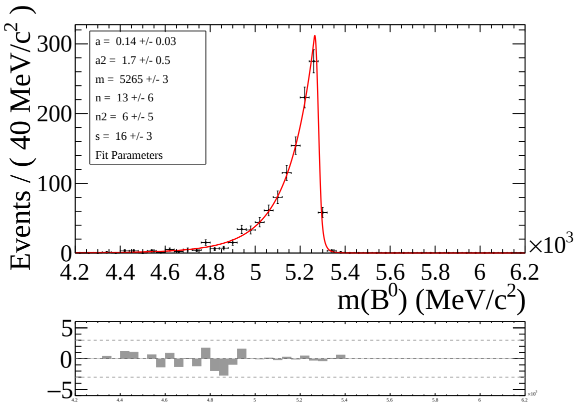

(a) L0I - 0G

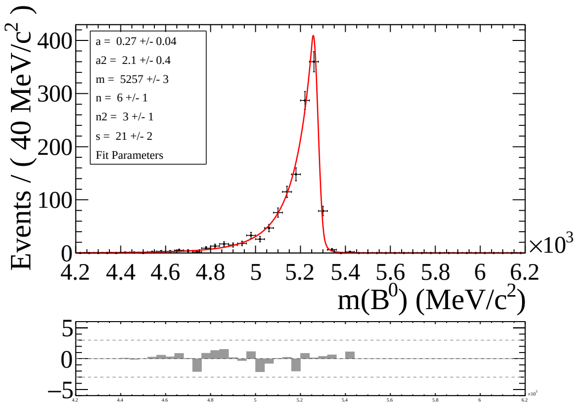

(b) L0L - 0G

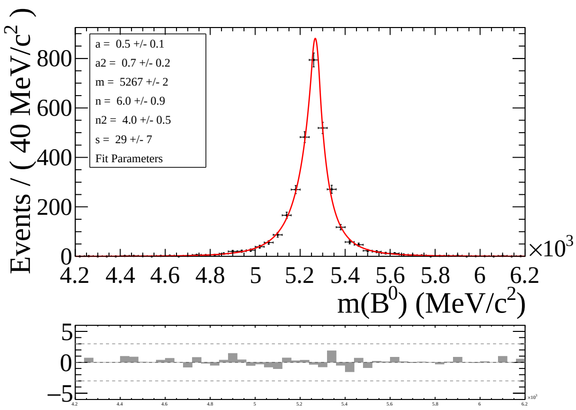

(c) L0I - 1G

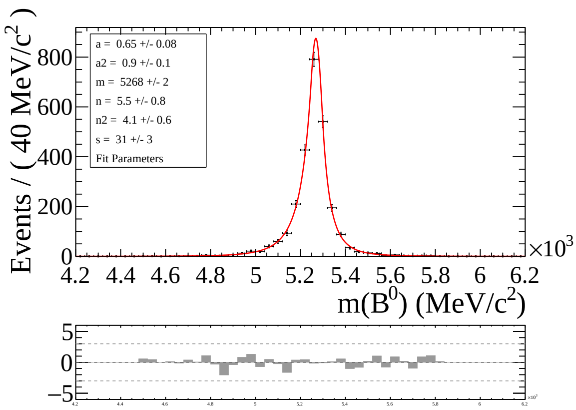

(d) L0L - 1G

FIGURE B.3: Signal MC fit of $B^0 \to K^{*0}e^+e^-$ candidates in the very low q^2 for R2p1

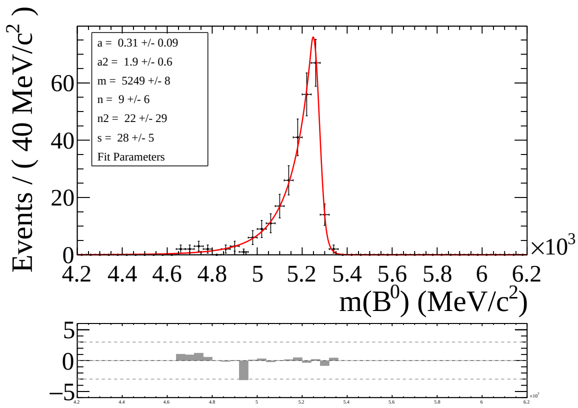

(a) L0I - 0G

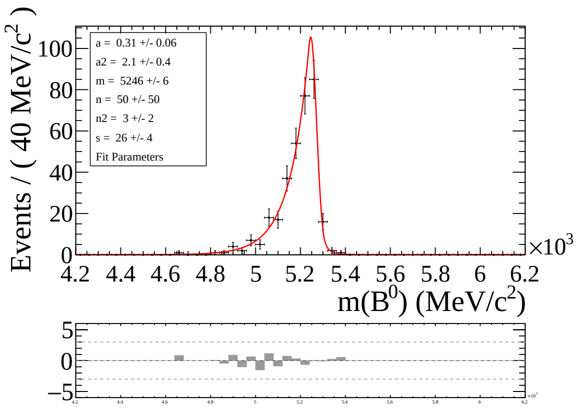

(b) L0L - 0G

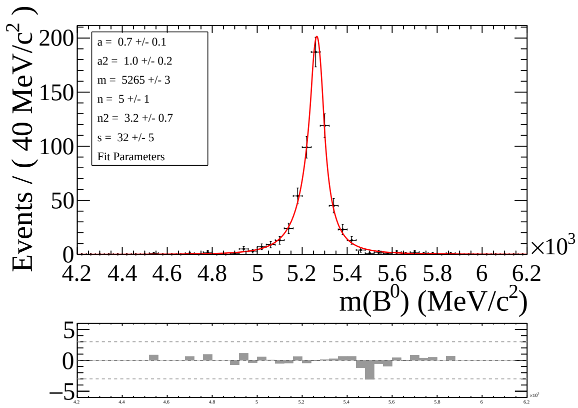

(c) L0I - 1G

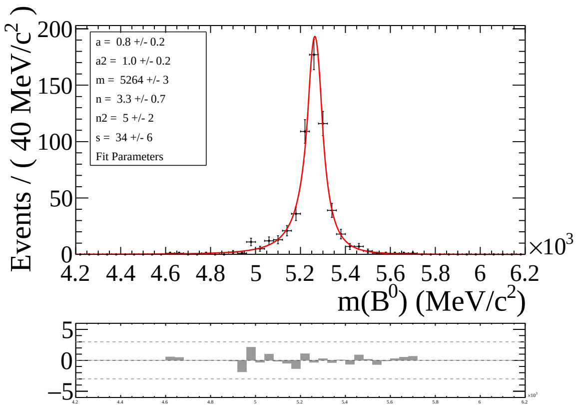

(d) L0L - 1G

FIGURE B.4: Signal MC fit of $B^0 \rightarrow K^{*0}\gamma(\rightarrow e^+e^-)$ candidates in the gamma q^2 for R2p1

B.2 Total data fits

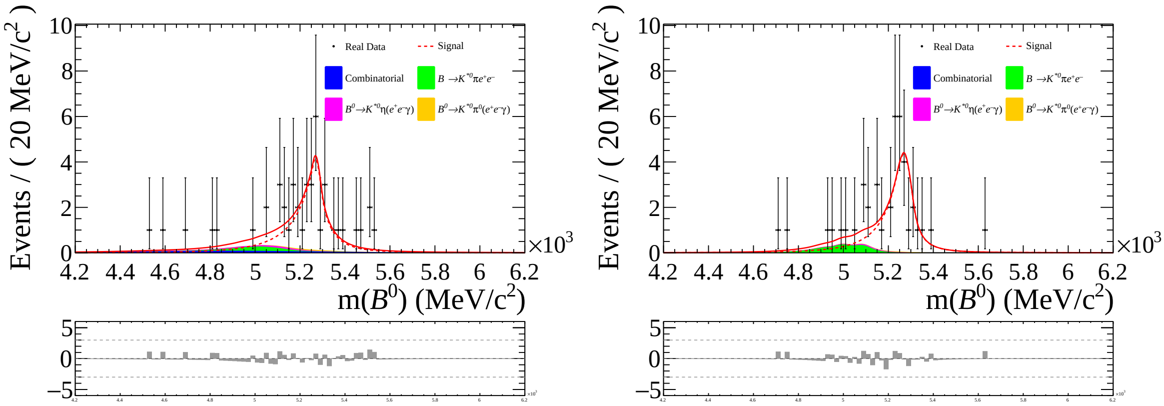

(a) L0I (b) L0L

FIGURE B.5: Total data fit of $B^0 \to K^{*0}e^+e^-$ candidates in the very low q^2 for R1

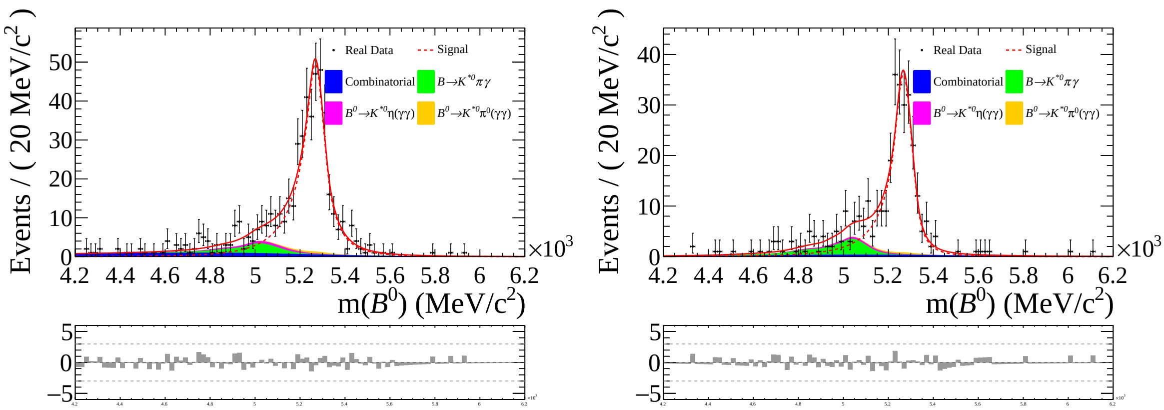

(a) L0I (b) L0L

FIGURE B.6: Total data fit of $B^0 \to K^{*0}\gamma(\to e^+e^-)$ candidates in the gamma q^2 for R1

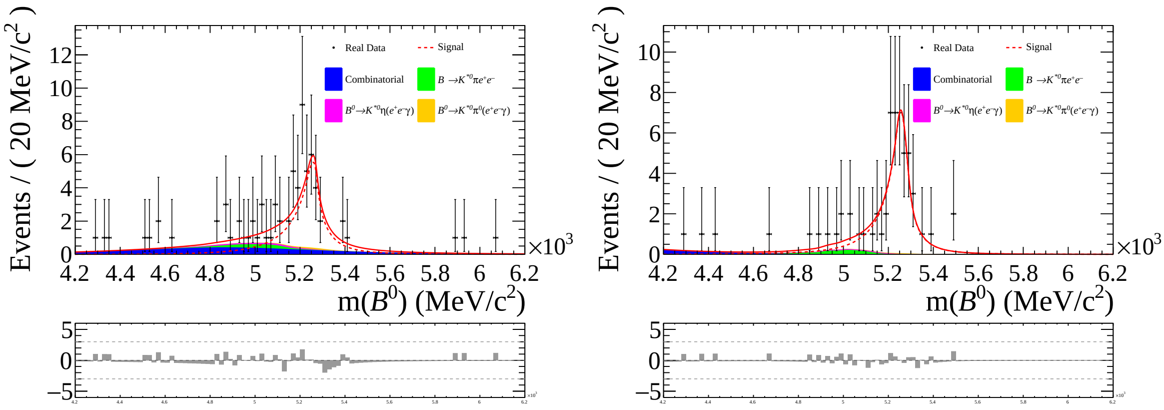

(a) L0I (b) L0L

FIGURE B.7: Total data fit of $B^0 \to K^{*0}e^+e^-$ candidates in the very low q^2 for R2p1

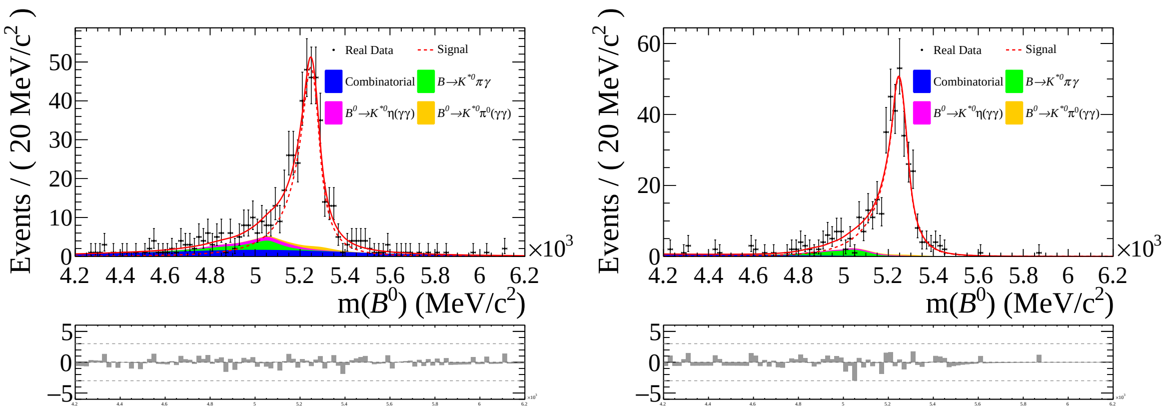

(a) L0I (b) L0L

FIGURE B.8: Total data fit of $B^0 \to K^{*0}\gamma(\to e^+e^-)$ candidates in the gamma q^2 for R2p1

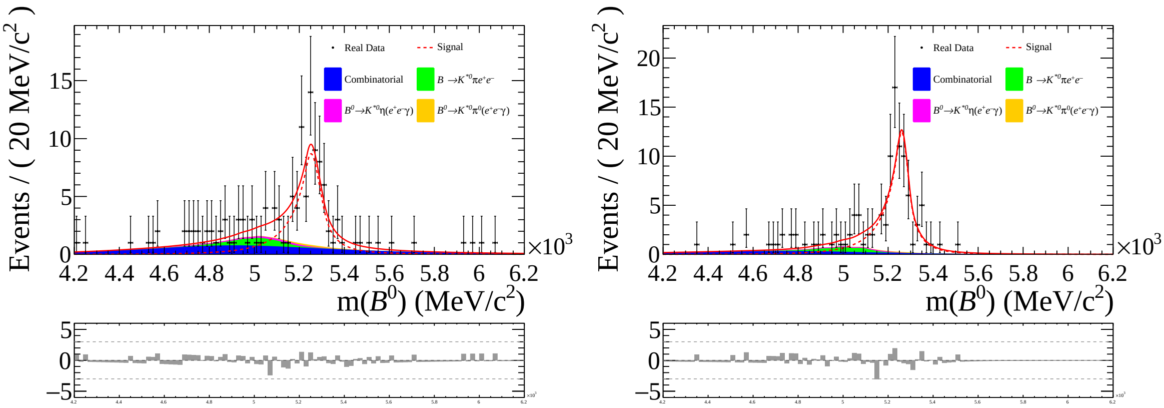

(a) L0I

(b) L0L

FIGURE B.9: Total data fit of $B^0 \to K^{*0}e^+e^-$ candidates in the very low q^2 for R2p2

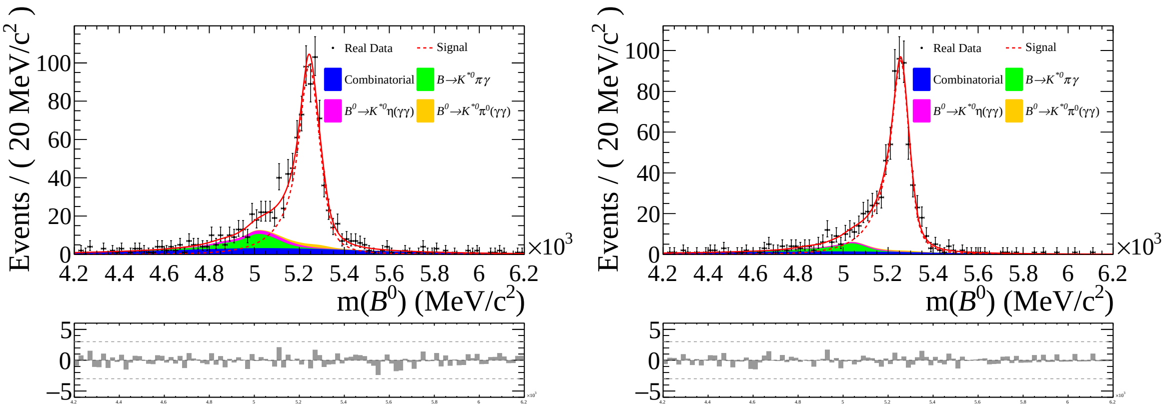

(a) L0I

(b) L0L

FIGURE B.10: Total data fit of $B^0 \to K^{*0}\gamma(\to e^+e^-)$ candidates in the gamma q^2 for R2p2

B.3 J/ψ mode data fits

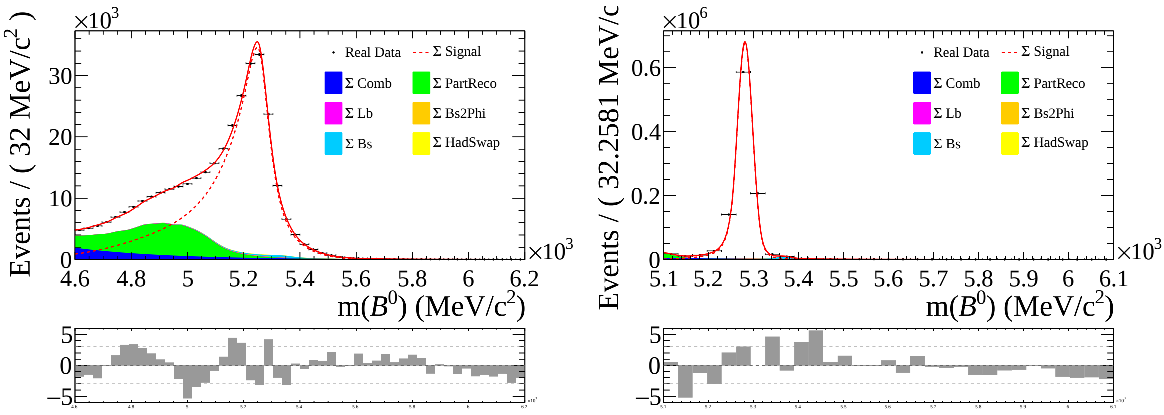

(a) e^+e^- mode (b) $\mu^+\mu^-$ mode

FIGURE B.11: Total data fit of $B^0 \to K^{*0}J/\psi(\to \ell^+\ell^-)$ candidates for all run periods and triggers

Sample	Signal yield, e^+e^- mode	Signal yield, $\mu^+\mu^-$ mode
Run1 - L0I	$(2.503\pm0.013)\cdot10^4$	66224 ± 258
Run1 - L0L	$(2.747\pm0.012)\cdot10^4$	17368 ± 429
Run2p1 - L0I	$(3.145\pm0.016)\cdot10^4$	72952 ± 265
Run2p1 - L0L	$(3.743\pm0.016)\cdot10^4$	16973 ± 414
Run2p2 - L0I	$(6.050\pm0.027)\cdot10^4$	13932 ± 369
Run2p2 - L0L	$(6.993\pm0.028)\cdot10^4$	35137 ± 601

TABLE B.2: Signal yields for each run period and trigger category in the total J/ψ mass fit

B.4 Other setups data fits

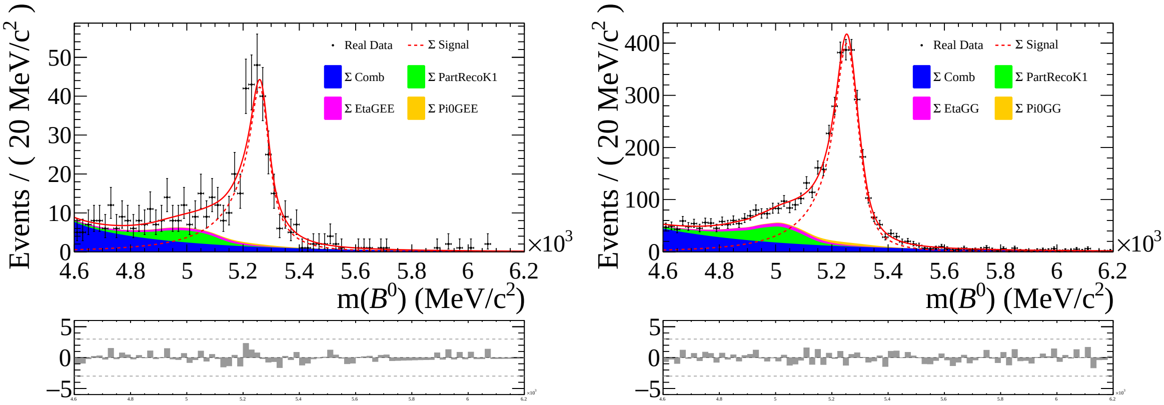

(a) Very Low q^2 : $B^0 \to K^{*0}e^+e^-$ (b) Gamma q^2 : $B^0 \to K^{*0}\gamma(\to e^+e^-)$

FIGURE B.12: Total data fit for all run periods and triggers, noPRMVA setup

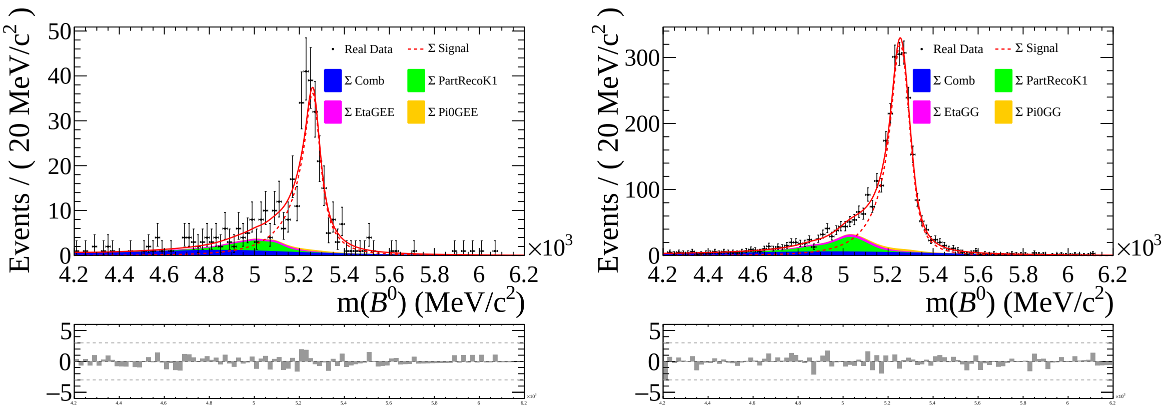

(a) Very Low q^2 : $B^0 \to K^{*0}e^+e^-$ (b) Gamma q^2 : $B^0 \to K^{*0}\gamma(\to e^+e^-)$

FIGURE B.13: Total data fit for all run periods and triggers, tight setup

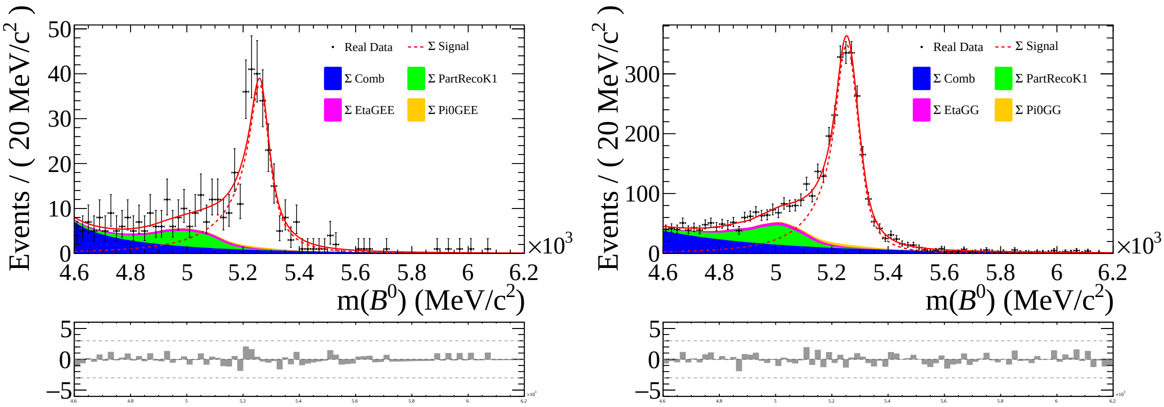

(a) Very Low q^2 : $B^0 \to K^{*0}e^+e^-$

(b) Gamma q^2 : $B^0 \to K^{*0}\gamma(\to e^+e^-)$

FIGURE B.14: Total data fit for all run periods and triggers, tight + no-PRMVA setup

C Angular fits

C.1 MC signal fits

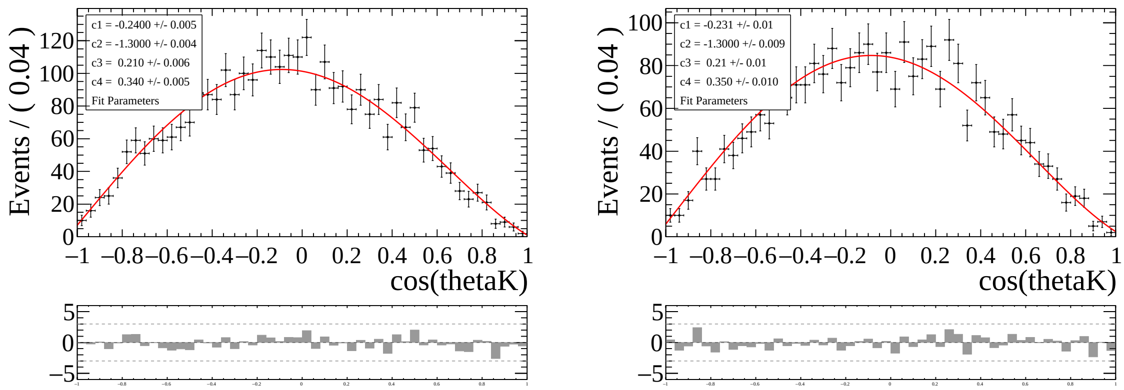

(a) L0I (b) L0L

FIGURE C.1: Signal MC fit of $B^0 \to K^{*0}e^+e^-$ candidates in the very low q^2 for R1

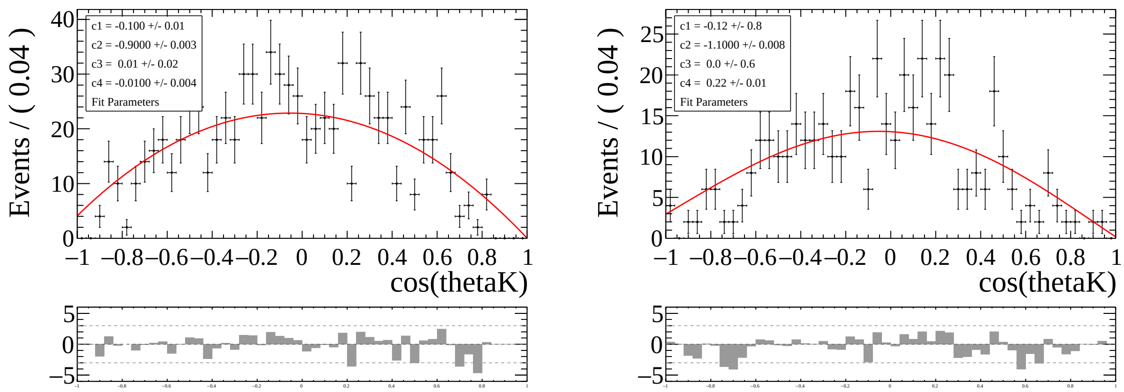

(a) L0I (b) L0L

FIGURE C.2: Signal MC fit of $B^0 \to K^{*0}\gamma(\to e^+e^-)$ candidates in the gamma q^2 for R1

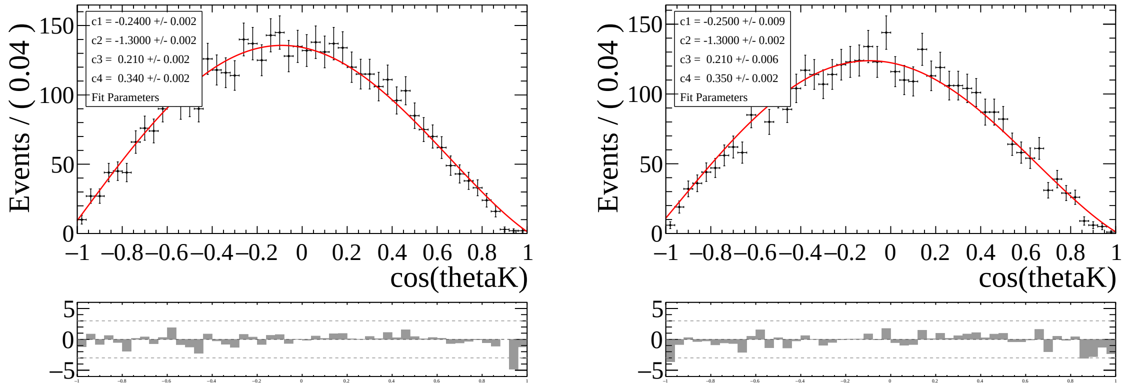

(a) L0I (b) L0L

FIGURE C.3: Signal MC fit of $B^0 \to K^{*0}e^+e^-$ candidates in the very low q^2 for R2p1

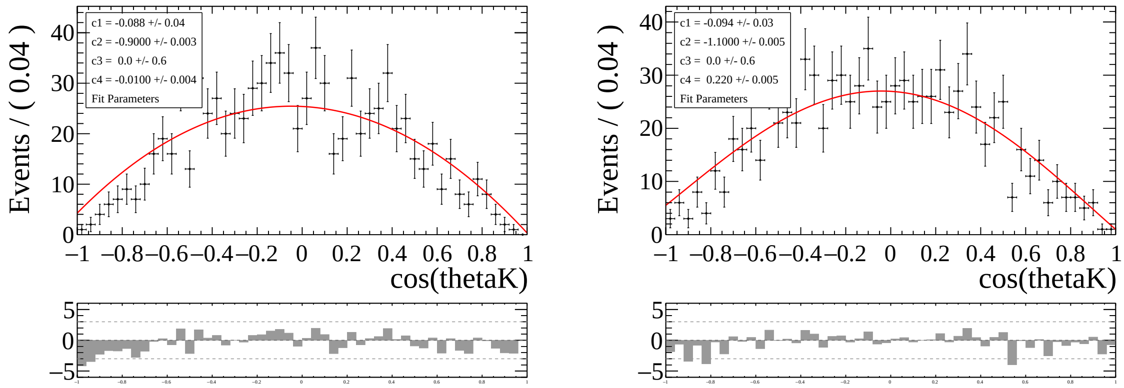

(a) L0I (b) L0L

FIGURE C.4: Signal MC fit of $B^0 \to K^{*0}\gamma(\to e^+e^-)$ candidates in the gamma q^2 for R2p1

C.2 Total data fits

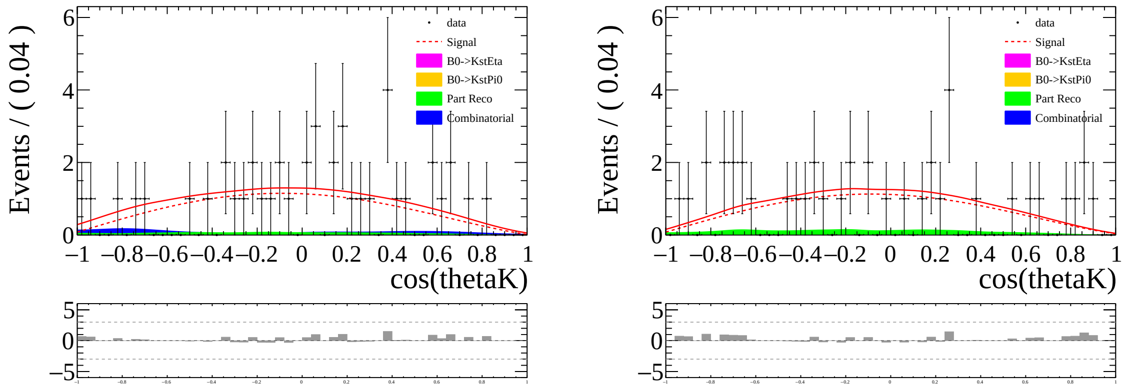

(a) L0I (b) L0L

FIGURE C.5: Total data fit of $B^0 \to K^{*0}e^+e^-$ candidates in the very low q^2 for R1

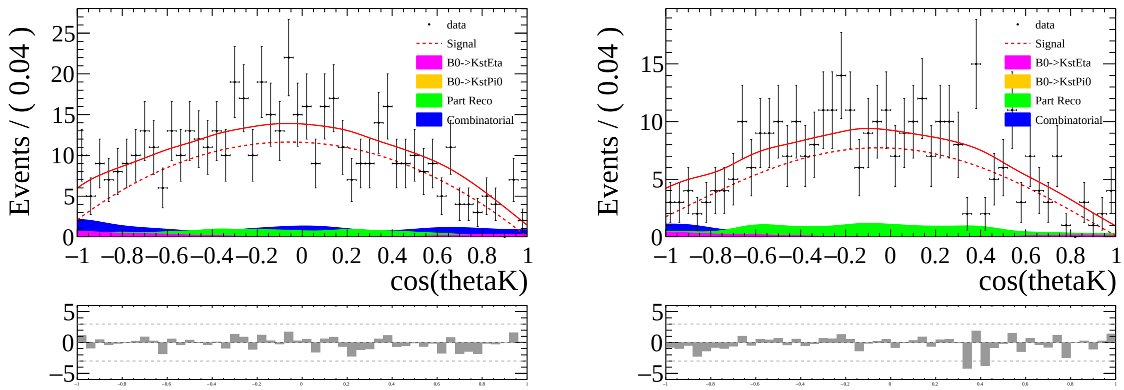

(a) L0I (b) L0L

FIGURE C.6: Total data fit of $B^0 \to K^{*0}\gamma(\to e^+e^-)$ candidates in the gamma q^2 for R1

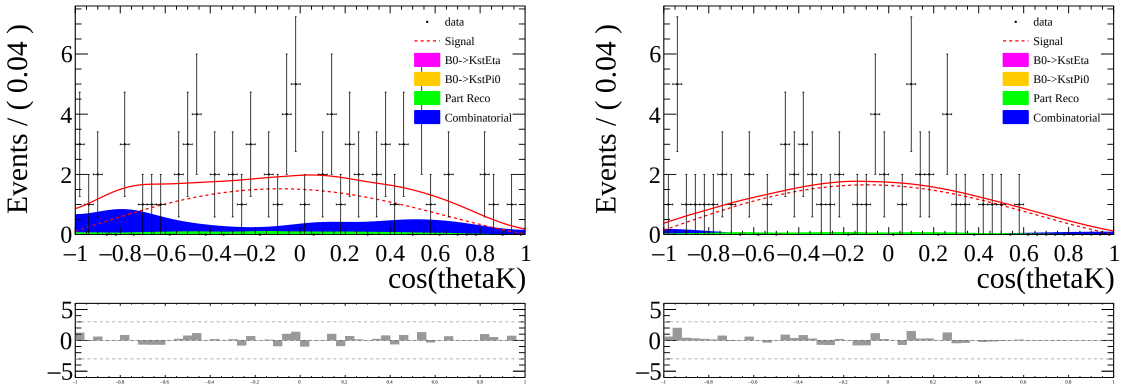

(a) L0I (b) L0L

FIGURE C.7: Total data fit of $B^0 \to K^{*0}e^+e^-$ candidates in the very low q^2 for R2p1

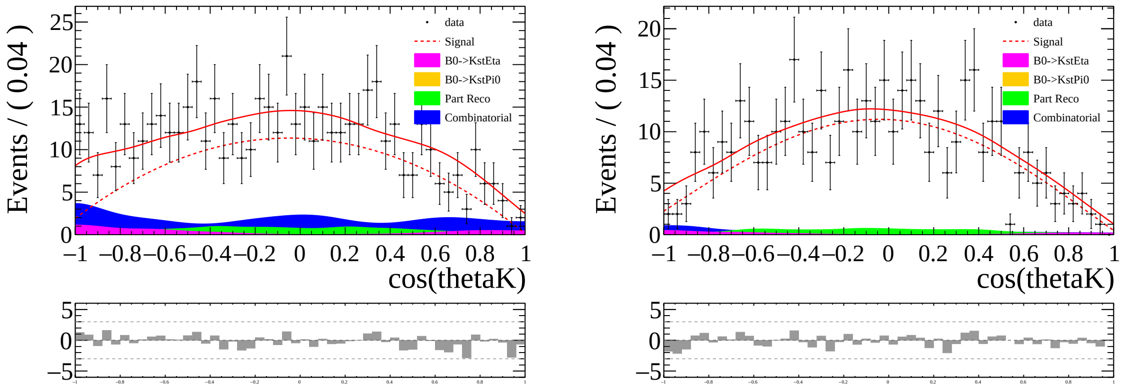

(a) L0I (b) L0L

FIGURE C.8: Total data fit of $B^0 \to K^{*0}\gamma(\to e^+e^-)$ candidates in the gamma q^2 for R2p1

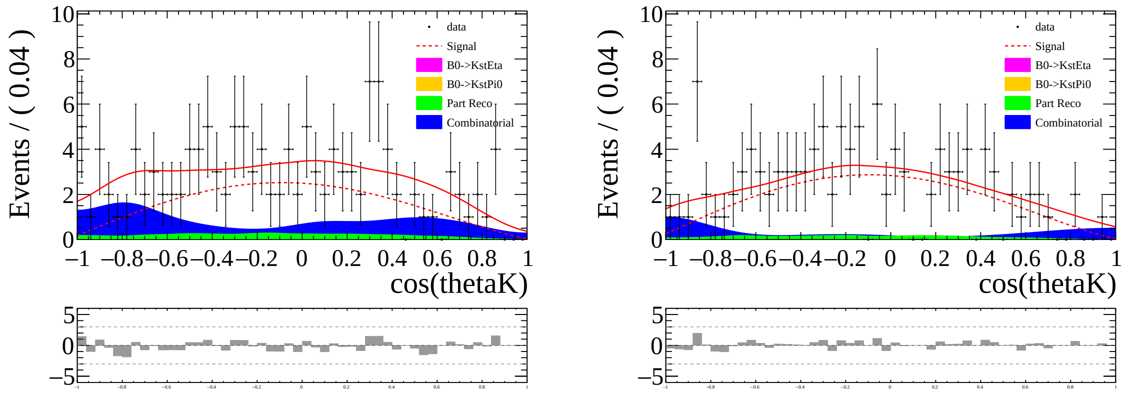

(a) L0I (b) L0L

FIGURE C.9: Total data fit of $B^0 \to K^{*0}e^+e^-$ candidates in the very low q^2 for R2p2

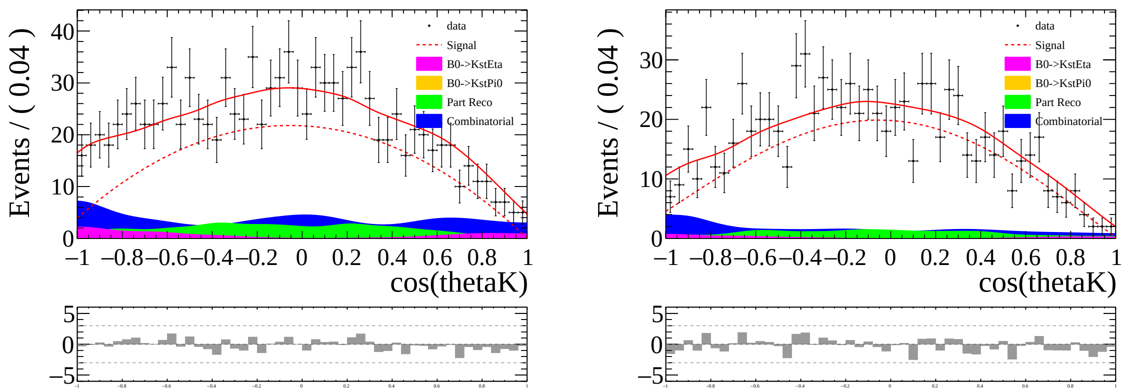

(a) L0I (b) L0L

FIGURE C.10: Total data fit of $B^0 \to K^{*0}\gamma(\to e^+e^-)$ candidates in the gamma q^2 for R2p2

Acknowledgements

First of all, I would like to thank Dr. Renato Quagliani for supervising me during this whole project, answering to my questions, and giving great advices. I would also like to thank Dr. Martino Borsato for the advices and help he provided for this study.
I express my gratitude to Pr. Olivier Schneider and Pr. Lesya Shchutska for giving me the opportunity to do my Master thesis and previous lab projects at the LPHE, and I would like to thank all LPHE members with whom I could work and discuss and from whom I learned a lot.
Finally, I thank my family and friends for supporting and encouraging me during my studies and this Master project.

Bibliography

[1] LHCb Collaboration. "Test of lepton universality in beauty-quark decays". In: *Nature Physics* (2021). DOI: 10.48550/ARXIV.2103.11769.

[2] LHCb Collaboration. "Test of lepton universality with $B^0 \to K^{*0}\ell^+\ell^-$ decays". In: *Journal of High Energy Physics* (2017). DOI: 10.1007/jhep08(2017)055.

[3] LHCb Collaboration. "Test of lepton universality with $\Lambda_b^0 \to pK^+\ell^+\ell^-$ decays". In: *Journal of High Energy Physics* (2020). DOI: 10.1007/jhep05(2020)040.

[4] LHCb Collaboration. "Tests of Lepton Universality Using $B^0 \to K_S^0\ell^+\ell^-$ and $B^+ \to K^{*+}\ell^+\ell^-$ Decays". In: *Physical Review Letters* (2022). DOI: 10.1103/physrevlett.128.191802.

[5] R.L. Workman and others (Particle Data Group). "Review of Particle Physics". In: *Prog. Theor. Exp. Phys.* (to be published (2022)). URL: https://pdg.lbl.gov/.

[6] M. Borsato et al. "Angular analysis of $B^0 \to K^{*0}e^+e^-$ at very low q^2 at LHCb". In: *Internal notes LHCb-ANA-2020-019* (2020).

[7] J. Albrecht et al. "Test of lepton flavour universality with $b \to s\ell^+\ell^-$ decays". In: *Internal notes LHCb-ANA-2020-069, in preparation* (2022).

[8] W. D. Hulsbergen. "Decay chain fitting with a Kalman filter". In: *Nuclear Instruments and Methods in Physics Research Section A: Accelerators, Spectrometers, Detectors and Associated Equipment* (2005). DOI: 10.1016/j.nima.2005.06.078.

[9] LHCb Collaboration. "Strong constraints on the $b \to s\gamma$ photon polarisation from $B^0 \to K^{*0}e^+e^-$ decays". In: *Journal of High Energy Physics* (2020). DOI: 10.1007/jhep12(2020)081.

[10] Belle Collaboration. "Evidence for Isospin Violation and Measurement of CP Asymmetries in $B^0 \to K^*(892)\gamma$". In: *Physical Review Letters* (2017). DOI: 10.1103/physrevlett.119.191802.

[11] S. Cunliffe et al. "Measurement of the differential branching fraction of $B^0 \to K^{*0}(892)\mu^+\mu^-$ and S-wave fraction of $B^0 \to K^+(892)\pi^-\mu^+\mu^-$ decays using 3 fb^{-1} of integrated luminosity". In: *Internal notes LHCb-ANA-2013-096* (2016). URL: https://cds.cern.ch/record/1632245.

[12] M. Thomson. *Modern Particle Physics*. Cambridge University Press, 2013. DOI: 10.1017/CBO9781139525367.

[13] Wikimedia Commons. *Standard Model of Elementary Particles*. URL: https://en.wikipedia.org/wiki/File:Standard_Model_of_Elementary_Particles.svg.

[14] S. Celani. "Lepton Flavour Universality tests and Lepton Flavour Violation searches at LHCb". 2021. DOI: 10.48550/ARXIV.2111.11105.

[15] A. Pich. *Effective Field Theory*. 1998. DOI: 10.48550/ARXIV.HEP-PH/9806303.

[16] D. Bećirević et al. "Future prospects for the determination of the Wilson coefficient $C_7'\gamma$". In: *Journal of High Energy Physics* (2012). DOI: 10.1007/JHEP08(2012)090.

[17] LHCb Collaboration. "The LHCb detector at the LHC". In: *Journal of Instrumentation* (2008). DOI: 10.1088/1748-0221/3/08/s08005.

[18] R. Aaij et al. "Performance of the LHCb Vertex Locator". In: *Journal of Instrumentation* (2014). DOI: 10.1088/1748-0221/9/09/p09007.

[19] LHCb Collaboration. *Letter of Intent for the LHCb Upgrade*. Tech. rep. CERN-LHCC-2011-001, 2011. URL: https://cds.cern.ch/record/1333091.

[20] I. Guz. "The LHCb Calorimeter System: Design, Performance and Upgrade". In: *Talk LHCb-TALK-2017-032*. 2017. URL: https://cds.cern.ch/record/2255089.

[21] R. Quagliani. "Study of double charm B decays with the LHCb experiment at CERN and track reconstruction for the LHCb upgrade". 2017. URL: https://cds.cern.ch/record/2296404.

[22] M.H. Schune, F. Polci, and M. Borsato. *HOP an additional tool for decays involving electrons*. Tech. rep. CERN-LHCb-INT-2015-037, 2015. URL: https://cds.cern.ch/record/2102345.

[23] K. Cranmer. "Kernel estimation in high-energy physics". In: *Computer Physics Communications* (2001). DOI: 10.1016/s0010-4655(00)00243-5.

[24] LHCb Collaboration. "Measurement of the electron reconstruction efficiency at LHCb". In: *JINST* (2019). DOI: 10.1088/1748-0221/14/11/P11023.

[25] Belle II Collaboration. "Measurements of the branching fractions for $B \to K^*$ decays at Belle II". 2021. DOI: 10.48550/ARXIV.2110.08219.